SENSING APPLICATIONS OF GOLD AND SILVER NANOPARTICLES

Chih-Yu Jao

Dissertation submitted to the Faculty of the
Virginia Polytechnic Institute and State University
In partial fulfillment of the requirements for the degree of

Doctor of Philosophy
In
Physics

Hans D. Robinson, Chairman
Giti Khodaparast
Richey M. Davis
James R. Heflin

November 8, 2012
Blacksburg, Virginia

Keywords: dithiocarbamate, localized surface plasmon resonances (LSPRs), fiber optical sensor, polyelectrolyte multilayers (PEMs), two-photon excitation fluorescence (TPEF)

Sensing Applications of Gold and Silver Nanoparticles

Chih-Yu Jao

ABSTRACT

Nanoscale materials have great applications in many areas. One of these applications is for manufacturing ultra-compact and efficient sensors for chemical and biological molecule detection. Noble metals, such as gold (Au) and silver (Ag), because of their distinguished optical property—localized surface plasmon resonances (LSPRs) that exhibit low loss, are ideal materials to fabricate these nanoscale plasmonic particles or structures. This work addresses the synthesis, characterization, and sensing applications of Au and Ag nanoparticles (NPs).

The progress on certain subjects related to our work—NP synthesis, surface functionalization, Au sphere-film structure and two-photon fluorescence—are reviewed in Chapter 1. We also show the calculation results of LSPRs of Au nanosphere suspensions using Mie theory. The measured extinction spectra of Au nanosphere suspensions agree with the calculated results very well.

Chapter 2 is a chapter describing the chemical synthesis of a variety of NPs, such as Ag prisms and cubes, Au spheres, rods, and bipyramids. These experiments involved different synthetic mechanisms and methods which enabled us to prepare NPs with desired shapes and optical properties.

To put these NPs into application, it is desirable and sometimes necessary to functionalize their surfaces. In Chapter 3, we present the functionalization of Ag cubes with poly(allylamine hydrochloride) (PAH) and poly(allylamine hydrochloride)-dithiocarbamate (PAH-DTC), which follows our previous work on Au NPs. The purpose of studying Ag instead of Au is to use the stronger plasmonic enhancement in Ag when applied to two-photon imaging applications. However, we found that PAH-DTC shrank the Ag cubes. We also functionalized the cationic

hexadecyltrimethylammonium bromide (CTAB)-stabilized Au NRs with anionic poly(sodium 4-styrenesulfonate) (PSS). Coated with the strong polyelectrolyte PSS, the NRs become more manageable and can be stable for over six months and are easily immobilized onto positively charged substrate. We put PSS-functionalized Au NPs into use and studied their adsorption process onto PAH-coated optical fiber tapers by monitoring the transmission light through the fiber. When the diameter of the fiber taper gets smaller, stronger coupling occurred between transmitted light inside the taper and the Au NPs on the taper surface (cylinder). This coupling resulted in a loss of the guided light at the plasmon resonance wavelength of the NPs. By monitoring this loss, we can study the adsorption rate of Au NPs onto the fiber.

In Chapter 4, we used Au nanospheres to study the adsorption rate on substrates with different curvatures. We also established a theoretical model to explain this phenomenon for cylindrical surface as well as planar and spherical surfaces. Our results fit well with the theory, which predicts that particle adsorption rates depend strongly on surface geometry, and can exceed the planar surface deposition rate by over two orders of magnitude when the diffusion length of the particle is large compared to the surface curvature.

In Chapter 5, we studied the optical properties of Au nanospheres separated from a thick Au film by a polyelectrolyte multilayer (PEM) film assembled from PAH and PSS under specific pH condition. The PEM film undergoes swelling and shrinking when the environmental pH is changed as a result of charging and discharging of the polyelectrolytes. Therefore, the PEM film provides an efficient means to tune the distance between Au spheres and Au film. The extinction peak blue-shifted as much as 100 nm when the pH of the water changed from pH 10 to pH 3 for 100 nm diameter Au spheres on a PEM film assembled at pH 9.5. Our preliminary estimates that the gap between sphere and surface can be as small as a few nm even though the film itself is tens of nm thick when it is not constrained by Au spheres.

We studied two-photon excitation fluorescence (TPEF) from Ag triangles in Chapter 6. The triangles were fabricated by nanosphere lithography, which used convective self-assembly to make the nanosphere mask. The LSPRs of the nanotriangles were tuned to be in the 800–900 nm range to match with the Ti:Sapphire pulse laser at 880 nm. We found that certain spots on the

fluorescence images gave rise to larger fluorescence intensity than rest of the area. SEM imaging reveals that the unusually bright spots seen on the surface were related to regions where the triangles transformed to spherical particles. The larger intensity is tentatively ascribed to the plasmon resonance of those spherical particles in ~400 nm range.

ACKNOWLEDGEMENT

Thanks to Department of Physics, Virginia Tech for giving the opportunity to study here. During my studies here, I am very grateful to have had interactions with many people and they have positively influenced my research life in Blacksburg. It is impossible to mention everyone individually; and I hope those people who care about me but do not appear in this brief acknowledgement understand my appreciation nonetheless.

First of all, I would like to thank my advisor, Dr. Hans Robinson, who has been giving me opportunities to work on some fascinating research projects. Not only has Dr. Robinson been so kind and patient enough to impart me a lot of expertise in different areas, but also always willing to discuss obstacles and progress in my experiments.

I would like to give thanks to my committee members: Dr. Richey Davis in the Chemical Engineering Department for his many suggestions on organic chemistry and nanoparticle synthesis as well as allowing me to use the instruments in his lab; Dr. Giti Khodaparast for the assistance on con-focal microscope and care; Dr. James Heflin for two very helpful courses—optics and nanotechnology, and generously letting me use the spectrophotometer in his lab.

I have received much advice and help from the faculty members and staff in the department: Dr. Uwe Täuber has given QM courses with overwhelming assignments for two semesters, and powerful suggestions for my research direction; Dr. Marvin Blecher, Dr. Kyungwha Park, Dr. Tetsuro Mizutani, and Dr. Jean Heremans have given me useful course trainings and other conversations related to my study; Dr. Yong Xu in the ECE Department, Dr. Yong-Woo Lee in the Biomedical Sciences Department, and Dr. Webster Santos in the Chemistry Department have also given me suggestions on my research; Graduate program coordinator, Chris Thomas, was a great help from the beginning to the end of my study here. And many other staff facilitated my work from purchase orders to deliveries. Thanks to our you-can-count-on-him computer technician, Travis Heath, for his 5-star service.

There are many people who trained me in areas related to my research: Stephen McCartney, John McIntosh and Dr. Niven Monsegue gave SEM and TEM trainings; Dr. William Miles showed me the very first nanoparticle synthesis, Raquel Mejia showed me the use of Zetasizer, and Sharavanan Balasubramaniam lent me his huge centrifuge. Travis Merritt was very helpful for the imaging spectrometer though I did not have enough time to work much on that. Dr. Brenden Magill continues my project on the fluorescence measurement.

I would like to thank all graduate students who have worked closely with me: Jihaeng Yi, Ishac Kandas and Dr. Chalongrat Daengngam for working interesting projects with me and contributed the results presented here; Dr. Stefan Stoianov and Dr. Kai Chen for being senior members in the lab; Erich See and Kirby Myers Esq. for being the junior members in the lab, and Dr. Jason Ridley for being a visiting member. Dr. Kriton Papavasiliou for the peaceful talks. And other short term lab users and members. Without them, I would not have had an exciting life in the lab. Thank to Joshua Peebles, Eugene Halpin for making the TA work run smoothly.

Lastly, I would like to thank my family for their understanding of my absence; my friends and my fellow Chinese students here for their kindness, help and friendship.

CONTENTS

LIST OF FIGURES

LIST OF TABLES

Chapter 1 Introduction

1.1 Localized Surface Plasmon Resonances

Long before modern optical studies, metal nanoparticles (NPs) were used as colorant starting in ruby glass in the 5th century BC continuing through to medieval cathedral windows. One of the most cited samples is the famous Lycurgus cup (4th century AD, now at the British Museum). As an example, it is instructive to look at how the Lycurgus cup gets its color. It is known that the glass contains Au NPs, which give it its unusual dichroic look. An analysis of the cup reveals that it contains a small amount of Au and Ag NPs around 70 nm in diameter (Liz-Marzán 2004). It appears opaque green when viewed in reflected light (left panel in **Fig. 1.1**), and red when light is shone from inside and transmitted through the glass (right panel). This is associated with the localized surface plasmon resonances (LSPRs) of the metal NPs.

Fig. 1.1: Lycurgus cup, 4th century AD.

LSPRs are collective oscillations of conduction electrons across metal NPs or nanostructures. When light is incident on the particle, the oscillating electric field excites a collective oscillation of the conduction electrons, as demonstrated in **Fig. 1.2**. These excited resonances result in a strong enhancement of absorption and scattering of the electromagnetic field. The spectral position of the LSPRs depends on the composition, shape and size of the NPs as well as the

surrounding media and the presence of neighboring NPs in the visible and infrared wavelength range.

Au and Ag NPs, because of their strong LSPRs, are a focus of interest for fundamental science and are employed in a range of applications, such as chemical and biological sensors, catalysts, and agents for drug delivery (Burgin, et al. 2008; Cheng, et al. 2008; Hvolbæk, et al. 2007; Jain, et al. 2007; Masatake 1997; Paciotti, et al. 2004; Tao, et al. 2003; Turner, et al. 2008; Xiong, et al. 2006). At the heart of these exciting applications and topics are the NPs and nanostructures within which the LSPRs are excited.

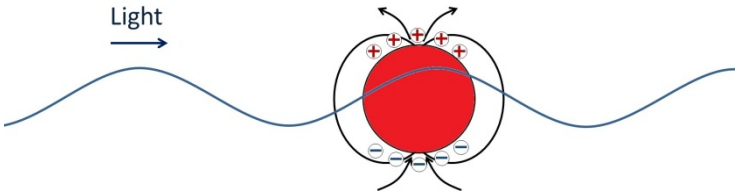

Fig. 1.2: Schematic of the electron cloud of a metal NP when excited by an external electromagnetic field.

Scattering, absorbance and extinction calculation

LSPRs of NPs can decay by emitting photons (scattering) or transferring into heat (absorption). Which pathway dominates is determined mainly by the size and shape of the NPs. The extinction (combination of scattering and absorption), scattering and absorption cross-sections (C_{ext}, C_{sca} and C_{abs}) of metal NPs are frequency dependent due to the frequency-dependent complex refractive indices. The numerical result combining Mie theory and dielectric constant of the metal particles shows that more than 99 % the LSPR energy is transferred into heat for a 20 nm diameter nanospheres (NSs) and around 90 % for 80 nm diameter NSs (Jain, et al. 2006). Mie theory (Mie 1908) is an analytical electrodynamical treatment solving Maxwell's equations of the response of a spherical metal particle to an external electromagnetic field. Using (Jain, et al. 2006),

$$
\begin{aligned}
Q_{\text{ext}} &= \frac{2}{x^2}\sum_{n=1}^{\infty}(2n+1)\text{Re}(a_n + b_n) \\
Q_{\text{sca}} &= \frac{2}{x^2}\sum_{n=1}^{\infty}(2n+1)(|a_n|^2 + |b_n|^2) \\
Q_{\text{abs}} &= Q_{\text{ext}} - Q_{\text{sca}}
\end{aligned}
\tag{1.1}
$$

$$
\begin{aligned}
a_n &= \frac{m\psi_n(mx)\psi_n'(x) - \psi_n(x)\psi_n'(mx)}{m\psi_n(mx)\xi_n'(x) - \xi_n(x)\psi_n'(mx)} \\
b_n &= \frac{\psi_n(mx)\psi_n'(x) - m\psi_n(x)\psi_n'(mx)}{\psi_n(mx)\xi_n'(x) - m\xi_n(x)\psi_n'(mx)}
\end{aligned}
\tag{1.2}
$$

where x is the size parameter given as $\frac{2\pi n_m}{\lambda}r$ with n_m the refractive index of the medium surrounding the sphere and r the radius of the sphere; ψ and ξ are Riccati-Bessel functions and m is the ratio of the refractive index between the sphere and medium, and tabulating the bulk dielectric functions of Au from (Johnson and Christy 1972), we can get the extinction, scattering, and absorption efficiencies (Q_{ext}, Q_{sca} and Q_{abs}) of NPs with different sizes in a dielectric using an algebraic program such as Mathematica. In our calculation, n = 1 to 12 in Eq. (1.1) were summed. This corresponds to summing over the first twelve electric and magnetic multipoles on the NP response to the incident field. The dimensionless efficiencies Q_{ext}, Q_{sca} and Q_{abs} can be converted to the corresponding cross-sections C_{ext}, C_{sca} and C_{abs} by multiplication with the cross-sectional area of the NP.

In our experiment analysis, we will only need the peak wavelength of the extinction spectra; therefore, we normalized the spectra for easier comparison. The calculated extinction spectra for different diameters of Au spheres in suspension are shown in **Fig. 1.3** (dotted lines). Measured extinction spectra of spheres of various diameters were taken using a fiber optic spectrometer (Ocean Optics, HR2000). By comparing the transmittance spectra of water I_0 and NP solution I, the extinction E can be obtained using

$$
E = -\log\left(\frac{I}{I_0}\right) \tag{1.3}
$$

The normalized the results are shown in **Fig. 1.3** (solid lines). The corresponding plasmon resonance peaks for 30, 60, 80 and 100 nm NSs in water are at 523, 536, 548 and 569 nm. The measured and calculated spectra are in good agreement. The fact that the experimentally obtained resonances are wider is likely due to the polydispersity of the NPs.

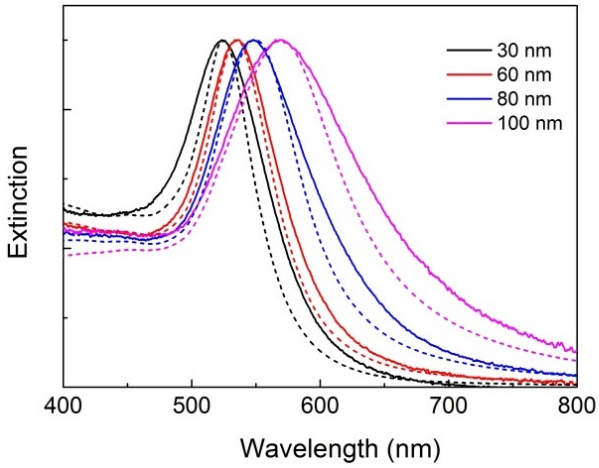

Fig. 1.3: Measured (solid) and calculated (dotted) extinction spectra of Au nanosphere suspensions of different diameters from Ted Pella.

There are many other calculations for particle shape other than sphere. Rayleigh-Gans theory is for elongated sphere (Bohren and Huffman 2007; Link and El-Sayed 1999). Discrete dipole approximation (DDA) and finite difference time domain (FDTD) methods are common means for solving Maxwell's equations in complex geometries. Commercial programs specifically intended for LSPR calculation also exist.

1.2 Thesis Outline

In Chapter 2, we discuss the synthesis of Au and Ag NPs with different shapes and the synthetic mechanism behind each class of NPs. The NPs were characterized by field-emission scanning electron microscopy (FE-SEM) or transmission electron microscopy (TEM) and their resonances were analyzed using a spectrometer. Chapter 3 is about dithiocarbamate (DTC) coating on Ag nanocubes and poly(sodium 4-styrenesulfonate) (PSS) functionalization on Au nanorods and bipyramids. Chapter 4 describes the investigation of the adsorption rate of the Au

NSs on substrates with different curvatures. Both theoretical and experimental data are presented and they are in good agreement with each other. Chapter 5 describes the plasmon resonance tuning of a Au NS-PEM film-Au substrate hybrid structure. The pH-induced swelling and shrinking of the PEM film can tune the plasmon resonances of the NSs. In Chapter 6, we describe a two-photon fluorescence imaging study of Ag triangles prepared using nanosphere lithography.

1.3 Literature Review

Many of the applications of metal NPs, especially Au and Ag, are based on LSPRs. They have played an important role in the field because they have the potential to serve as building blocks for putting nanotechnology to practical use. For example, because of their high electron density and the existence of LSPRs, they provide high contrast for both optical and electron microscopy. In this sense, Au NPs have been used in labeling to detect specific biological substances (Jain, et al. 2008; Zhao, et al. 2008; Zijlstra and Orrit 2011). Ag NPs are also of great interests for their strong LSPRs (Camargo, et al. 2010; Kelly, et al. 2002; Link and El-Sayed 1999). As mentioned in Sec. 1.1, LSPRs greatly depend on the shapes of the NPs; therefore, it is highly desirable to be able to fabricated NPs or NP arrays with a variety of shapes suitable for different applications.

Although NPs have been used since ancient times, it was not until the 1990s that fabrication and characterization tools able to engineer and study particles at the nanoscale came into existence and revived this field, termed as plasmonics (Nathan, et al. 2012; Paolo, et al. 2012 and the references therein) and the references therein. Nowadays, a variety of nanofabrication techniques, such as e-beam lithography (EBL), focused-ion beam (FIB) lithography, wet chemistry synthesis, and microscopic techniques, such as dark-field microscopy and near-field scanning optical microscopy (NSOM), have enabled the emergence of more and more fascinating research topics pushing the limits of what nanotechnology can offer to the science and technology communities.

There are primarily two approaches of fabricating nanomaterials: top-down and bottom-up methods. As indicated by the name, top-down techniques employ lithographic tools to fabricate nanostructures from the relatively large bulk materials by milling, etching or sputtering. On the other hand, bottom-up methods take advantage of sophisticated and controllable wet chemistry to assemble individual atoms to form structures at the nanoscale with the aid of various surfactants. Both top-down and bottom-up methods have their advantages and disadvantages. Top-down methods can prepare complex and highly oriented NP arrays but often involve expensive and bulky instruments and time-consuming procedures. By contrast, bottom-up methods use generic chemicals to grow 3-dimentional NPs in a relatively simple and low-cost process but come with different degree of impurities. In our work, we mainly use the bottom-up method (wet-chemistry synthesis) to fabricate our NPs.

Michael Faraday was the first person to realized that it is the NPs that make the color of Au-doped glasses and porcelain and intentionally synthesized metal NPs using chemical reactions (Faraday 1857). Almost one hundred years later, people started to study the nucleation and growth processes during the synthesis of colloidal Au (Frens 1973; Turkevich, et al. 1951). With the emergence of plasmonics (Ebbesen, et al. 1998) in the 90s, chemical synthesis of NPs started to revitalize. Over the years, people have developed a number of synthetic methods (Lu, et al. 2009; Millstone, et al. 2009; Sau and Murphy 2004 and the references therein) to grow Au or Ag NPs with a variety of shapes and compositions, such as spheres, rods (Jana, et al. 2001b), prisms (Jin, et al. 2001; Jin, et al. 2003), cages (Chen, et al. 2005), belts (Sun, et al. 2003), round disks (Maillard, et al. 2003), hollow shells (Oldenburg, et al. 1998; Zhou, et al. 1994), stars (Hao, et al. 2004), caps (Liu, et al. 2005), nanorice (Wang, et al. 2006), cubes (Sun and Xia 2002), rings (Aizpurua, et al. 2003), octahedra (Li, et al. 2007), etc.

For photochemical synthesis, Esumi *et al.* (Esumi, et al. 1995) were the first to use photochemical reduction with cationic micelles as a template to obtain anisotropic Au nanostructures. Jin *et al.* (Jin, et al. 2001; Jin, et al. 2003) showed controllable synthesis of triangular Ag nanoprisms with visible light. Mirkin et al. (Xue and Mirkin 2007) also demonstrated that adjusting the pH of the solution allowed controlling single-modal (instead of double in Jin's work in 2001) growth of the Ag prisms. It is noted that Ag prisms can also be

synthesized by thermal synthesis (Aherne, et al. 2008; Métraux and Mirkin 2005). Yin *et al*. later showed that these thermally-synthesized Ag prisms can be transformed to thick round plate by UV-light-induced reconstruction (Zhang, et al. 2009b).

Another popular bottom-up method is polyol synthesis. Although this method has been known for quite some time, it was recently revived by Xia and Yang (Sun and Xia 2002; Tao, et al. 2008; Tao, et al. 2006). In this synthetic method, the metal salt is dissolved in a type of alcohol containing multiple hydroxyl groups such as ethylene glycol (EG), which is then subjected to continuous heating. A capping agent, usually polyvinylpyrrolidone (PVP), helps to produce metal NPs with various shapes, e.g., cubes, bipyramids, wires and plates (Sun, et al. 2002; Tao, et al. 2003; Wiley, et al. 2006; Wiley, et al. 2007; Xiong, et al. 2006). In this process, the actual reductant is glycolaldehyde (GA), which is produced by the oxidation of EG in air (Skrabalak, et al. 2008). It is noted that the reaction temperature and the acidity of the solution is very critical to the final results of the experiments, even EG from different companies gives different results. The polyol synthesized nanocubes have been used as templates to prepare Au nanoboxes and nanocages by a galvanic replacement reaction (Chen, et al. 2005), which have been applied to surface enhanced Raman scattering (SERS) (Camargo, et al. 2010) and embedded in polystyrene thin film to create nanojunctions (Gao, et al. 2012), etc.

Au nanorods (NRs) and bipyramids (BPs) have drawn significant interests because they can be synthesized in a relatively simple process where rational control over the aspect ratio is possible, and they also possess large optical extinction cross-sections (Kou, et al. 2007). There are many ways of making Au NRs besides photochemical reduction (Ahmed and Narain 2010; Esumi, et al. 1995), for instance, electrochemical synthesis of Au NRs in the presence of cationic surfactants, co-surfactant, and other additives, which were found empirically to favor NRs formation (van der Zande, et al. 1999; Yu, et al. 1997).

To fabricate Au NRs and BPs, we used the seed-mediated growth methods pioneered by Murphy and El-Sayed (Huang, et al. 2009; Sau and Murphy 2004) with a small modification of the amount of added HCl to increase the stability of the NRs (Liu and Guyot-Sionnest 2005). This is a seed-mediated synthesis which means that a seed suspension is prepared first and the

seeds are later grown into larger particles in a second growth step. There are two methods developed by (Busbee, et al. 2003; Nikoobakht and El-Sayed 2003) which use the citrate-stabilized seeds or bi-surfactant system to synthesize NRs with large aspect ratios and hence redshift the LSPRs. Etching or overgrowing the NRs can also tune the LSPRs (Ni, et al. 2008). The aspect ratios of the Au BPs can be tuned by the amount of seed solution added into the growth solution (Lee, et al. 2009). The yield of the bipyramids in this synthesis can be improved with larger headgroup surfactant cetyltributylammonium bromide (CTBAB) instead of using cetyltrimethylammonium bromide (CTAB) (Kou, et al. 2007).

For many applications, the as-synthesized NPs cannot be used right away. Controlled surface functionalization of NPs with various materials is necessary to make them suitable for applications in chemical engineering, pharmaceutical and biological fields. Considering the large surface/volume ratios of the NPs, it is essential to modify their surface properties for many applications. Besides the inclusion of functional molecules for specific applications, the surface functionalization is also necessary for the colloidal stability of the particles (Bönnemann, et al. 1996; Crooks, et al. 2000; Toshima and Yonezawa 1998). For example, a monolayer coating of strong polyelectrolyte on the surface of a NP increases its surface charge density, which increases the electrostatic repulsion between the NPs, effectively preventing particle aggregations or agglomerations. In addition, the coating also changes the dielectric environments of metal particles and can shift the plasmon resonances.

Surface functionalization of NPs can be accomplished by either physisorption or chemisorption. Physisorption is the physical adsorption of molecules such as surfactants or polymers onto the surfaces of the particles usually resulting from coulomb and van der Waals forces (Caruso 2001). In particular, a significant advance in polymer coating of NP was initiated by Caruso and co-workers applying the layer-by-layer (LbL) technique to colloidal NPs (Caruso 2000; Caruso, et al. 1998; Caruso, et al. 1999a; Caruso, et al. 1999b). This approach employs sequential coating of particles with multiple layers of oppositely charged polyelectrolytes bound via electrostatic interactions.

Chemisorption, by contrast, employs chemical bonding of molecules to the surface of NPs. Due to the larger bonding energy, chemisorption generally provides greater stability for the functional layer than physisorption. We are particularly interested in dithiocarbamate (DTC) functionalization of Au and Ag NP surfaces (Morf, et al. 2005; Zhao, et al. 2009; Zhao, et al. 2005; Zhu, et al. 2008). DTC-anchored monolayers provide a more stable coating than conventional thiol chemistry and have been applied to Au planar surface or NPs for applications, such as SERS and biological imaging (Huff, et al. 2007; Tong, et al. 2007; Zhao, et al. 2009). These reports mainly focus on surface functionalization on Au surfaces while only a few studies of DTC functionalization of Ag NPs exist (Tong, et al. 2006; Yuan, et al. 2011). Therefore, we studied the surface functionalization of Ag nanocubes with DTC as detailed in Chapter 3.

As mentioned earlier, the plasmon resonance in a NP is highly dependent on the environment. When the refractive index of the surrounding medium increases, such as from air to water as in an aqueous solution, the resonance moves towards longer wavelength. In other cases, the NPs are generally placed on top of a substrate, which can be either dielectric, metallic or semiconductor. The presence of the substrate, especially a metallic one, dramatically modifies the near-field around the NPs. The simplest such case is that of a Au nanosphere sitting on or above a Au film, which has already been extensively studied both theoretically and experimentally (Aravind and Metiu 1983; Bobbert and Vlieger 1986; Driskell, et al. 2006; Fucile, et al. 1997; Johnson 1996; Le, et al. 2005; Lévêque and Martin 2006a; Lévêque and Martin 2006b; Mock, et al. 2008; Mock, et al. 2012; Mubeen, et al. 2012; Nordlander and Prodan 2004; Okamoto and Yamaguchi 2003; Schertz, et al. 2012; Wind, et al. 1987). When an external field polarizes the nanosphere, an image dipole is induced inside the substrate and interacts with the sphere. The strength of the interaction depends strongly on the size of any gap between the sphere and the film. When the gap is small, strong interactions occur leading to extremely large field intensity inside the gap, which makes this system quite attractive for several applications such as nonlinear and surface enhanced spectroscopy with active materials inserted as the spacer layer (Nagai, et al. 2012). If a thiol layer is used as the spacer, then the gap distance can be precisely controlled since the length of a thiol molecule is determined by how long the carbon chain is (Bain, et al. 1989). When the gap is in the sub-nanometer range, quantum effects start to

come into play. Recently, Smith and coworkers (Ciracì, et al. 2012) utilized this geometry and demonstrated that with a sub-nanometer gap, the non-locality of the dielectric constant has to be included in the modeling, which demonstrates the richness of the physics of this simple system.

Mock and coworkers (Mock, et al. 2012) tuned the thickness of the spacer layer between sphere and metal surface by an external electric field and modulated the interactions between the particle plasmon and the surface plasmon polariton (SPP) of the film. The applied voltage actuated an electrophoretic force on the nanosphere and increased or decreased the gap distance depending on the polarity of the voltage. However, the gap change induced in this way is small and limits the tunability. In our experiments, we used a polyelectrolyte multilayer (PEM) film as the spacer layer and employ the pH-triggered swelling/shrinking property of the PEM to tune the plasmon resonance over a large range. The swelling/shrinking property of PEM film has been extensively studied (Hiller and Rubner 2003; Tanchak and Barrett 2004; Zhang and Peppas 1999). For a PEM film consisting of strong and weak polyelectrolytes, such as PSS and PAH, which are used in our experiments, the mechanism of this swelling/shrinking behavior is driven by the changes in the degree of ionization of the free amine groups in the PAH (Itano, et al. 2005). When assembled at high pH (> 8.5), more free amines than sulfonate are included in the film. The amines subsequently become charged at low pH resulting in electrostatic repulsion between them and thus film swells as water molecules infiltrate the film to screen this charge. The charging rate of the amines is highly dependent on the pH value and therefore the film thickness is tunable with the pH. Increasing the pH from low to high shrinks the film to its original state, and this process is repeatable for many cycles (Tanchak and Barrett 2004). Depending on how many layers are in the film, the swelling/shrinking capability and thus the tunability of the spacer layer thickness can be different, providing a great tool to tune the plasmon resonance of the system.

Noble metal NPs have also been widely studied in fluorescence microscopy because they exhibit a high fluorescence signal and are not subjected to photo-bleaching or phototoxicity unlike fluorescent dye molecules or quantum dots (Yorulmaz, et al. 2012). The plasmon resonance associated with the NPs gives rise to large absorption and scattering cross-sections. The fluorescence signal from these NPs can be enhanced by several orders of magnitude (Ming,

et al. 2011). Even more intriguing are the nonlinear applications of the noble metal NPs which can be employed in 2-photon fluorescence imaging (So, et al. 2000), second harmonic generation (Gauderon, et al. 2001) and four-wave mixing imaging (Harutyunyan, et al. 2010) among other modalities. When excited, metal NPs act like antennas but working in the nanoscale regime, concentrating the incident light into nanoscale volumes resulting in extremely large electric field intensities. For 2-photon fluorescence imaging, the fluorescence signals are proportional to the square of the incident light intensity. Therefore, it is expected that the fluorescence yield of NPs should be significantly enhanced by the plasmon resonance. Indeed, this has been demonstrated in several reports (Beversluis, et al. 2003; Imura, et al. 2005; Imura and Okamoto 2009; Yorulmaz, et al. 2012).

There are a great number of reports on fluorescence from Au NPs concerning either 1-photon (Goldys and Sobhan 2012) or 2-photon fluorescence (Durr, et al. 2007; Park, et al. 2010). The fluorescence spectrum is strongly affected by the scattering properties of the NPs (Fang, et al. 2012). There are two models behind the mechanisms of fluorescence from Au NPs: the first model is based on energy transfer from electron-hole pair to a plasmon excitation (Bouhelier, et al. 2005; Dulkeith, et al. 2004; Tcherniak, et al. 2010); the second model involves internal field enhancement that the optical field created by the recombination is shared by the plasmon and enhanced by its antenna effect (Beversluis, et al. 2003; Imura, et al. 2004; Mohamed, et al. 2000). However, there are far fewer reports on fluorescence from Ag NPs (Drachev, et al. 2004; Gao, et al. 2004; Yeshchenko, et al. 2009).

Chapter 2 Silver and Gold Nanoparticle Synthesis

In this chapter, we discuss the synthesis of Ag nanoprisms, nanocubes, bipyramids; Au nanospheres, nanorods and bipyramids.

2.1 Introduction

A common top-down technique to prepare nanoparticles (NPs) is electron-beam lithography. Using this technique, a 2-dimentional NP array can be created with good orientation but the cost can be quite high. By contract, the bottom-up methods can provide large amount of NPs in a single batch and at reasonable cost. Here we focus on preparing Au and Ag NPs by using bottom-up synthetic techniques. Thanks to the well-developed literatures on this subject, we can obtain NPs of the shapes we desire with only minor adjustments of the literature methods.

In a typical chemical synthesis process, a salt solution, which contains the metal ions, is prepared. Then the metal ions are reduced by a reducing agent, UV light, microwave radiation, or by electrical current. The reduced metal atoms aggregate to form seeds in the solution and these seeds will grow into NPs with different shapes depending on the experimental conditions, e.g., the choice of capping agents, the temperature or acidity of the solution. In our work, we have used three methods—photochemical reduction, polyol-thermal synthesis and seed-mediated growth—to prepare Au and Ag NPs with different shapes.

The Au and Ag NPs discussed in this chapter are used in surface functionalization and plasmonic applications in subsequent chapters. The cleaning of the glassware is very important to the synthesis of the NPs; therefore, we begin by describing the cleaning methods, followed by a brief summary of the instrumentation we used.

Cleaning

In order to avoid unwanted particle nucleation during syntheses, the glassware needs aggressive cleaning to remove all the organic or inorganic contaminants. There are many ways to clean the glassware, for example, RCA cleaning, plasma cleaning, Piranha cleaning, aqua regia cleaning, etc. We mainly used aqua regia cleaning to clean the glassware. Aqua regia contains 3 parts concentrated hydrochloric acid (Fisher Sci., A144C-212) and 1 part concentrated nitric acid (Fisher Sci., A200C-212) and is able to dissolve organic compounds and most metallic residues. Aqua regia cleaning needs to be conducted in a fume hood with proper protection. The glassware is soaked in a freshly-prepared aqua regia solution for about 20 mins, rinsed with deionized (DI) water and usually dried with nitrogen gas. The other cleaning method that we commonly used is the plasma cleaning. The plasma cleaner (SPI Supplies, Plasma Prep II^{TM}) can remove organic residues and carbonaceous composition using an oxygen plasma. Plasma cleaning is preferred when there are no metallic residues on the glassware. The instrument is safe and easy to operate. It takes roughly 20 mins to clean the glassware.

Equipment and instruments

The DI water used in these experiments was obtained from an ultrafiltration system (Thermo Scientific, D11971) with a measured resistivity over 18 MΩ/cm and the organic contaminant level is < 1 ppb.

The extinction spectra of particles in suspension were all taken using a quartz cuvette (NSG Precision Cells, 18ES10) with an optical path of 1 cm. The transmission electron microscope (TEM) images were taken using Philips EM 420 at accelerating voltage of 120 kV and the field-emission scanning electron microscope (FE-SEM or SEM) images were taken using LEO Zeiss 1550 at accelerating voltage of 5 kV in the Virginia Tech Nanoscale Characterization and Fabrication Laboratory (NCFL). The zeta-potential (ζ-potential) measurements were taken using Zetasizer (Malvern, Nano ZS) in Prof. Richey Davis's lab in the Chemical Engineering Department and most of the extinction spectra were taken using the Perkin–Elmer Lambda 25 UV-visible spectrophotometer in Prof. Randy Heflin's lab in the Physics Department.

2.2 Silver Nanoprisms

Synthesis

Triangular Ag nanoprisms can be synthesized in a two-step photochemical reaction comprising synthesis of Ag seeds followed by photo-exciting the NS suspension with light at certain wavelengths. The Ag seeds were prepared by reducing silver nitrate ($AgNO_3$) with sodium borohydride ($NaBH_4$) in the presence of sodium citrate ($Na_3C_6H_5O_7$) and bis(p-sulfonatophenyl) phenylphosphine dihydrate dipotassium (BSPP). This synthesis method is based on the reports by Mirkin *et al.* (Jin, et al. 2001; Xue and Mirkin 2007).

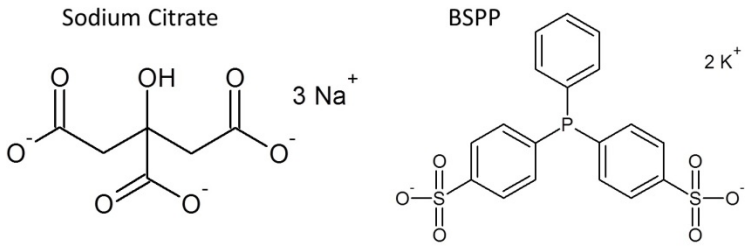

Fig. 2.1: Structures of sodium citrate and BSPP.

In the synthesis, sodium citrate and BSPP were used as stabilizing ligands (Weare, et al. 2000). BSPP is water-soluble and it oxidizes over time. During degradation, the color of BSPP solution changes from colorless to yellow and the associated extinction band at 268 nm decreases. In this case, BSPP would not be able to form a complex with Ag^+. It is interesting that without BSPP the prisms can still grow, but along with other large, irregularly shaped particles and in a much longer time. However, without sodium citrate, the prisms will not grow at all (Xue, et al. 2008). We found the presence of O_2 is necessary for the formation of Ag prisms, which is consistent with the discussion in Xue's mechanism study (Xue, et al. 2008). The major role of oxygen is to chemically convert the smaller Ag seeds into Ag^+ as in reaction (2.1), which is subsequently

$$2\ Ag^0 + O_2 + 2\ H_2O \rightarrow 2\ Ag^+ + 2\ OH^- \qquad (2.1)$$

complexed by BSPP and used as the Ag^+ source. The photochemical reaction induced by plasmon excitation has been proposed as charge transfer among BSPP-Ag^+ complex, Ag seeds and citrate. Hot electrons from the plamon mode reduce adsorbed Ag cations on the particle surfaces while hot holes are neutralized by electrons from citrate (Xue, et al. 2008).

Preparation of Ag seeds: 0.5 mL of 20 mM $AgNO_3$ (Sigma, 204390) and 1 mL of 30 mM sodium citrate (Sigma, S1804) were mixed with 95 mL DI water in a conical flask capped with a rubber septum. The flask was immersed in an ice bath, and the solution was bubbled with nitrogen in the dark with vigorous stirring for about 20 mins. After that, 1 mL of freshly prepared 50 mM $NaBH_4$ solution (Sigma, 213462) was rapidly injected into the flask. Over the next 15 mins, five drops of $NaBH_4$ solution were added into the solution. Then 1 mL of 5 mM BSPP (Strem Chemicals, 15-0463) solution and 1 mL $NaBH_4$ were added drop-wise to the flask. The resulting Ag colloid was gently stirred for 5 h in the ice bath and allowed to age overnight at 4 ºC in the dark. The seed solution was light yellow.

Transformation of Ag seeds to prisms: 20 mL of a suspension of such Ag seeds was adjusted to pH 11.2 by adding NaOH, and then illuminated by an arc lamp (Newport, 66902) through a 550 ±20 nm bandpass filter (Andover, 550FS40-50). Several illumination configurations were attempted, but we obtained the best results when the light was incident from the bottom of the vial, which was loosely capped. The intensity of the light was measured by a power meter (Newport, 1930-C) at ~10 mW/cm^2. After several hours the color of the solution became blue indicating the formation of nanoprisms.

Results and discussion

The extinction spectrum of the Ag seed suspension in **Fig. 2.2** shows a clear and narrow peak at 394 nm indicating the Ag seeds were smaller than 5 nm in diameter. This was confirmed by TEM imaging of the Ag seeds as shown in the inset. **Fig. 2.3** shows the extinction spectra taken at various times during the synthesis. The peak wavelength at 394 nm decreased over time and a new peak associated with the prisms started to form in the longer wavelength range. After 7.5 h, a peak on the spectrum appears at 680 nm while the seeds peak red-shifted slightly, which suggested the conversion was still in the initial stage. After 23 h, the 394 nm peak of Ag seeds

showed a considerable decrease while the longer wavelength peak became more pronounced, which grew into the dominant peak on the spectrum after 48 h. The sample TEM image of the NPs after 48 h of exposure is shown in **Fig. 2.4**. It is clear that the NPs were mainly in the form of triangular prisms although other shapes were also obtained, which accounted for the broadness of the peak in the spectrum. In addition, it is interesting to note that this 680 nm peak exhibited a visible blueshift as exposure time went on. This is consistent with the results in literature (Jin, et al. 2003). But we did not see a significant change of the nanoprisms after 23 h due to the limited number of prisms on TEM images.

The peak wavelength of the Ag nanoprism spectrum was in good agreement with that in the literature (Jin, et al. 2003; Xue and Mirkin 2007). However, the broadness of the peak, corresponding to large distribution of the size of the prisms, was possibly due to our less-than-perfect experimental setup so that a longer irradiation time was needed, which results in larger prisms and nipped prisms.

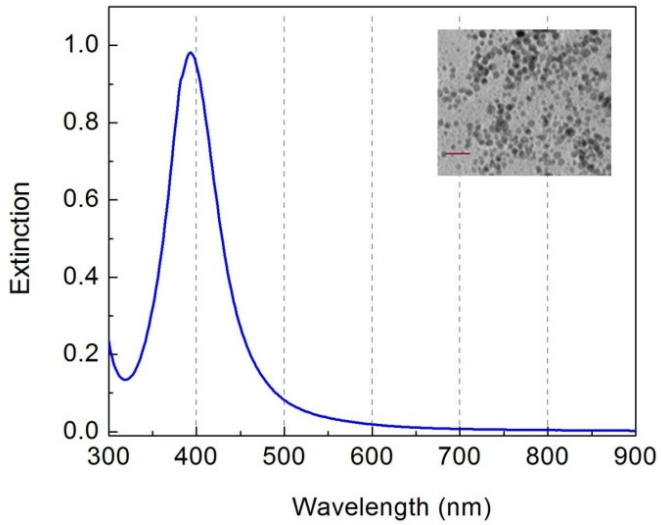

Fig. 2.2: Extinction spectrum of Ag seed solution. The inset is the TEM image of Ag seeds. The scale bar is 20 nm.

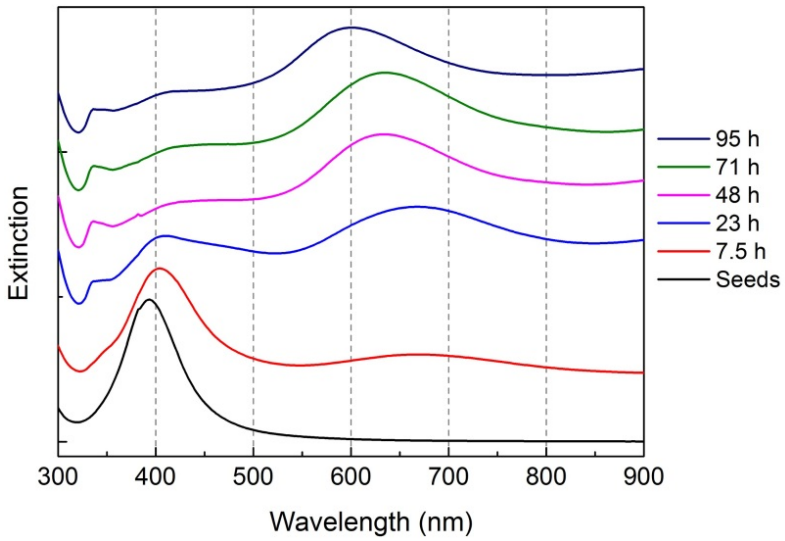

Fig. 2.3: Time-resolved extinction spectrum of the Ag seed solution illuminated by an arc lamp with a 550 ±20 nm bandpass filter.

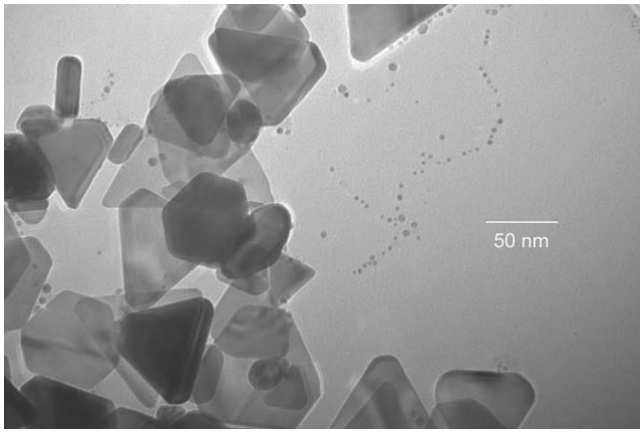

Fig. 2.4: TEM image of the Ag prisms after 48 h of illumination.

A study (Jin, et al. 2001) showed if the Ag seeds are excited with a single band of wavelength rather than two, there will be a bimodal size distribution of these nanoprisms, where one size is approximately twice as large as the other. This is associated with the dipole and quadrupole plasmon resonances of the nanoprisms. Therefore, if the Ag seeds are irradiated by dual beams with two wavelengths, one inhibits the formation of larger prisms and the other one excites the smaller prisms to form, there will be a uni-modal distribution. However, if the initial pH value of the Ag seed solution is adjusted from pH 9.5 to pH 11.2 (Xue and Mirkin 2007) as we did, with only one beam, the sample will also have a single modal distribution.

The edge length of the prisms can be tuned by changing the excitation wavelength of the light source. Mirkin *et al.* (Jin, et al. 2003; Xue and Mirkin 2007) reported tuning the LSPRs of the prisms from 500 to 750 nm by changing the excitation wavelengths from 470 to 633 nm. As discussed above, photochemical synthesis is able to fabricate Ag nanoprisms with tunable edge length. However, more experiments are expected to improve the yield and quality of the prisms.

2.3 Silver Nanocubes (Ag NCs)

Synthesis

Ag NCs can be prepared by a polyol synthesis. This is a pathway proposed by Xia *et al.* (Im, et al. 2005; Skrabalak, et al. 2008). In this process, the ethylene glycol (EG, 1,2-ethanediol) is preheated so that reaction (2.2) can happen. In this reaction, glycolaldehyde (GA) is the product of oxidation by reaction with ambient oxygen. To this preheated solution, some hydrochloric acid (HCl) is added. The GA is then be used as a reducing agent as in reaction (2.3) to reduce Ag-ions (from silver nitrate) to Ag in the presence of poly(vinyl pyrrolidone) (PVP) as capping agent.

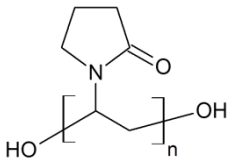

Fig. 2.5: Molecular structure of PVP. PVP is terminated in the hydroxyl group due to the involvement of water and hydrogen peroxide in polymerization which was somehow ignored by the colloidal community (Xiong, et al. 2006).

At first, both single and twinned-crystal seeds are formed in the reaction. The initial concentration of nitric acid is so high that the initially reduced Ag is dissolved back to ions as in reaction (2.4). When the nitric acid (formed by the hydrogen-ions and nitrate-ions) is gradually consumed, selective dissolution occurs. The twinned seeds are more reactive towards being etched away as a result of the lattice distortion and surface defects. This leads to enrichment of single crystalline seeds that can continue to grow into cubes.

(2.2)

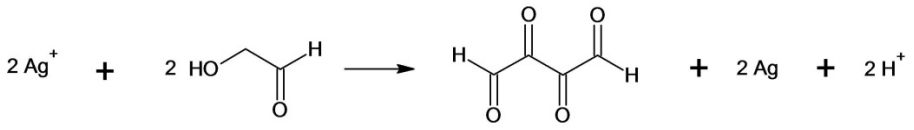

(2.3)

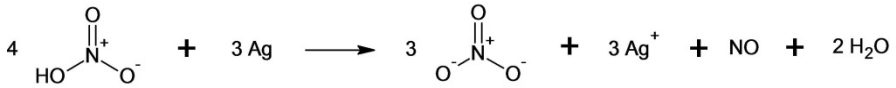

(2.4)

In a typical synthesis: 5 mL EG (J. T. Baker, 9300-01) was injected in a 15 mL long-neck spherical flask and heated in a silicone oil (Sigma, DMPS5X) bath at 140 ºC by using the feedback control of the hot plate for 1 h with magnetic stirring to remove trace of water and to cause GA to form. 2 μL of 1 N HCl was mixed with 1 mL EG (i.e. 1 mL of a 2 mM HCl in EG) and then injected to the preheated EG. After 10 mins, 3 mL of 94 mM $AgNO_3$ in EG and 3 mL of 147 mM PVP (M_W ~55,000; Sigma, 856568) in EG were simultaneously added by a syringe pump at a rate of 45 mL per hour. The flask was loosely capped afterward. We normally stopped the reaction after 5 h.

The whole synthesis reaction went through several phases, which were indicated by the color changes of the solution after adding $AgNO_3$ and PVP into the preheated EG. In the beginning it was milky white due to the formation of AgCl, and then it became yellow when Ag seeds were formed, and finally opaque ocher green when the cubes were formed. According to Xia, there is a period when the solution becomes transparent due to the complete etching of the Ag seeds. However, in our experiments, we did not observe the transparent stage. Nevertheless, the yield and quality of the Ag cubes we synthesized were good and comparable to those reported in the literature.

After quenching with water, the solution was first diluted with ethanol at a 1:1 ratio and centrifuged at 5000 rcf for 10 mins to remove the EG and excess PVP. The supernatant was substituted with same amount of water (2× of the as-synthesized solution) and ultrasonicated for less than one minute. The procedure was repeated once more. The Ag NCs were then ready for

the morphology characterization, extinction spectrum measurement and further functionalization as described in Sec. 3.2. We will refer to this as the as-prepared Ag NC suspension.

Results and discussion

A bottom-up synthesis tends to have some byproducts. The byproducts of Ag NC synthesis are bipyramids and wires. This is because in the beginning of the synthesis there are both single- and twinned-crystalline seeds. If left unetched, the twinned seeds would grow into bipyramids. Since cubes and wires are both single crystalline, there were always micron-sized wires or long wires (> 20 microns) in the synthesis depending on the HCl concentration. The synthesis of micron-sized Ag wires (Tao, et al. 2003) has a similar procedure but with higher PVP and $AgNO_3$ concentration in EG and higher molar ratio of PVP to $AgNO_3$ (6:1), and without HCl.

The extinction spectrum of 40× diluted Ag colloid taken with Perkin–Elmer Lambda 25 UV-visible spectrophotometer is shown in **Fig. 2.6**, with sharp peak wavelengths at 356, 393, 496 and a broad peak around 630 nm. Discrete dipole approximation (DDA) numerically solving Maxwell's equations for particles with arbitrary shapes has been previously applied to various nanoparticles (Yang, et al. 1995; Zhao, et al. 2008). In the DDA calculated by Zhou *et al.* (Zhou, et al. 2008), after summing over dipole and quadruple components, the plot in 1B in Zhou's paper shows that cube array with edge length > 100 nm has a very broad peak in 600 nm wavelength range. This DDA calculation was using air as the environment. We anticipate a redshift of the spectra when the environment is water (Chen, et al. 2009; Mock, et al. 2003). Therefore our spectrum of 130 nm cube solution is in the right range.

The SEM images in **Fig. 2.7** show the cleaned Ag NC colloid deposited onto a silicon substrate and dried in the ambient condition. The majority of the nanoparticles were cubes with quite uniform size distribution. The edge length of the cubes is ~130 nm. Some bipyramids and smaller cubes are also observed in the image. The inset shows a high resolution TEM image of a single cube. A natural Ag_2O layer of ~10 nm is observed under the microscope. The oxidization is similar to that seen in nickel cubes (LaGrow, et al. 2011). As shown in **Fig. 2.7B**, micron-sized wires were also present at a small fraction of the product. The micron-size wires' resonances are between 480 to 640 nm (Tao, et al. 2003) which overlap with Ag cubes' resonances. Therefore, it

is not easy to distinguish the influence of the presence of Ag wires to the spectra. Considering that cubes are the major products, we believe that the spectrum in **Fig. 2.6** represents the optical response from Ag cubes. The average zeta-potential (ζ-potential) of the cubes is about −30 mV. More details about ζ-potential measurement can be found in **Fig. 3.3** in Chapter 3.

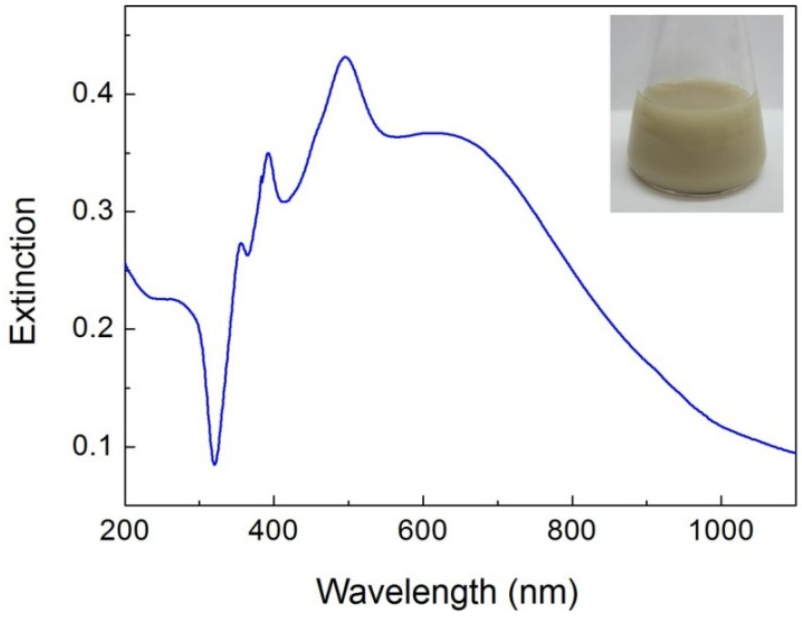

Fig. 2.6: Extinction spectrum of Ag cubes with edge length ~130 nm in suspension and the inset is the photo of the as-synthesized Ag cube suspension.

Silver cube synthesis is very sensitive to the presence of HCl. When preparing the 1 mL HCl adjusted EG, we scaled up the volume 10 times for accuracy and took 1 part to add into the pre-heated EG. In addition, the pH values of the initial EG solvent from different companies were different. Since EG is an organic compound, DI water was added to EG (highly water miscible) at a 1:1 ratio when measuring the pH of the EG at room temperature. The pH of the EG from Sigma (324558) was ~pH 9; while the one from J. T. Baker, which was used in the synthesis section, was ~pH 6. This difference can be attributed to different amount of metal ions such as Fe in the EG. It is important to be aware of this difference because the pH value of the solution is very critical to the final product yield of the synthesis. However, by adding the right amount of HCl, both EG solvents worked.

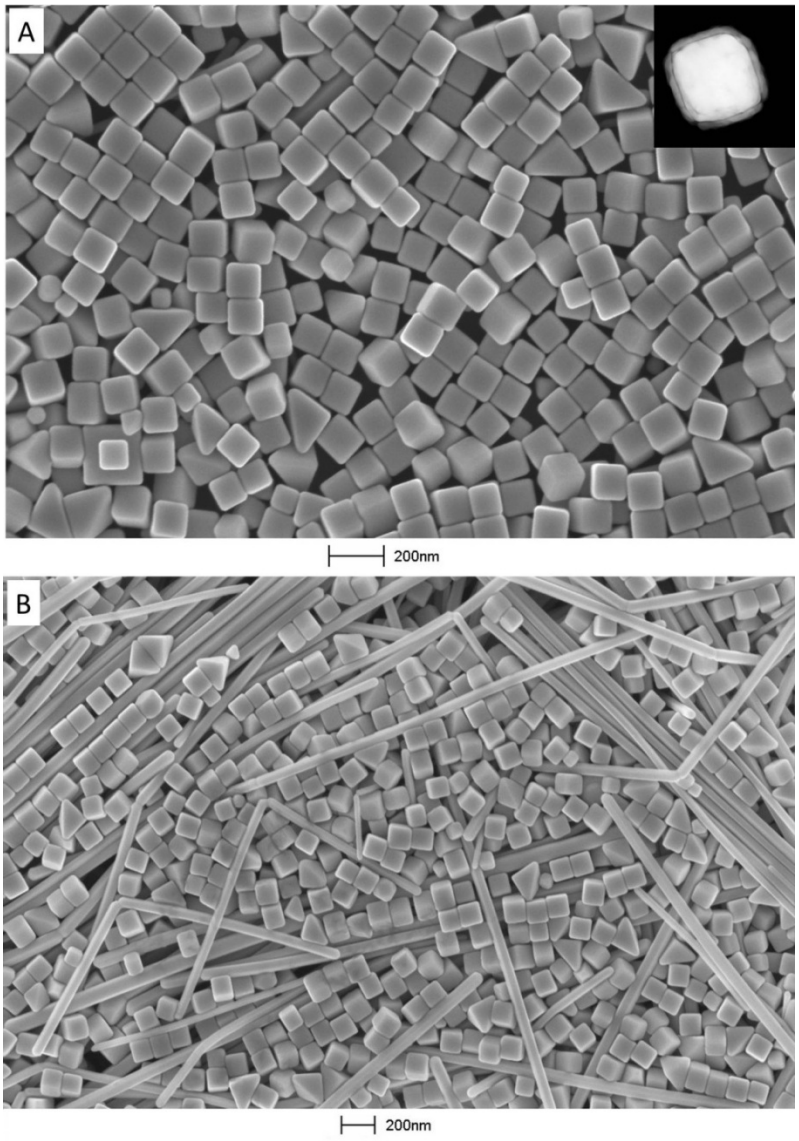

Fig. 2.7: SEM images of Ag cubes at different magnifications from different areas of sample substrate. (EG from J. T. Baker, 2.0 µL of 1 N HCl added, Reaction time: 5 h) The inset in **A** is the HR-TEM image[i] of a single cube. The exterior Ag_2O layer protects Ag cube from further oxidation.

As EG from J. T. Baker was more acidic than that from Sigma, so less HCl was needed. The EG used in the synthesis of the cubes in **Fig. 2.7** was from J. T. Baker with 2.0 µL of 1 N HCl added as described in the synthesis section. Based on our experience, 2.0 to 2.5 µL of HCl for 1

[i] The high resolution TEM image of silver cube was the courtesy of Dr. Niven Monsegue at ICTAS.

mL EG from J. T Baker and 5.5 to 6.0 µL for EG from Sigma would lead to the formation of cubes as the major product. **Fig. 2.8** shows SEM images of Ag cubes made with EG from Sigma with 5.8 µL of HCl added. The synthesis was terminated after 4 h. Even though the sizes of the cubes were not uniform, the cubes were of high quality, and they were much larger than those made of J. T. Baker's EG.

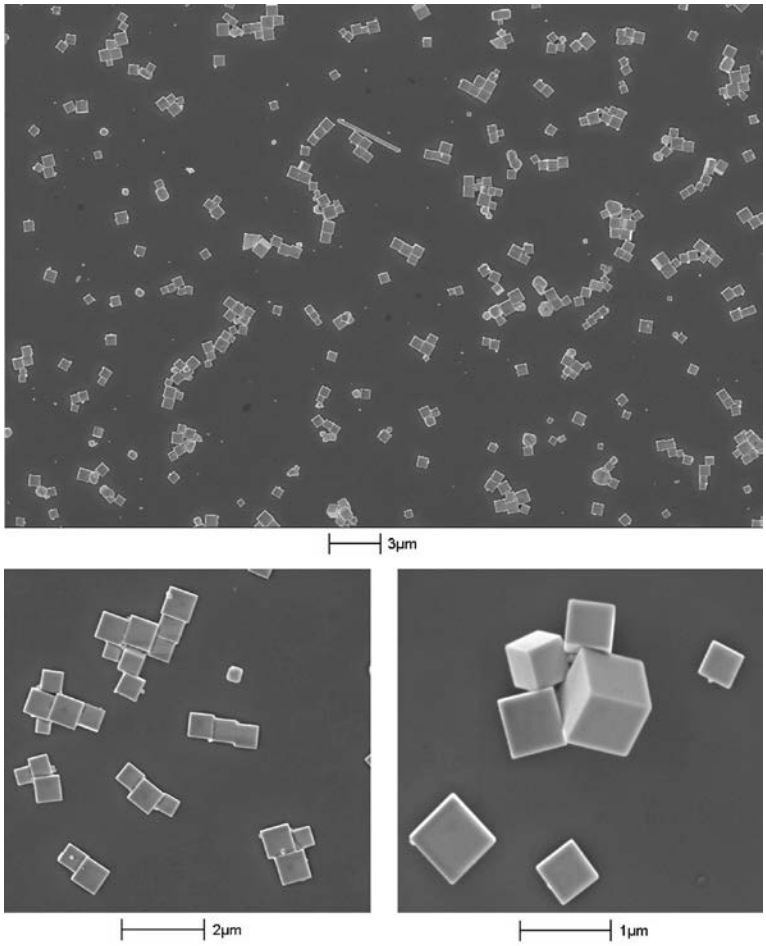

Fig. 2.8: SEM images of Ag cubes at different magnifications from different areas of sample substrate. (EG from Sigma, 5.8 µL of 1 N HCl was added. Reaction time: 4 h)

If extra HCl is added, wires will become the dominant product in the solution with both EGs. For example, in Xia's paper (Im, et al. 2005), the authors used 3.0 µL of HCl for the EG from J. T. Baker. When we used 3.0 µL of 1 N HCl for the synthesis, we got an opaque gray-green solution containing a white precipitate in the bottom after 3 to 4 hours, which was later verified to be Ag wires under SEM as shown in **Fig. 2.9**. There were very few cubes in the solution.

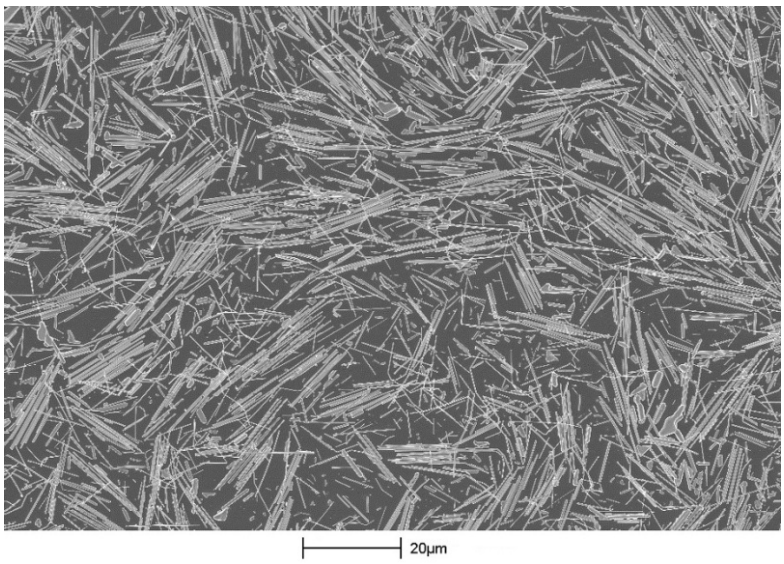

Fig. 2.9: SEM image of Ag wires. (EG from J. T. Baker, 3.0 µL of 1 N HCl added. Reaction time: 7 h)

Oxygen is also an important factor during synthesis. Taguchi *et al.* (Taguchi, et al. 2008) reported that the amount of oxygen injected during synthesis can change the formation of the nanoparticles from amorphous to wires and cubes. According to the paper, the presence of oxygen effectively promotes the oxidative etching and reduces the growing speed of nanoparticles. We did not try to control the oxygen flow, but we synthesized all the cubes in a single type of vial, which was loosely covered by an aluminum foil.

The size and shape of the cubes can also evolve when additional $AgNO_3$ and PVP added into the solution (Tao, et al. 2006; Zhang, et al. 2010b). And with different capping agent (Zeng, et al. 2010) or different reducing agent (Skrabalak, et al. 2008), the results will also be different.

2.4 Silver Bipyramids (Ag BPs)

Synthesis

The synthesis of Ag BPs is very similar to that of Ag nanoprisms. It is also a plasmon-mediated synthesis. Ag BP is consisting of two tetrahedra symmetrically joined base-to-base. The materials for photochemical synthesis of Ag BPs were very similar to those of Ag prisms in

Sec. 2.2, only with different concentrations and no sodium borohydride added. This synthesis was based on the method developed by Mirkin *et al*. (Zhang, et al. 2009a).

Preparation of the seed solution: In a typical synthesis, 17.7 mL of DI water, 600 µL of a 10 mM aqueous $AgNO_3$ solution, 1 mL of a 30 mM sodium citrate solution, 600 µL of 10 mM bis(p-sulfonatophenyl) phenylphosphine dihydrate dipotassium salt (BSPP) and 100 µL of 1 N NaOH were mixed in a 20-mL clean vial under magnetic stirring. Then the vial was irradiated by an arc lamp with a 550 ±20 nm bandpass filter as in the Ag prisms synthesis in Sec. 2.2. The irradiation was stopped after 22 h or less.

1 mL of the as-synthesized Ag BP solution was centrifuged at 5000 rcf for 10 mins and the supernatant was replaced by DI water to remove the excess BSPP for further characterization.

Results and discussion

The size and morphology of plasmon-mediated Ag bipyramids and prisms greatly depend on the [BSPP]/[Ag^+] ratio and the pH of the seed solution (Zhang, et al. 2010a). The sturcture of BSPP is shown in **Fig. 2.1**. BSPP is a water-soluble triarylphosphine that forms coordination complexes with Ag^+. To make Ag bipyramids, the pH value should be higher than 10, which is why NaOH was added to adjust the pH of the seed solution to 10.5. We also mantained the ratio [BSPP]/[Ag+] = 1.

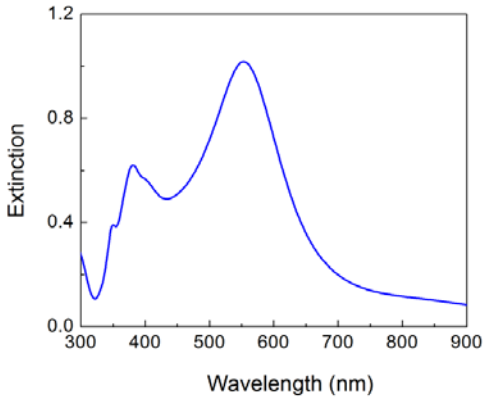

Fig. 2.10: Extinction spectrum of the Ag BPs in suspension. The peak wavelengths are 350, 381 and 553 nm.

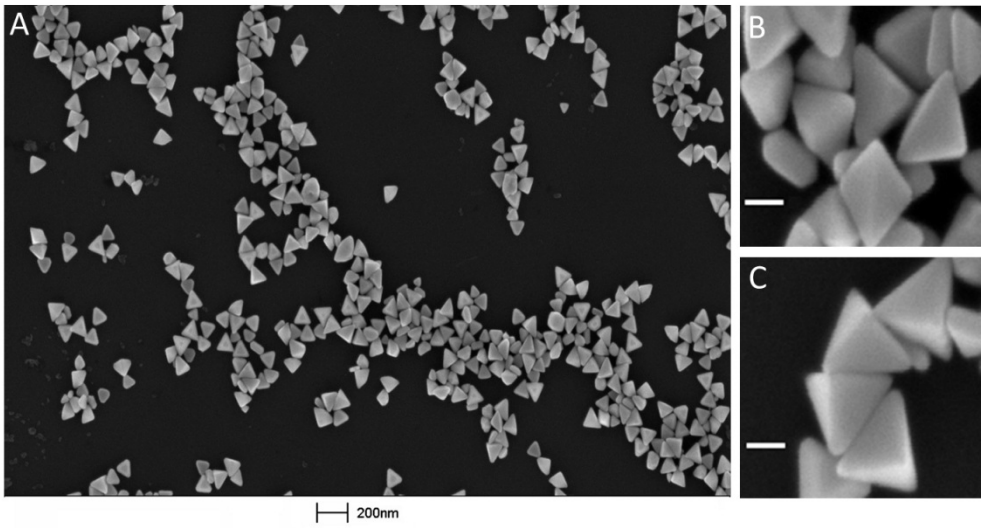

Fig. 2.11: SEM images of Ag BPs. B-C) Higher magnification images. The scale bars are 50 nm in B and C.

Fig. 2.10 shows an extinction spectrum of Ag BPs in suspension. The peak wavelengths are 350, 381 and 553 nm. **Fig. 2.11** shows an SEM image of the BPs on a silicon wafer.

The plasmon resonance in the BPs can be tuned by changing the optical filter used during growth. With the excitation wavelength changes from 550 to 650 nm, the longest peak wavelength (dipole resonance) will shift from 540 to 700 nm (Zhang, et al. 2009a).

2.5 Gold Nanospheres (Au NSs)

2.5.1 Citrate-Stabilized Method

This method was developed by G. Frens in 1973 (Frens 1973). NSs can be prepared by reducing chloroauric acid ($HAuCl_4$) with $NaBH_4$.

The Au NSs are prepared with solution of 0.01 % $HAuCl_4$ (by weight, 0.25 mM, Alfa Aesar, 42803) and 1 % sodium citrate (by weight, 34 mM). 50 mL of the 0.01 % $HAuCl_4$ solution was heated to boiling, and then an additional amount of sodium citrate was added depending on the desired particle size. The Au salt solution was kept in an Erlenmeyer flask covered with an

aluminum foil while heated under magnetic stirring. When the salt solution was boiling, the sodium citrate solution was injected into the flask. After 5 mins, the flask was moved away from the hotplate and allowed to cool. The sizes of the resulting Au spheres depend on the amounts of citrate that are used. **Fig. 2.12** shows the relationship between the amount of sodium citrate and its corresponding average diameter of the spheres as reported by Frens.

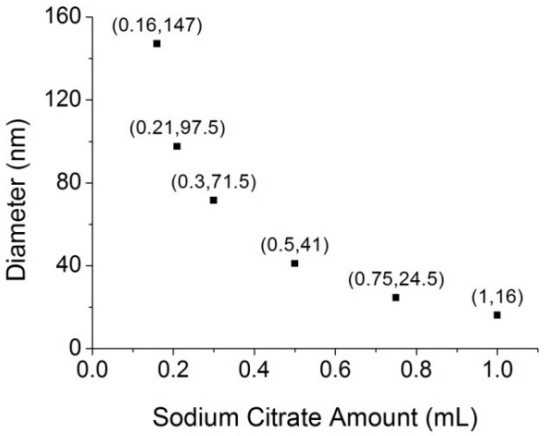

Fig. 2.12: Plot of the amount of 1 % sodium citrate solution used in the Au NS synthesis and the resulting diameter of the Au NSs (Frens 1973).

Results and discussion

In our case, 0.25 mL of 1 % sodium citrate solution was added in order to get the average sphere size around 80 nm in diameter. The pH of the as-synthesized citrate stabilized NSs at this size was 3.5. For smaller spheres, more citrate is needed and the pH will be lower. The extinction spectrum in **Fig. 2.13A** shows a resonance peak at 549 nm. The 80 nm Au sphere solution obtained from Ted Pella in **Fig. 1.3** shows a resonance peak at 548 nm peak, but with a much narrower full-width-at-half-maximum (FWHM). This means the spheres we made had a larger size distribution. The SEM image in **Fig. 2.13B** shows the citrate-stabilized spheres. The average ζ-potential of these NSs was around –30 mV because of the citrate. The citrate-stabilized NSs were not spherical, but oval. For smaller spheres prepared by Jason Ridley and Erich See in our lab using the same method, the shapes were not spherical either as shown in the TEM images in

C and **D**. The spheres were not very useful for the applications that we needed for later experiments.

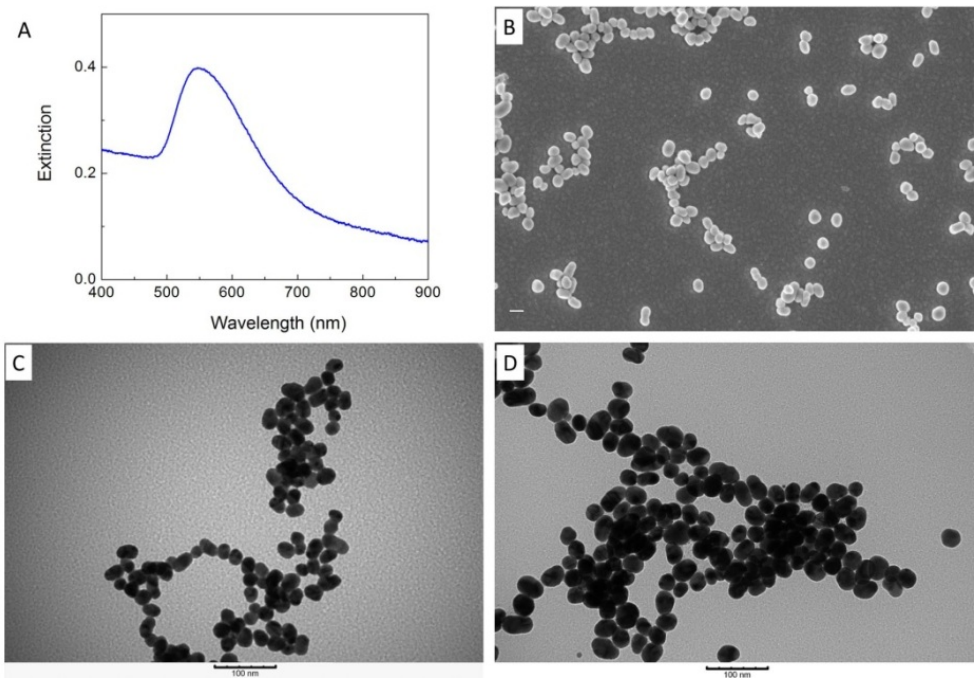

Fig. 2.13: A) Extinction spectrum of 2× diluted citrate-stabilized Au NSs. B) SEM image of 80 nm spheres corresponding to A. The scale bar is 100 nm. C) TEM image of 20 nm spheres. D) TEM image of 30 nm spheres[ii].

In literature (Perrault and Chan 2009), if another weak reducing agent, hydroquinone (benzene-1,4-diol, $C_6H_4(OH)_2$), is used with proper amount, spherical Au NSs from 2 to 200 nm in diameter can actually be obtained. Due to time-constraints, we did not attempt to verify this method.

2.5.2 CTAB-Stabilized Method

Gold NSs can also be prepared by the seed-mediated method developed by Jana *et al*. (Jana, et al. 2001a). The Au seeds (~3.5 nm in diameter) can be prepared by reducing chloroauric acid

[ii] The 20 and 30 nm Au NS suspensions were prepared by Jason Ridley and Erich See.

($HAuCl_4$) with sodium borohydride ($NaBH_4$) in the presence of sodium citrate. The growth solution can be prepared by heating and cooling the mixture of chloroauric acid and hexadecyltrimethylammonium bromide (CTAB). With this method 5–40 nm NSs can be prepared and they are spherical in shape.

The chemical structure of L-ascorbic acid is shown in **Fig. 2.14**. The molecular structure of CTAB can be found in **Fig. 2.18**.

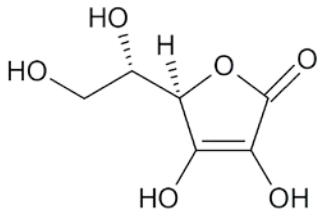

Fig. 2.14: Molecular structure of L-ascorbic acid.

Preparation of Au Seeds: A 20 mL solution containing 0.25 mM $HAuCl_4$ and 0.25 mM sodium citrate was prepared in a conical flask. Next, 0.6 mL of on ice-cold, freshly prepared 0.1 M $NaBH_4$ solution was added to the solution while stirring. The solution turned pink immediately after adding $NaBH_4$. The particles in this solution were used as seeds within 2–5 h after preparation. Unlike the citrate-stabilized method, sodium citrate here serves only as a capping agent because it does not reduce $HAuCl_4$ at room temperature.

Preparation of the growth solution: A 200 mL solution containing 0.25 mM $HAuCl_4$ and 80 mM CTAB (Sigma, H9151) was prepared in a conical flask. The mixture was heated until the solution turned to a clear orange color (close to boiling). The solution was then cooled to room temperature and used as the growth solution.

In a flask (denoted A), 0.05 mL of 0.1 M L-ascorbic acid was added into 7.5 mL of the growth solution. Then, 2.5 mL of the seed solution was added into this flask while stirring. After 10 mins, the solution turned wine red. The NSs formed at this stage were around 5.5 nm.

Next, 0.05 mL of 0.1 M L-ascorbic acid was added to another flask (denoted B). Then 1 mL of NS solution from A was added into this flask. After 10 mins, the solution turned dark red. The

resulting NSs were around 8.0 nm in diameter. Then the process can be repeated once (C) or twice more (D) to make larger spheres. Beyond that, nanoparticles with other shapes will become dominant. The average size of spheres in D is about 40 nm according to the literature, and there will be a small portion of Au nanorods in solution. Therefore we prepared solution C for our use.

1 mL of the as-synthesized CTAB-stabilized Au NS solution was centrifuged at 15000 rcf for 10 mins and the supernatant was replaced with DI water to remove the excess CTAB for further characterization and application.

Results and discussion

L-ascorbic acid is a mild reducing agent and it can only reduce the Au after the seeds (nucleation cites) are added.

We anticipated spheres with an average diameter of 17 nm in solution C. In the TEM images in **Fig. 2.15**, the average diameter of the spheres was larger than 17 nm. We also got some triangular shape nanoparticles. We also found out these NSs were penta-twinned crystals as in image **C**.

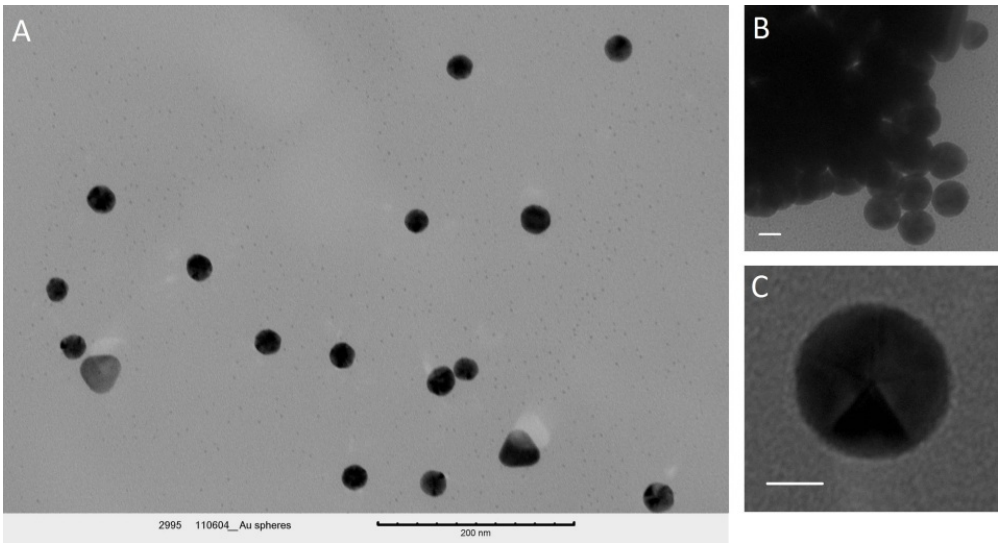

Fig. 2.15: TEM images of CTAB-stabilized Au NSs. Scale bars in B) and C) are 10 nm.

The CTAB-stabilized Au NSs were later surface-functionalized with poly(sodium 4-styrenesulfonate) polystyrene (PSS, a strong anionic polyelectrolyte) using the method described in Sec. 3.3 for Au nanorods in order to reduce aggregation when the nanoparticles adsorbed onto a modified substrate. Unfortunately, the spheres were still subject to aggregation after PSS coating. We were unable to use these spheres for our experiments but they may still be useful for other applications.

2.6 Gold Nanorods (Au NRs)

Synthesis

Short Au NRs can be prepared by a seed-mediated method (Liu and Guyot-Sionnest 2005). The standard procedure is preparing a seed solution first and adding the seed solution to another growth solution. The seed solution is prepared by using sodium borohydride ($NaBH_4$) as a reducing agent to reduce the Au salt dissolved in a hexadecyltrimethylammonium bromide (CTAB) solution. (CTAB was also used in synthesizing CTAB-stabilized Au NSs in previous section. Its molecular structure is shown in **Fig. 2.18**.) The resulting seeds are mostly single crystalline. The growth solution is a mixture of chloroauric acid ($HAuCl_4$), silver nitrate ($AgNO_3$) and CTAB. HCl is used to acidify the growth solution to prevent later overgrowth, which has been described by Wei *et al.* (Zweifel and Wei 2005). The Ag ions assist the growth of NRs, but their role is not well understood. L-ascorbic acid is used as a mild reducing agent to reduce Au(III) to Au(I). After adding the seeds as nucleation sites, the NRs start forming. CTAB adsorbs preferentially onto the {110} and {111} facets of the Au NPs in a bilayer form, therefore confining the growth direction of the NRs to the [001] direction (Chen, et al. 2009; Nikoobakht and El-Sayed 2003).

Preparation of Au seeds: 0.25 mL of 10 mM $HAuCl_4$ was mixed with 10 mL of 0.1 M CTAB. Then, 0.60 mL of freshly prepared 10 mM $NaBH_4$ was quickly injected into the solution under vigorous stirring. The mixture was stirred for 5 mins for the complete decomposition of $NaBH_4$.

Preparation of the growth solution: To a 10 mL of 0.1 M CTAB solution, 0.5 mL of 10 mM $HAuCl_4$ and 0.1 mL of 10 mM $AgNO_3$ were added. The solution was then acidified with 0.2 mL of 1 N HCl, followed by the addition of 0.08 mL of 0.1 M L-ascorbic acid. After mixing, 24 µL of seed solution was injected into the growth solution. The reaction was performed at 30 °C under gentle stirring. The reaction was allowed to proceed at 30 °C under gentle stirring for up to 2 h.

1 mL of the as-synthesized Au NR suspension was centrifuged at 5000 rcf for 10 mins and the supernatant was replaced by DI water to remove the excess CTAB for further characterization and application.

Results and dissussion

The short Au NR synthesis is very mature and can reach 95 % purity. **Fig. 2.16A** shows the extinction spectrum of short Au NRs in suspension taken by the Ocean Optics HR2000 fiber optic spectrometer. The peak at 817 nm is the longitudinal plasmon mode resonance of the Au NRs and 509 nm is the transverse plasmon mode resonance. NRs at this size and aspect ratio, the extinction spectrum is mostly attributed to absorbance rather than scattering (He, et al. 2010). The spectrum contains a small shoulder around 570 nm. This is due to nanoparticles with other shapes, e.g. cubes in the suspension. The inset shows the photo of as-synthesized Au NR solution in a conical flask. **Fig. 2.16B** shows a TEM image of the Au NRs.

The longitudinal mode strongly depends on the aspect ratio (AR) of the Au NRs. Based on DDA simulations, the relation between LSPR peak, λ_{max}, and AR is experimentally determined by $\lambda_{max} = 96\,\mathrm{AR} + 418$ (nm) (Brioude, et al. 2005). With the extinction peak at 817 nm, we can estimate that the average aspect ratio of the NRs is around 4. Short Au NRs (AR < 7) are octagonal enclosed mainly by {100} and {110} facets and their axial growth direction is [001]. NRs with larger AR have different crystallographic structure (Gai and Harmer 2002; Wang, et al. 1999).

There are several methods to tune the LSPR of the NRs. To shorten the LSPR (decrease AR), the as-synthesized NRs can be etched by hydrogen peroxide. Alternatively, cysteine

($HO_2CCH(NH_2)CH_2SH$, an α-amino acid) can be used to mediate overgrowth of the NRs, which can tune the LSPR from 820 nm to 600 nm (Ni, et al. 2008). Adjusting the concentration of $AgNO_3$ in the growth solution can also tune the AR of the NRs (Zweifel and Wei 2005).

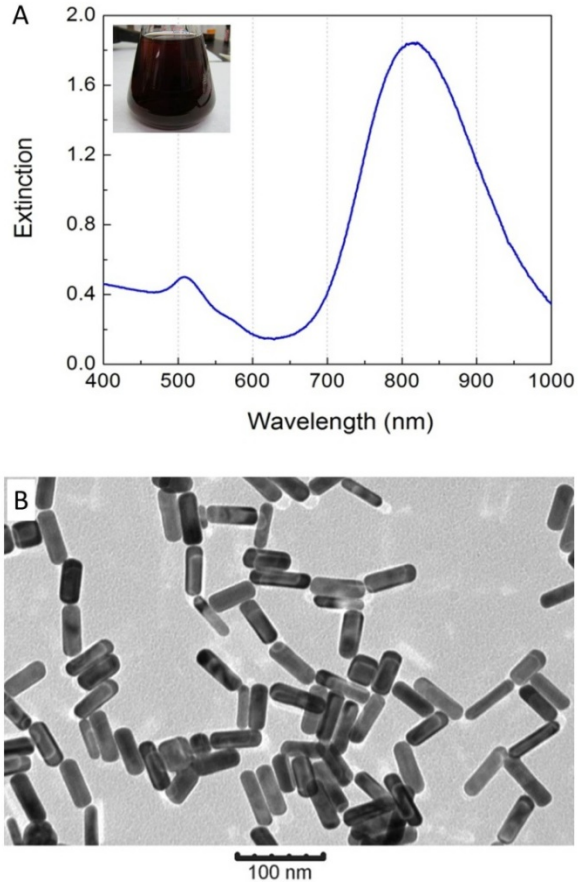

Fig. 2.16: A) Extinction spectrum of Au NRs in suspension. The inset is a photo of as-synthesized Au NR suspension. B) TEM image of Au NRs.

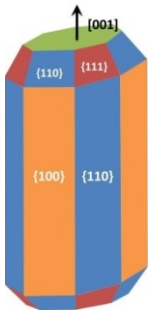

Fig. 2.17: Crystallographic structure of short Au NRs.

To lengthen the LSPR (increase AR) of the NRs, we used the method developed by El-Sayed *et al*. (Nikoobakht and El-Sayed 2003) with a binary surfactant system and also the method developed by Jana *et al.* (Jana, et al. 2001b) synthesizing Au NRs without the presence of Ag ions in the growth solution. These two methods will be discussed in sequence.

Binary surfactant system: Benzylcetyldimethylammonium chloride (BDAC, Alfa Aesar, 32377) was introduced to the growth solution along with CTAB. The concentration of the surfactant for the synthesis is far above the 2nd critical micelle concentration (CMC). The surfactant forms rod-like micelle (Imae, et al. 1985; Mock, et al. 2003). Possibly because BDAC has larger head group than CTAB as can be seen in **Fig. 2.18**, the reduction of the Au-surfactant complex is slowed. The rods can therefore be narrower and longer. The bromide ions of CTAB also play a role in the NR synthesis, so if only BDAC was present, the NRs cannot form (Nikoobakht and El-Sayed 2003).

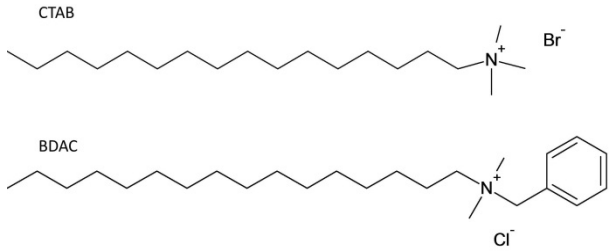

Fig. 2.18: Molecular structures of CTAB and BDAC.

To synthesize NRs using this method, the same seed solution as for the short NRs was added into the growth solution with specific ratio of BDAC/CTAB. By changing the ratio of BDAC/CTAB from 16 to 2, NRs with LSPR ranging from 900 to 1300 nm can be made. In our test, we prepared a 5 mL surfactant solution containing 150 mM BDAC and 1 g CTAB, which is equal to 55 mM, making the BDAC/CTAB = 2.7. After mixing with 5 mL of $HAuCl_4$, the total surfactant concentration was 100 mM, which was close to the CTAB concentration for short NRs.

The extinction spectrum (blue line) in **Fig. 2.19A** did not show the redshift as described in the paper after a week. For this specific synthesis, the LSPR peak was at 850 nm, which was far from the value we expected—1200 nm. After several trials, we obtained LSPRs in the 900 nm range. For future trials, we will increase the concentration of CTAB to 100 mM as for short NRs

and add corresponding amount of BDAC since there was perhaps not enough bromide ions in the solution. The TEM image in **Fig. 2.19B** shows that the byproducts of the binary surfactant synthesis were cubes. By centrifugation or filtration, the NRs can be separated from cubes.

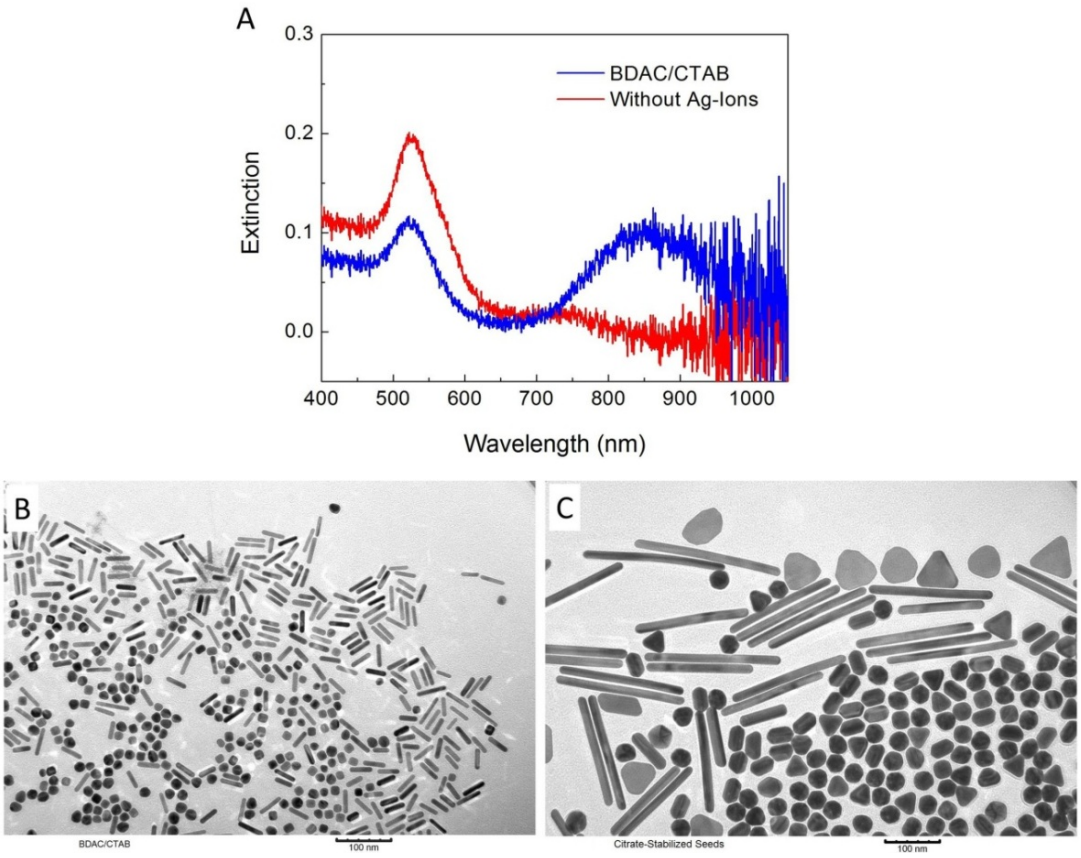

Fig. 2.19: A) Extinction spectra of Au NRs from a binary surfactant growth system and a growth solution without Ag-ions. TEM images of B) Au NRs grown from BDAC/CTAB binary surfactant system; C) long Au NRs synthesized without Ag-ions.

Without Ag ions: To synthesize Au NRs without Ag ions in the growth solution, another seed solution needs to be prepared. The seed solution for this synthetic method is different from that for short NRs and binary surfactant system. Instead, we use the citrate-stabilized seeds for the CTAB-stabilized NSs in Sec. 2.5.2. A three-step seeding method similar to that section was used: Three flasks were labeled as A, B and C. To each flask, a 9 mL growth solution containing 0.25 mM $HAuCl_4$ and 0.1 M CTAB and 0.05 mL of 0.1 M L-ascorbic acid were added. Next, 1.0 mL seed solution was added into flask A. After 4–5 h, 1 mL of solution A was added into B.

After 4–5 h, 1 mL of solution B was added into C. Solution C turned red in color within 10 mins and was stable for over a month.

In this work, there was no $AgNO_3$ added and the ratio of L-ascorbic acid to $HAuCl_4$ was 2.2, higher than that for the short NRs synthesis, where it was 1.6. The extinction spectrum (red line) in **Fig. 2.19A** was not able to show the LSPR due to the limitation of our spectrometer. The yield of the synthesis was very low. The yield can be improved by raising the pH of the growth solution (Busbee, et al. 2003). **Fig. 2.19C** shows a typical TEM image of the NRs and other byproducts synthesized this way. The separation of the NRs from other byproducts is also possible through centrifugation.

2.7 Gold Bipyramids (Au BPs)

Synthesis

Au BPs are nanoparticles with a penta-twinned crystal structure. Au BPs can be prepared by a seed-mediated method. The growth solution for making the BPs is same as the one for making short Au NRs; the difference lies entirely with the seed preparation. When preparing the seed solution, instead of CTAB, sodium citrate is used as the stabilizer for the preparation of the twinned-crystal seeds (Liu and Guyot-Sionnest 2005). The reducing agent is still $NaBH_4$, however, the amount is half of that used in the short NR synthesis.

Preparation of the seeds: To a 20 mL solution containing 0.125 mM $HAuCl_4$ and and 0.25 mM sodium citrate, 0.3 mL of 10 mM freshly prepared $NaBH_4$ solution was added under vigorous stirring at room temperature. The seed solution was then aged for at least 2 h before use.

Preparation of the growth solution: To 10 mL of a 0.1 M CTAB solution, 0.5 mL of 10 mM $HAuCl_4$ and 0.1 mL of 10 mM $AgNO_3$ were added. The solution was then acidified with 0.2 mL of 1.0 M HCl, followed by the addition of 0.08 mL of 0.1 M L-ascorbic acid. Either 80 µL or 12 µL of the seed suspension was then injected. The reaction was allowed to proceed at 30 °C under gentle stirring for up to 2 h.

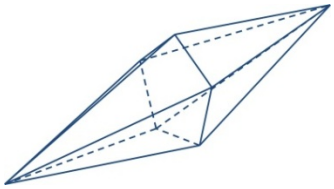

Fig. 2.20: Sketch of a Au bipyramid.

1 mL of the as-synthesized Au BP solution was centrifuged at 5000 rcf for 10 mins and the supernatant was replaced by DI water to remove the excess CTAB for further characterization and application.

Results and discussion

Au BPs have very high extinction cross-sections, as much as five times higher than the short Au NRs, and have the highest maximal electric-field-intensity enhancement among short and long NRs (Kou, et al. 2007). This makes the penta-twinned BPs very interesting. There is still room for yield improvement. The yield is currently around 50 % and it requires some efforts to separate the byproduct since the dimension of the byproduct (which consists of spheroidal particles) is very close to that of the BPs. According to Wang and coworkers (Kou, et al. 2007), the yield of the bipyramid synthesis can be improved by using a larger headgroup surfactant, cetyltributylammonium bromide (CTBAB), instead of using CTAB. However, CTBAB is not commercially available.

The LSPRs of the Au BPs can be tuned by adding different amounts of seed suspension into the growth solution (Lee, et al. 2009). We synthesized BPs using either 80 µL or 12 µL of seed suspension, where the larger amount results in lower aspect ratio particles and shorter wavelength LSPRs. The extinction spectra of the two Au BP suspensions taken using a Perkin–Elmer Lambda 25 UV-visible spectrophotometer and an Ocean Optics Fiber spectrometer are shown in **Fig. 2.21A** (80 µL seed suspension) and **D** (12 µL seed suspension). In **Fig. 2.21A**, the two peaks at 552 and 804 nm are associated with the transverse and the longitudinal LSPRs of the Au BPs, respectively. The shorter wavelength peak also has contributions from the spheroids. **Fig. 2.21B** and **C** show TEM images of the small aspect ratio Au BPs, and **E** and **F** show the TEM images of large aspect ratio Au BPs. As can be seen in **D**, peak wavelength of in large

aspect ratio BPs occurs beyond the limit of the fiber optic spectrometer that we used for this measurement.

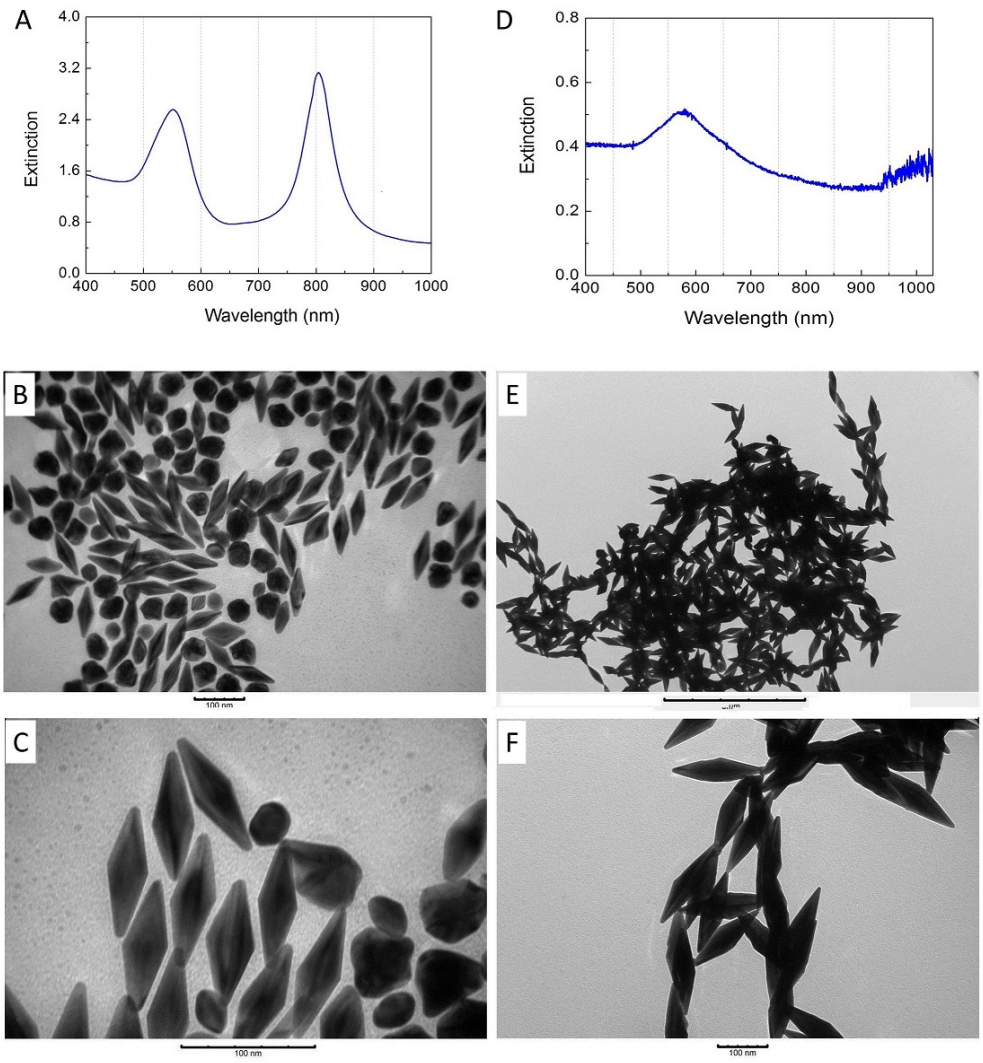

Fig. 2.21: A) Extinction spectrum Au BPs with smaller aspect ratios in suspension and B-C) the corresponding TEM images. D) Extinction spectrum of Au BPs with larger aspect ratios in suspension and E-F) the corresponding TEM images.

2.8 Conclusion

The methods we have used in this chapter are far from the only ways to make the various types of nanoparticles we have synthesized. A very large variety of metal nanoparticles can be

synthesized by plasmon-mediated, thermal, lithographic, and other methods. We chose methods which fit our lab conditions. With the help of literature, we were able to synthesize NPs for our needs with a good understanding of their surface properties. There is still room to improve the NPs preparation, e.g., separation of product from the impurities, and making spherical NSs.

Chapter 3 Surface Functionalization

In the first part of this chapter, we focus on the surface functionalization of Ag nanocubes (NCs) and bipyramids (BPs) with poly(allylamine hydrochloride) (PAH) and poly(allylamine hydrochloride)-dithiocarbamate (PAH-DTC). Previously, we have successfully demonstrated robust PAH-DTC surface functionalization on Au nanospheres (NSs) (Chen and Robinson 2011). In this chapter, we applied the protocol to Ag NCs and BPs and found that the PAH-DTC actually shrinks the Ag NCs. In the second part of the chapter, we will describe the physisorption coating of a strong polyelectrolyte poly(sodium 4-styrenesulfonate) (PSS) on CTAB-stabilized Au nanorods (NRs) and discuss the applications of these NRs.

3.1 Introduction

Noble metal nanoparticles (NPs) have been employed in many applications, such as surface enhanced spectroscopy, chemical/biological sensors, imaging contrast agents, and drug delivery carriers (Burgin, et al. 2008; Camargo, et al. 2010; Cheng, et al. 2008; Haruta 1997; Huff, et al. 2007; Hvolbæk, et al. 2007; Jain, et al. 2007; Paciotti, et al. 2004; Tao, et al. 2003; Tong, et al. 2007; Zhao, et al. 2009). In all cases, proper functionalization of the nanoparticle surface is critical to the application. For Au NPs, thiol chemistry has been widely employed for its ease of use. However, thiol chemicals suffer from a few disadvantages such as oxidization and diffusion on the surface. We have previously reported the use of dithiocarbamate (DTC)-grafted PAH to modify Au NS surfaces and found that such particles exhibit considerable colloidal stability and can be further functionalized with biotin for biological sensing. There have only been a few reports discussing DTC surface functionalization on Ag NPs (Guerrini, et al. 2009; Tong, et al. 2006). Although Ag NPs are not as chemically stable as Au NPs, they show larger plasmonic enhancement and are superior for many applications. Therefore, it is also interesting to study the influence of surface functionalization on Ag NPs. For this reason, we applied PAH-DTC to Ag nanocubes and bipyramids.

The second part of this chapter treats surface functionalization of Au NRs using ionic self-assembly technique, where negatively-charged PSS polymer is attached to the outer CTAB layer of the NRs. The surface charge of the NRs can then be easily manipulated to be either positive or negative, facilitating applications to different scenarios (Gole and Murphy 2005). In one example, the PSS-coated Au NRs served as building blocks to fabricate plasmonic supra-structure via selective-activation of molecules on the particle surface. We also studied the adsorption rate of PSS-coated NRs onto planar surface and fiber tapers, which is beneficial to the understanding of the attachment of nanoparticles or bulky biological agents to surfaces of various curvatures and to the development of novel fiber sensors.

3.2 Dithiocarbamate (DTC)-grafted PAH on Ag NCs and BPs

PAH-DTC preparation

PAH-DTC (Chen and Robinson 2011) is prepared by grafting carbon disulfide (CS_2, Sigma, C573-500) onto PAH (M_w ~15,000, $(C_3H_8ClN)_n$, Sigma, 283215). PAH is a weak cationic polymer, which means its net charge depends on the pH value of the solution. When dissolved in DI water at 100 mM, the PAH solution showed a pH of about 4.0. The pH was then raised to 8.8 by adding NaOH, which is the pK_a value of PAH. The K_a in Henderson–Hasselbalch equation

$$\mathrm{pH} = \mathrm{p}K_a + \log\left(\frac{[\mathrm{A}^-]}{[\mathrm{HA}]}\right) \tag{3.1}$$

is the acid dissociation constant. We can see that when pH = pK_a, [HA] = $[\mathrm{A}^-]$, i.e., half of the amine groups on PAH are uncharged. The deprotonated amine groups can then react with CS_2 (Zhu, et al. 2008) yielding dithiocarbamate (DTC) moieties across the polymer chain. We denote this product PAH-DTC. PAH-DTC can bind covalently to Au surfaces via DTC-Au bonding while giving a positive surface charge when the remaining amines are protonated, preventing aggregations among the Au NPs.

The standard steps for preparation PAH-DTC are shown in **Fig. 3.1**: 1 mL of 100 mM PAH on a monomer basis at pH 8.8 was injected into a 4-mL vial, then degassed with argon for 5 mins and mixed with one-tenth equivalent CS_2, corresponding to 10 µL of 1 M CS_2 in ethanol. The mixture was then agitated with a vortex mixer for 30 s. The solution was incubated for 4 h before use. Successful preparation of PAH-DTC can be confirmed by UV-Vis absorption spectroscopy. **Fig. 3.2** shows the spectrum of 1 mM PAH-DTC in a 1-cm cuvette after 4 h reaction. The observation of two characteristic peaks of dithiocarbamate at 254 and 286 nm confirmed that PAH-DTC was formed in the solution. Generally, PAH-DTC in this form is stable for several days when protected from air.

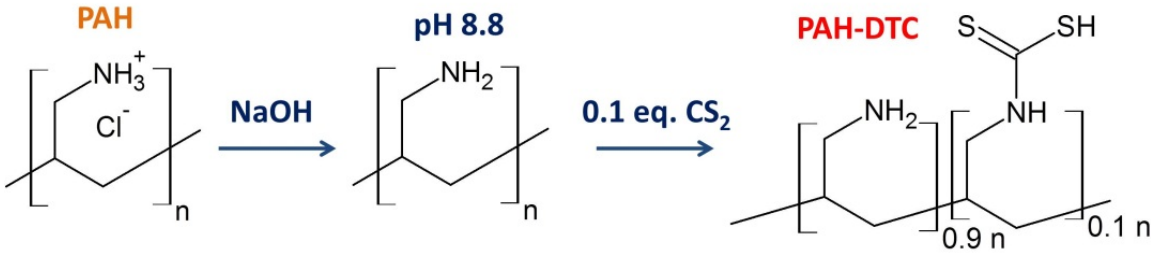

Fig. 3.1: Scheme of synthesis of PAH-DTC.

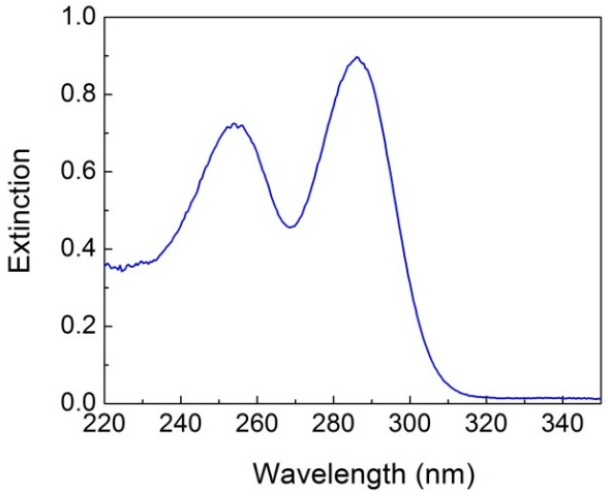

Fig. 3.2: Extinction spectrum of 1 mM PAH-DTC. The characteristic peaks at 254 and 286 nm indicate the presence of DTC.

PAH and PAH-DTC coating

The as-prepared Ag NC suspension (Sec. 2.3) was diluted 20 times with DI water. Twenty 4-mL vials were filled with 0.5 mL of the suspension. To these vials, 0.5 mL of PAH or PAH-DTC with concentrations varying from 10 μM to 1280 μM were then added while stirring, so the final concentrations of PAH or PAH-DTC in the mixtures were between 5 and 640 μM. After 30 mins, excess polymer was removed by centrifugation using polypropylene centrifuge tubes (Fisher, 02-681-320) at 5000 rcf for 10 mins followed by redispersion to the same volume of DI water.

The extinction spectra were taken using a Perkin–Elmer Lambda 25 UV-visible spectrophotometer and zeta potentials were measured using a Zetasizer (Malvern, Nano-ZS).

Zeta potential measurement

On a particle surface, there are two layers of charges—the inner (Stern) layer where ions are strongly bound, and the outer layer where the ions are loosely bound. There exists a boundary at the edge of the outer layer, inside which the ions move with the particle. Zeta potential (ζ-potential) is the potential at this boundary with respect to the dispersion medium. The Zetasizer applies an alternating electric field on the electrodes of a disposable capillary cell (Malvern, DTS1061) while a laser beam passes through the sample. By studying the scattering beam using Laser Doppler Velocimetry, the electrophoretic mobility of the particle can be obtained, from which the ζ-potential can be determined. A colloid with an average ζ-potential larger than ±25 mV can be considered colloidally stable. For 10 to 100 nm particles at a concentration between 0.1 mg/mL and 5 mg/mL, the concentration of the particles does not affect the ζ-potential.

Fig. 3.3 shows an example of the ζ-potential distribution measured by the Zetasizer. As-prepared Ag NC suspension shows an average potential of −32.8 mV. This is probably because of the stabilizing agent PVP that was used during the NC synthesis. The PVP on the Ag NC surfaces has been oxidized during the heating process. Therefore, the as-prepared Ag NCs are negatively charged. PAH-DTC coated Ag NC suspension has a ζ-potential of +28.6 mV because of the charged amine groups in PAH. The sign change suggests that the coating was successful.

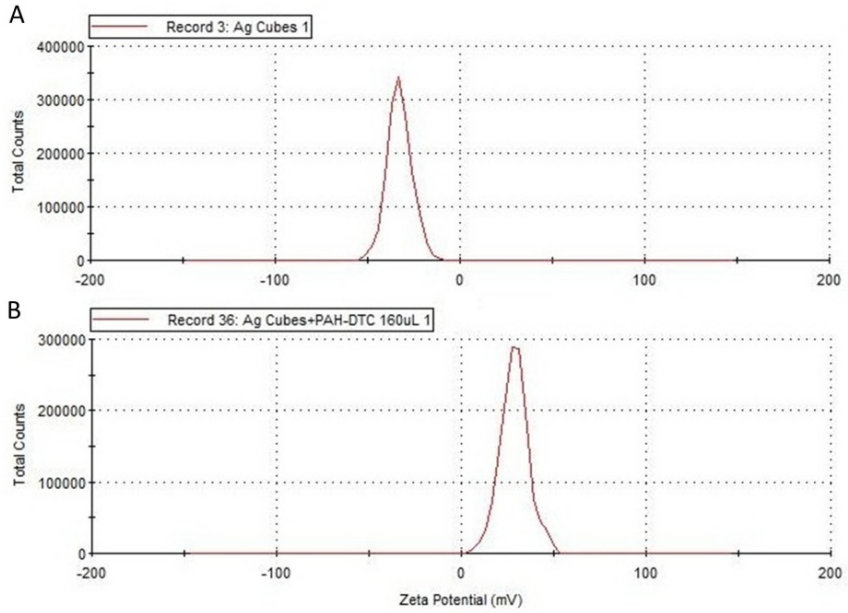

Fig. 3.3: Examples of ζ-potential distribution. A) As-prepared Ag cube suspension; B) after successful PAH-DTC coating. The suspensions were diluted 30× from their initial concentration.

Results and discussion

PAH polymers bind to the surface of Ag NCs because of electrostatic attraction between the positively charged PAH and the negatively charged PVP. **Fig. 3.4A** shows the extinction spectra of the original Ag NC suspension. After PAH coating, the spectrum stayed almost unchanged except that the overall intensity of the spectrum dropped due to the loss of particles from the suspension. In other words, the spectral positions and widths of the original 356, 393, 496 and the 630 nm broad peaks did not change in the experiments. In general, we would expect the resonance peaks red-shift a few nanometers after coating due to the refractive index increase from water to polymer. This did not occur in this case, and we speculate that the PVP monolayer may be thicker than the decay length of the plasmon mode and thus PAH coating barely affects the spectra. **Fig. 3.4B** shows the extinction spectra of the NC suspensions after PAH-DTC coating. In this case, DTC-grafted PAH are chemically adsorbed onto Ag NC surfaces via the

DTC-Ag bonds. Compared to the NCs with the physisorbed PAH, the overall shape of the spectrum has changed dramatically.

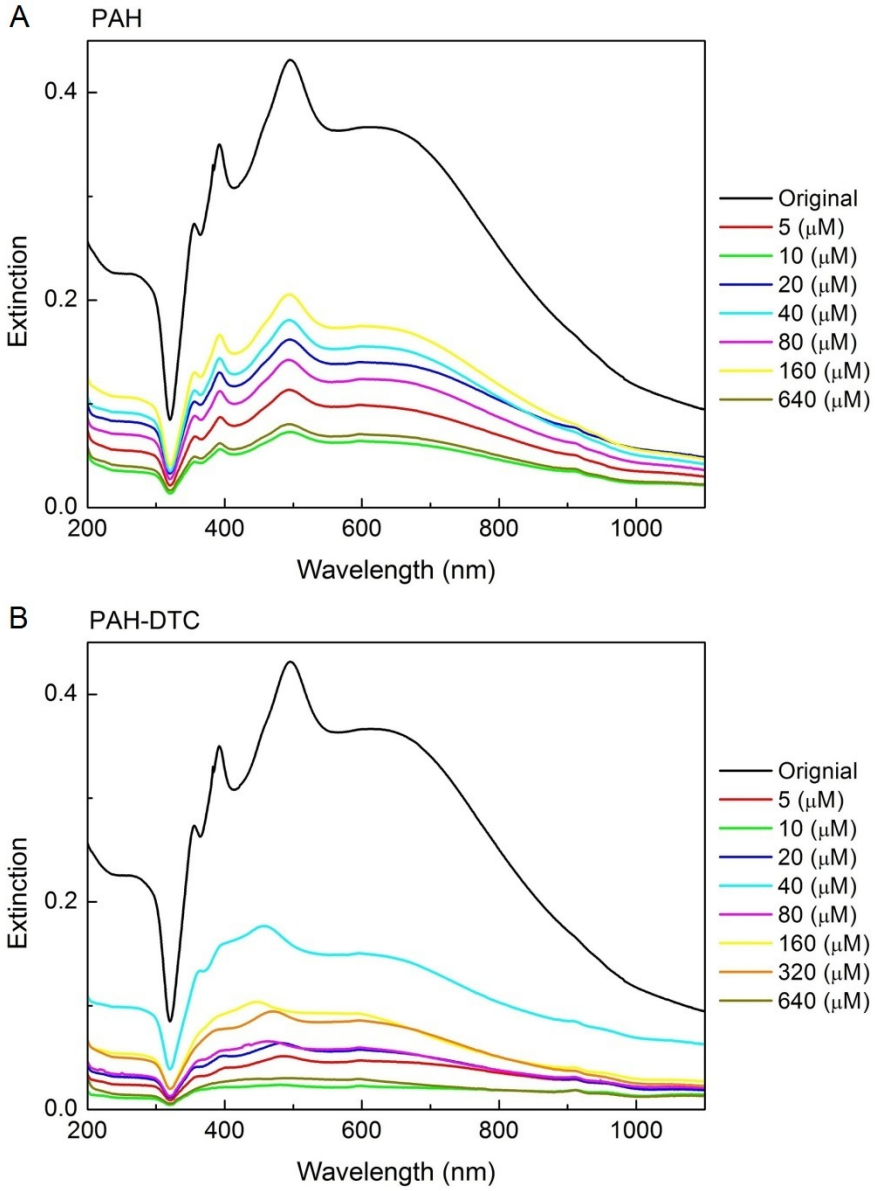

Fig. 3.4: Extinction spectra of Ag NC suspensions functionalized with different final A) PAH; B) PAH-DTC concentrations.

In order to know whether the coating is successful, we need to check the ζ-potential of the Ag NC suspensions after cleaning out the excess PAH/PAH-DTC. Surprisingly, the ζ-potential

in **Fig. 3.5A** fluctuates above and below zero as the polymer concentration changes. The ζ-potential measurement should be positive if the coating was successful, so we conclude that the coating was not successful for every concentration of PAH or PAH-DTC. This was unexpected considering our previous study on Au NSs. It is interesting to note that the ζ-potential of Ag NC suspension seemed to behave the same way when the same amount of PAH and PAH-DTC were added, which remains a puzzle to us. It is possible that there exist certain concentration values of the polymers that result in a perfect surface coverage of the particles with little excess polymers.

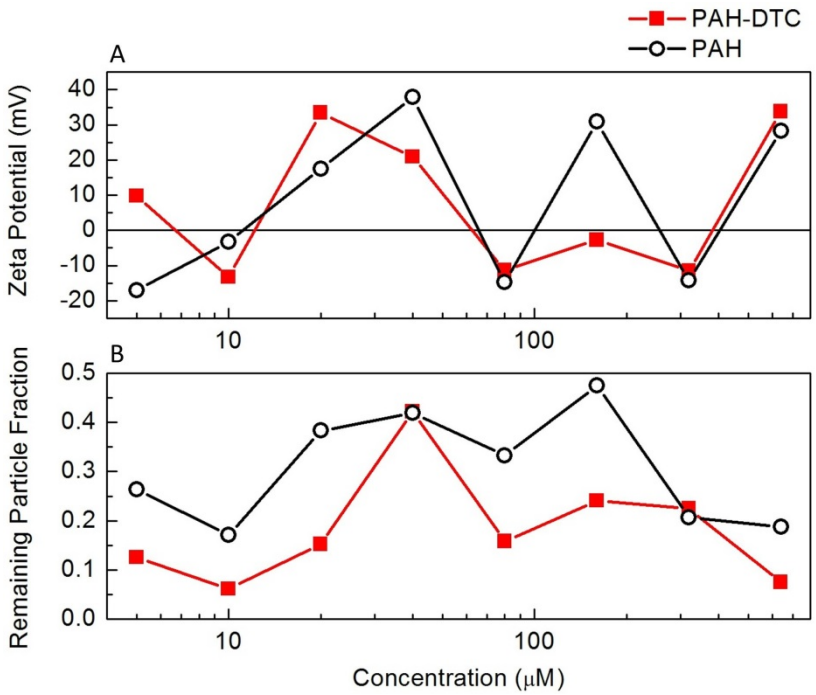

Fig. 3.5: ζ-potential measurements and remaining particle fractions with different final concentrations of PAH/PAH-DTC during coating.

By integrating the area under the extinction line and comparing to the original NC solution, the remaining fraction can be obtained. This is done according to Beer–Lambert law, $T = 10^{-\varepsilon l c}$, where T is the transmission; ε is the extinction coefficient; l is the path length and c is the molar concentration of absorbing particles. Extinction (the combination of absorbance and scattering) is defined as $E = -\log T$. If we assume that the size and shape of the NCs do not change, the extinction value is proportional to the particle concentration. (In reality, we figured the edge

lengths of the cubes were smaller depending on the added amount of polymer solution, but this has little effect on our analysis.) **Fig. 3.5B** shows the fractions of particles remaining in suspension after PAH/PAH-DTC coating at different polymer concentrations. Both PAH and PAH-DTC coating resulted in the loss of more than half of the NCs. (For Au NSs, by contrast, less than 5 % of loss was observed.) Some of the particle loss happened during the cleaning step, when the particles stuck to the surface of the polypropylene centrifuge tube (Fisher, 02-681-320) after centrifugation and could not be redispersed in the solution even with ultrasonication. Some of the loss happened at the instant when the polymer solution was added as the color of the NC solution changed from milky white to slightly transparent. When the final concentration of the polymer solution was above 640 μM, the solution instantly became fully transparent.

Combing the ζ-potential and remaining particle fraction data, we reached the conclusion that the best condition for coating the 20× diluted NCs is to add 0.5 mL of 40–80 μM PAH/PAH-DTC into 0.5 mL NC suspension making the final concentration 20–40 μM. We then estimated the minimum polymer concentration that would theoretically be required to fully coat all the NCs in our 20× diluted NC suspension. A single monolayer coverage of polymer corresponds to approximately 1 mg/m^2 (Auguste, et al. 2008). Therefore, in order to estimate the total surface area of the Ag NCs in suspension, we need to know both particle size and the absolute Ag concentration. The inductively coupled plasma atomic emission spectrometer (ICP-AES) located in the VT Soil Department (Arcos SOP, Spectro Analytical Instruments, Inc.) gave us a Ag concentration of 958 ppm for the as-prepared Ag NC suspension. The average edge length of the cubes was 126 nm as determined from the SEM images. This means the concentration of the 20× diluted Ag cubes was 2.28×10^9 $particles/cm^{-3}$. Adding the polymer solution halves the concentration, so the surface area per volume becomes 109 m^2/m^3. As the monomer formula weight of PAH is 93, we find that the minimum final concentration of PAH/PAH-DTC for monolayer coverage in our experiment is 1.17 μM, which means that optimum results were obtained for a polymer excess of 20 to 40 times.

Since positive ζ-potential indicates successful polymer coating, we went back to the spectra in **Fig. 3.4B** and extracted those with positive ζ-potential. The normalized spectra are shown in

Fig. 3.6, which shows a clear trend that the peak resonances blueshift with increasing PAH-DTC concentration. When the final concentration of PAH-DTC changed from 5 to 160 μM, the resonance peak initially at 496 nm shifted to 446 nm. The inset shows the relation between the spectral peak position and the PAH-DTC concentration. According to Xia *et al.*'s DDA simulation (Zhou, et al. 2008), the blueshift of the peak wavelength indicates that the Ag NCs have become smaller. They showed that the peak wavelength of Ag NC in air blueshifts ~10 nm when the edge length of Ag NC changes from 130 to 120 nm. Unfortunately, SEM imaging of these samples were not performed. Otherwise, with 50 nm blueshift, the size change of our NCs would likely have been observed.

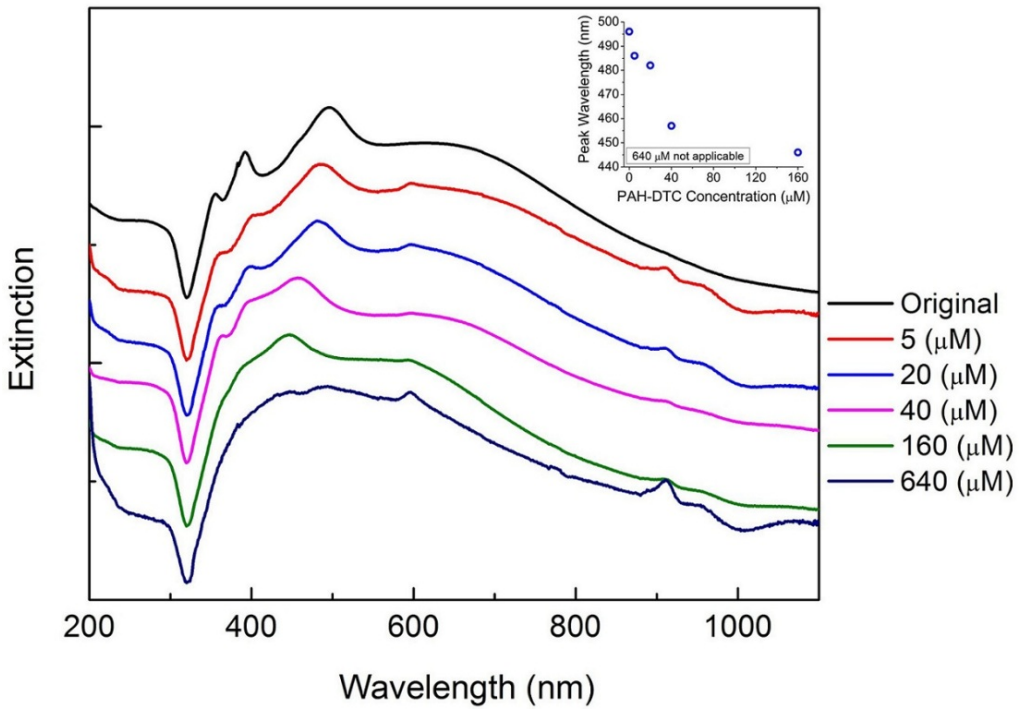

Fig. 3.6: Normalized extinction spectra of the successful PAH-DTC coated Ag cube suspensions. The inset is the peak wavelengths of cube suspensions and their corresponding final concentrations of PAH/PAH-DTC during coating.

The SEM images in **Fig. 3.7** shows the SEM images of samples obtained under different experimental conditions as summarized in **Tab. 3.1**. The average edge lengths of the cubes shown in **Fig. 3.7A**, **B** and **C** exhibit large uncertainties, so it is difficult to draw conclusions on

whether the cubes shrank or not. However, for the extreme case of sample D, the final concentration of PAH-DTC was so high that the Ag cubes were almost completely dissolved. As a result, this sample did not go through the cleaning step, but was directly dropcasted onto a silicon wafer and dried in air for SEM imaging.

Tab. 3.1: Experimental conditions and the average edge lengths of the Ag NCs.

	Ag NC Solution	PAH-DTC	Final C (µM)	Average Edge Length (nm)
A	Original	0	0	127 ±8
B	9 mL 21× diluted	1 mM, 1 mL	100	124 ±6
C	0.5 mL 30× diluted	1 mM, 0.16 mL	242	122 ±7
D	1 mL 80× diluted	100 mM, 0.2 mL	16666	41 ±10

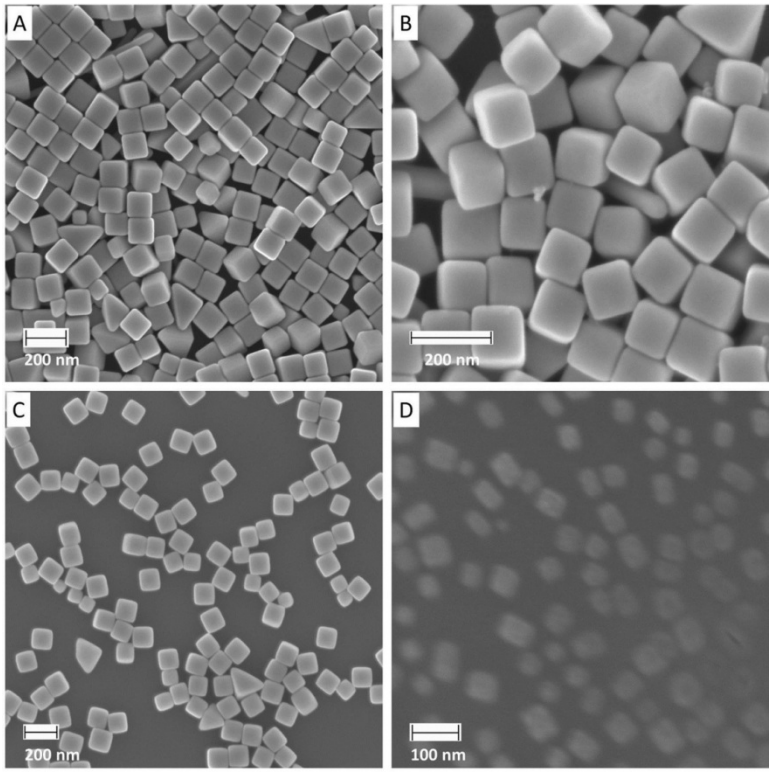

Fig. 3.7: SEM images of Ag NCs with different coating conditions described in **Tab. 3.1**.

We note that much less than 16.7 mM of PAH-DTC was required to make the NC suspensions transparent. As we can see in **Fig. 3.4B**, 640 µM of PAH-DTC already made the remaining fraction very low, and at a concentration of 1280 µM, the cube solution became nearly

transparent. The loss of particles here is then not mainly due to dissolution, but most likely the result of particle aggregation or adhesion to glassware or polypropylene centrifuge tubes.

We also performed a similar experiment on Ag BPs. The surface of Ag BP is coated with BSPP, rather than PVP, so it is reasonable to expect that the results would be different. We added 0.1 mL of 100 mM PAH-DTC to 0.5 mL of the 1× Ag BP suspension. The final concentration of PAH-DTC during coating was 16.7 mM. With such a high concentration, Ag NCs would aggregate immediately. However, the Ag BPs remained stable in this case. The ζ-potential changed from −18.5 to +22.2 mV indicated the coating was successful. **Fig. 3.8** shows the spectra of Ag BP suspension before and after PAH-DTC coating. PAH-DTC coating only caused mild particle loss and we believe this occurred during the cleaning step.

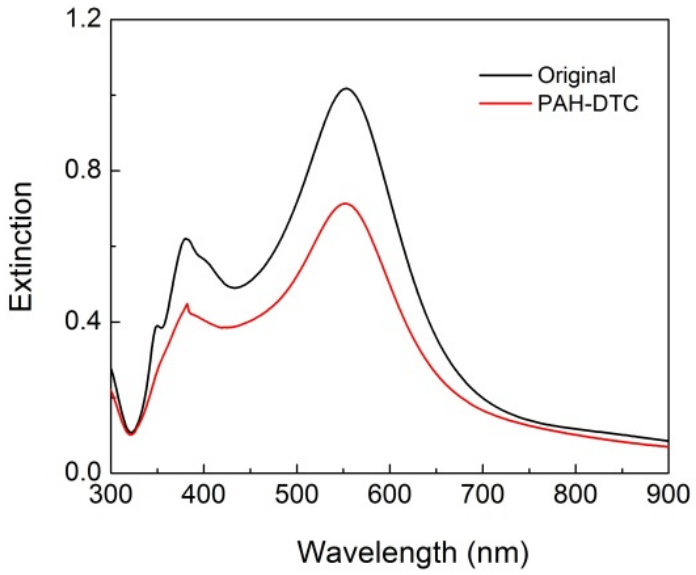

Fig. 3.8: Extinction spectra of as-synthesized Ag BPs in suspension and after the coating with PAH-DTC.

The peak resonances of the Ag BP suspension remained distinct after coating, while the 350 nm peak lost intensity. We speculate that the different results seen in NCs and BPs are due either to the different crystal facets of their surface or to the difference in surface functionalization.

3.3 PSS on Au NRs and BPs

PSS coating

Poly(sodium 4-styrenesulfonate) (PSS, $(C_8H_7NaO_3S)n$, M_w ~70,000, Sigma, 243051) is a strong polyelectrolyte because its negative charge does not vary with pH. **Fig. 3.9A** shows the molecular structure of PSS. By simple electrostatic attraction, PSS can be coated onto the surface of positively charged NPs, such as CTAB-stabilized Au NSs, NRs, and BPs. CTAB is a cationic surfactant that was discussed in the synthesis sections in 2.5, 2.6 and 2.7. Its molecular structure can be found in **Fig. 2.18**. In the following, we will use Au NRs as our example, but the same technique can be applied to CTAB coated spheres and bipyramids.

CTAB forms a double layer on Au NRs surface making them positively charged (Murphy, et al. 2005). Before coating with PSS, the excess CTAB needs to be removed from the solution as described in Sec. 2.6. As a reminder, the Au NR suspension was centrifuged at 2500 rcf for 10 mins and the supernatant was then replaced by the same amount of DI water. The precipitant was then resuspended by 30 s ultrasonication. The sonication should not run for longer than 1 min otherwise the NRs solution can overheat, which may result in aggregation. Following our previous work on Au NS assembly (Chen and Robinson 2011), PSS polymer solution (1 mg/mL, ~5 mM) was added to the cleaned suspension at a volume ratio of 1 to 10 with stirring. (1 mL of PSS solution was added into 10 mL Au NR solution.) After 30 mins, the NRs were cleaned by the same centrifugation procedure to remove the excess PSS for two times. The coating process was monitored by ζ-potential and UV-VIS measurements.

The ζ-potential distribution of the cleaned Au NRs in **Fig. 3.9C** shows an average at +32.3 mV before coating. However, part of the counts cross the zero line and this happened with all the batches of the Au NR solution that we synthesized. After PSS coating, the average ζ-potential falls in the range between −60 and −90 mV, with an average of −62.2 mV. With the full distribution corresponding to highly negative ζ-potential values, the PSS-coated NRs are very stable and can survive for at least six months. **B** is the extinction spectra of the Au NRs in suspension before and after coating. The LSPR shifted from 816 to 820 nm due to the higher

effective dielectric constant seen by the plasmon modes when the PSS is adsorbed on the surface. The resonance peak intensity stays almost the same suggesting that most of the NRs survived the coating process.

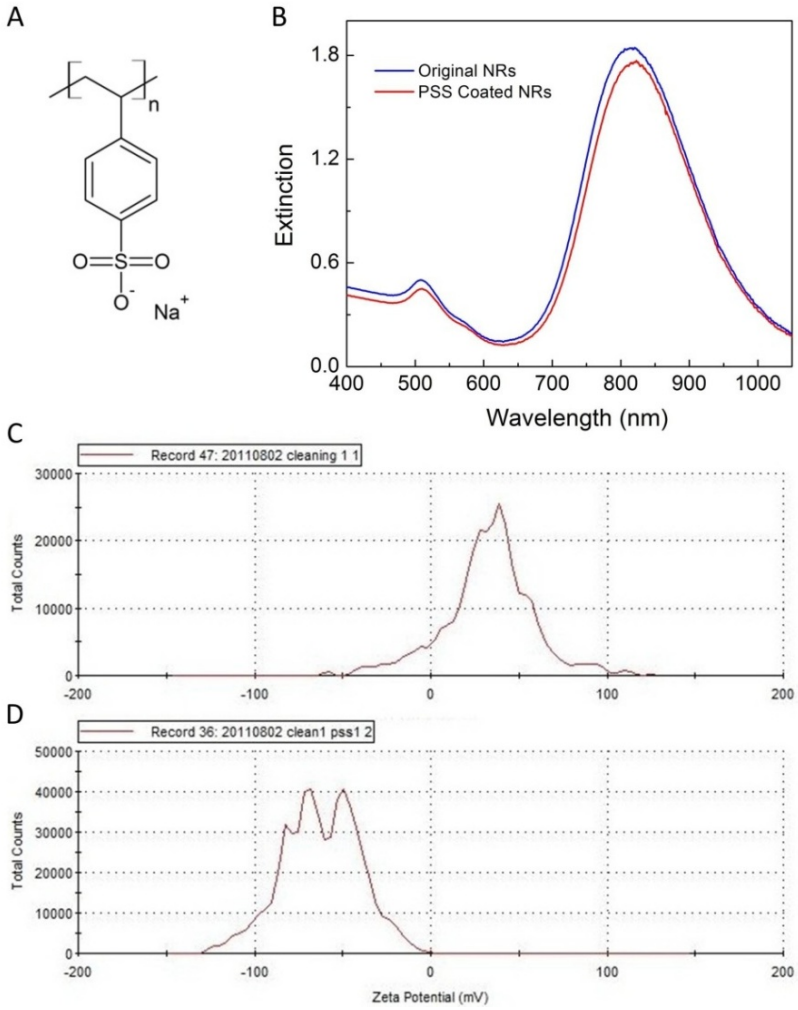

Fig. 3.9: A) Molecular structure of poly(sodium 4-styrenesulfonate) (PSS). B) Extinction spectra of Au NR suspension before and after PSS coating. ζ-potential distributions of Au NRs C) before; D) after PSS coating.

Application 1—Au NRs adsorbing onto PAH-coated substrate

The PSS-coated Au NRs can easily adsorb onto a PAH-coated substrate, whether it is a plane, a cylinder (like a fiber) or other shapes. PAH is same cationic polymer as described in Sec.

3.2 with the same molecular weight, M_w ~15,000. Before coating the substrate, the 10 mM PAH solution was adjusted from pH 4.5 to 7.0 by adding NaOH, which was to make PAH less charged so that the PSS-coated NRs can evenly spread out across the surface. First, an aqua regia-cleaned (or RCA-cleaned) glass coverslip was immersed into the PAH solution for 10 mins and followed by DI water rinsing and drying with a stream of nitrogen gas. The positively charged coverslip was then immersed in a diluted PSS-coated Au NR suspension. The concentration was 3 % of its initial concentration. After the desired deposition time, the coverslip was then rinsed with DI water and dried with nitrogen.

The particle concentration of the Au NR suspension was obtained by inductively coupled plasma atomic emission spectroscopy (ICP-AES) and SEM. The Au concentration was found to be 52.0 ppm. After estimating the NR size to 17 nm in diameter and 70 nm in length from SEM micrograph, the particle concentration in suspension was found to be 1.70×10^{11} particles/mL. This concentration was too high for the deposition experiments.

Fig. 3.10 shows the PAH-coated coverslip after 4 h immersion. After 4 h, the adsorption had almost saturated as the repulsion between Au NRs strongly suppressed additional adsorption. The average density was 27 NRs/μm^2 in this sample. The particle density can be adjusted by changing the NR concentration and the soaking time. If several coverslips were placed in a Coplin staining jar and each of them was taken out and rinsed in a timely manner, the adsorbing trend can be observed as in **Fig. 3.11**. In this figure, each image was cropped (6 μm × 6 μm) from the same corner of the original SEM images. And the graph is the statistics from 5 different locations of each sample. The adsorption rate gradually slowed down as expected, with the particle density behaving as $\sqrt{t}$ (Park, et al. 1987).

One might ask why coating the rods with PSS is necessary, as it may seem that positively charged CTAB-coated rods should easily adsorb onto negatively charged surfaces. The problem is that the surface-bound CTAB is a small molecule and exists in a thermodynamically balance with free CTAB dissolved in the suspension. Without the free CTAB, the CTAB on the NR surfaces would rapidly come off the surfaces to achieve the equilibrium, causing the rods to aggregate due to the lack of a charged surface layer. The free CTAB does however bind to any

negatively charged substrate that is present and thus reverses its charge so that NRs do not adsorb on the substrate. By contrast, PSS is a long-chain polymer and strongly attaches to the NR surface with far less detachment so that no PSS is required in the suspension. Therefore, PSS-coated NRs can uniformly distribute on a PAH-coated substrate.

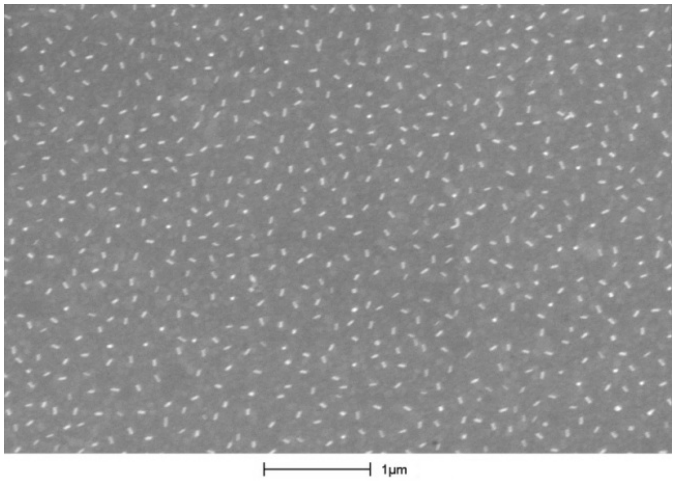

Fig. 3.10: SEM image of PSS-coated Au NRs on a PAH-coated coverslip. The coverslip was immersed in 3 % Au NR suspension for 4 h.

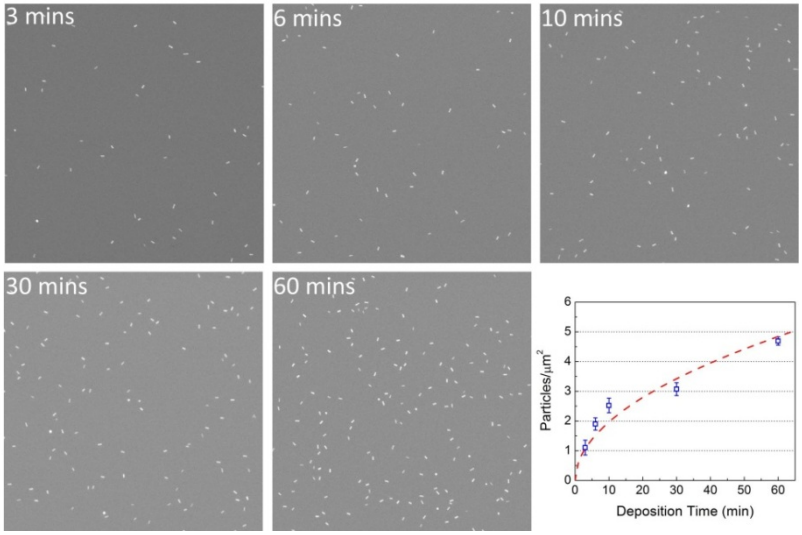

Fig. 3.11: SEM images of Au NRs with different adsorbing time. The SEM images are of 6 μm × 6 μm areas and are taken from the micrographs together with other micrographs to generate the statistic graph. The fitting is $\text{Particle}/\mu\text{m}^2 = 0.625\sqrt{\text{t}}$.

Application 2—Au NRs adsorbing onto a silica fiber as a sensor

This work was done in collaboration with Jihaeng Yi (Xu Group, ECE, VT). For a typical optical fiber taper, the diameter of the tapered region is much smaller than that of a normal fiber and thus the guided mode field is extended beyond the fiber core. A micrograph of the taper profile can be seen in **Fig. 3.12**. When used as a sensor, any refractive index changes, such as binding of biological molecules to the taper, will affect the guided mode and lead to a change in the transmitted light intensity. By monitoring this intensity change, sensing of biological events is possible. To enhance the sensing performance, we combined optical tapers with plasmonic nanoparticles by adsorbing NPs onto the taper surface. The ratio between the extinction and physical cross-sections of plasmonic nanoparticles are much larger than 1 (Ming, et al. 2011). Because of this, properly functionalized Au NPs attached to a fiber surface can generate much stronger signals than the fiber itself would be capable of. In contrast to Shao *et al.*'s etching the fiber (Shao, et al. 2010), we use a stretched fiber optic taper in our work. The taper was prepared by heating a silica fiber with a propane-oxygen flame while holding the fiber by two fiber clamps. As the glass softens under high temperature, the clamps are pulled apart, and the time-dependence of the pulling force enables us to control the spatial profile of the taper diameter (Xue, et al. 2007).

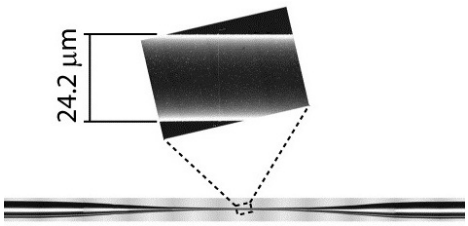

Fig. 3.12: An example micrograph of a fiber taper.

In our experiment, we monitored the transmitted light loss spectra of an optical taper, which is exposed to properly functionalized Au NRs solution. The fiber optic taper was fixed on a U-shape glass slide using epoxy after pulling. One end of the taper connected to a halogen light source (Ocean Optics, DH-2000) and the other to a high-resolution miniature fiber optic spectrometer (Ocean Optics, HR2000). The taper was then submerged into a 10 mM PAH

solution for 3 mins and subsequently a DI water bath for 3 mins to remove excess PAH. At this moment, a reference spectrum (I_0) was taken. The taper was then placed into a clean dish followed by pouring in the 3 % (~5.1×10^9 particles/mL) PSS-coated Au NR suspension. As the NRs kept adsorbing onto the taper, more and more light was coupled out of the taper and the spectrum of the transmitted light (I) was monitored in real time as less and less light made it through the fiber.

Fig. 3.13 shows the time-resolved loss spectrum of the taper. The dB loss is defined by $\text{dB Loss} = 10 \log (I/I_0)$. The waist diameter of this specific taper is 7 µm. At the instant of adding NR solution, the signal started dropping. The inset on the right plots the transmitted light intensity over time showing that after one hour more than 80 % of the inserted light was coupled out of the taper by the Au NRs. The kinks superposed on the intensity line were due to vibrations in the setup changing the rate of NR adsorption onto the fiber. At the end of the deposition, the NR coverage was about 25−50 NRs/µm^2 in the center of taper region and decreased when moving away from the center. This is because the diameter of the taper increases when moving further away from the waist region. More details can be found in the next chapter where we analyze the particle adsorption in detail. In that chapter, we used spheres instead of rods and ensured that the deposition was performed under condition of zero liquid flow around the fiber.

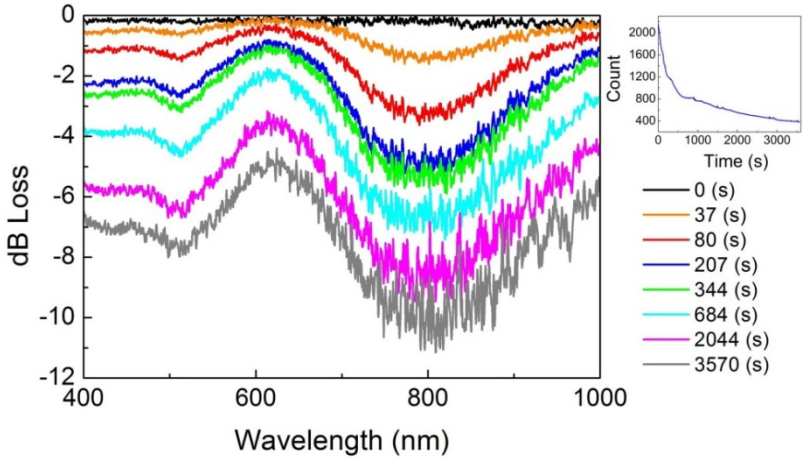

Fig. 3.13: Time-resolved loss spectrum of a fiber optic taper as more NPs are gradually adsorbed onto the fiber.

Fig. 3.14 shows the extinction spectra of PSS-coated NRs in suspension, on a coverslip and on a fiber taper. The first two spectra were taken by Perkin–Elmer Lambda 25 UV-visible spectrophotometer. The coverslip sample was placed in a cuvette filled with water when the spectrum was taken. The spectrum on the fiber taper was extracted from **Fig. 3.13** at 207 s. The spectra have been rescaled for a better comparison. The spectrum of the NRs on the coverslip red-shifted a few nanometers because part of the surrounding medium has changed from water to glass. The spectrum of NRs on the taper is very close to that on the coverslip, which confirms that the loss in **Fig. 3.13** is indeed due to adsorption of Au NRs on the taper surface.

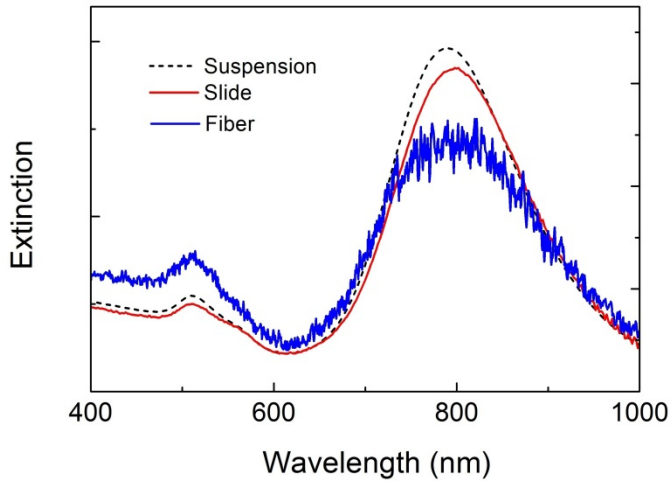

Fig. 3.14: Extinction spectra of PSS-coated NRs in suspension, on a coverslip in water, and on a fiber optic taper in water.

3.4 Conclusion

We have studied the effect of PAH-DTC coating on Ag nanocubes and bipyramids. Unlike the case of Au nanospheres, the PAH-DTC coating can negatively affect the Ag nanoparticles. PAH-DTC can shrink the Ag NC size as indicated by a blueshift of the resonance peaks that increases with PAH-DTC concentration. We also found that successful PAH-DTC coating happens only within a certain concentration range, outside of which the particles rapidly aggregate. However, for the case of Ag BPs, the PAH-DTC only causes mild loss. More

experiments and studies are needed to clarify this discrepancy. Nevertheless, we have shown that the PAH-DTC coating can be applied to Ag BPs to achieve amine surface functionalization.

We demonstrated applications of PSS-coated NRs: adsorption onto planar (glass slide) and curved (fiber taper) PAH-coated substrates. We have demonstrated that very uniform coverages of PSS-coated NRs on planar substrate can be achieved. By monitoring the loss spectrum of a fiber taper onto which NRs are being adsorbed, adsorption rate of the PSS-coated NRs was monitored. This can serves as a model for biological sensing with plasmonic nanocrystals. Functionalization of Au NRs with PSS can be performed with nearly 100 % yields. The resulting particles are easy to handle and show good long-term stability.

Chapter 4 Irreversible Adsorption of Gold Nanospheres on Fiber Optical Tapers and Microspheres

This work was done in collaboration with Jihaeng Yi, Ishac Kandas and Bo Liu (Xu Group, ECE, VT). We study the adsorption of gold nanospheres (Au NSs) onto planar, cylindrical and spherical glass surfaces from quiescent particle suspensions. The surfaces consist of tapers and microspheres fabricated from optical fibers and were coated with the polycation PAH, enabling irreversible nanosphere adsorption. Our results fit well with theory, which predicts that particle adsorption rates depend strongly on surface geometry, and can exceed the planar surface deposition rate by over two orders of magnitude when the particle diffusion length is large compared to the surface curvature. This is particularly important for plasmonic sensors and other devices fabricated by depositing nanoparticles (NPs) from suspensions onto surfaces with non-trivial geometries. We find that at short deposition times, the nanoparticle adsorption is largely independent of substrate geometry, while at long times, deposition is significantly faster onto the curved surfaces. The crossover occurs when the NP diffusion length in comparable to the radius of curvature of the surface.

4.1 Introduction

Sensors and other devices based on plasmon resonances in metal NPs have attracted a large amount of attention in recent years (Zeng, et al. 2011 and the references therein). In many implementations, particles are deposited from a liquid suspension onto a substrate to form a plasmonically active surface (Nusz, et al. 2009; Zhao, et al. 2006). Such substrate is often flat, but other geometries are also of interest. In particular, since plasmonic devices are intrinsically optical, it is natural to consider NP deposition on optical microstructures such as silica fibers, fiber tapers or microsphere resonators, which display, respectively, cylindrical, conical and

spherical geometries. As the complexity of such devices increases, it is imperative to develop a good understanding of the process of NP deposition. Here, we focus on the dependence of deposition on substrate geometry as it applies to silica-based tapers and microspheres.

The problem of particle adsorption on a collecting surface is of great technological importance in fields such as materials science, food and pharmaceutical fabrication, electrophoresis, catalysis, etc. It is also of interest in biomedicine in describing processes such as ligand binding to macromolecules or digestion by microbes and cells (Shoup and Szabo 1982; Wagner, et al. 2006). It is then not surprising that the problem has been studied for a long time and that theoretical treatments have reached a high degree of sophistication (Adamczyk 2006; Evans 1993; Talbot, et al. 2000). However, the bulk of the experimental work in this field has been done on planar surfaces, and studies of adsorption onto curved collecting surfaces (Gu and Li 2002; Harding 1995; Shoup and Szabo 1982) have generally concerned regimes that are not directly applicable to optical and plasmonic device fabrication.

4.2 Theory

For our theoretical treatment, we confine ourselves to the simplest possible case, where we first assume that the collecting surfaces are perfect sinks, i.e. that any particle that gets within a certain small distance from a surface sticks immediately and irreversibly, which is reasonable for small particles at low concentrations (Adamczyk 2000; Adamczyk and Szyk 2000), and at time scales where the fast adhesion kinetics is masked by the slower diffusion dominated particle transport to the surface. Since the Debye length in water is at the most a few tens of nanometers, this holds for all times longer than about a millisecond. We also assume that the drag experienced by a particle near a surface is balanced by attractive dispersion forces (the Smoluchowski-Levich approximation), so that we can take the diffusion coefficient to be constant everywhere including near the surface. Finally, we treat only the case where there are no external forces and no liquid flow present (quiescent conditions). Under these idealized conditions, the problem reduces to solving the diffusion equation:

$$\begin{cases} \partial_t n(\mathbf{r},t) = D\nabla^2 n(\mathbf{r},t) \\ n(\mathbf{r},0) = n_0 \\ n(\mathbf{r}_s,t) = 0, n(\infty,t) = n_0 \end{cases} \tag{4.1}$$

Here, $n(\mathbf{r},t)$ is the concentration of nanoparticles in the suspension, D is the diffusion constant, n_0 is the initial concentration of particles, and $\{\mathbf{r}_s\}$ are the coordinates of the collecting surface. In all geometries at issue here, this can be solved with standard separation of variables techniques. The accumulation density of particles on the collecting surface is given by $\langle N(t)\rangle = D\int_0^t \partial_\perp n(\mathbf{r}_s,t')dt'$, where $\partial_\perp$ is the derivative normal to the surface. From this we obtain:

$$\begin{aligned} \langle N_{\text{flat}}(t)\rangle &= 2n_0\sqrt{\frac{Dt}{\pi}} \\ \langle N_{\text{sph}}(t)\rangle &= n_0\left(2\sqrt{\frac{Dt}{\pi}} + \frac{Dt}{a}\right) \\ \langle N_{\text{cyl}}(t)\rangle &= \frac{2n_0 a}{\pi}\int_0^{\frac{Dt}{a^2}} d\tau \int_0^\infty d\beta e^{-\tau\beta^2}\Im\left\{\frac{H_1^{(2)}(\beta)}{H_0^{(2)}(\beta)}\right\} \end{aligned} \tag{4.2}$$

where the three subscripts for $\langle N(t)\rangle$ indicates the corresponding adsorbed particle density for planar, spherical and cylindrical surfaces, respectively. D and a are the diffusion constant and the substrate radius of curvature, respectively. $H_\nu^{(2)}(x)$ are Hankel functions of the second kind, and $\Im(z)$ denotes the imaginary part of z. The formula for $\langle N_{\text{flat}}(t)\rangle$ is well-known and has repeatedly been shown to describe irreversible particle deposition onto flat adhesive surfaces quite well (Adamczyk, et al. 2004; Grabar, et al. 1996; Park, et al. 1987), so long as the surface particle density is low enough that the assumption of a perfectly adhesive surface remains valid. To simplify matters, we introduce dimensionless measures of time $\tau = Dt/a^2$ and particle accumulation $\langle \nu(\tau)\rangle = \langle N\rangle/n_0 a$, which gives us

$$\langle \nu_{\text{flat}}(\tau) \rangle = 2\sqrt{\frac{\tau}{\pi}}$$
$$\langle \nu_{\text{sph}}(\tau) \rangle = 2\sqrt{\frac{\tau}{\pi}} + \tau$$
$$\langle \nu_{\text{cyl}}(\tau) \rangle = \frac{2}{\pi}\int_0^{\tau} d\tau' \int_0^{\infty} d\beta e^{-\tau'\beta^2} \Im\left\{\frac{H_1^{(2)}(\beta)}{H_0^{(2)}(\beta)}\right\} \tag{4.3}$$
$$\approx \begin{cases} 2\sqrt{\frac{\tau}{\pi}} + \frac{\tau}{2} & \tau \leq 2 \\ \frac{2}{\pi}\left[\tau \text{arccot}\left(\frac{\ln \gamma\tau}{\pi}\right) + 1\right] & \tau > 2 \end{cases}$$

$\gamma = 0.5772$ is a constant chosen to obtain the best fit with the exact expression. The errors in the approximations for $\langle \nu_{\text{cyl}}(\tau) \rangle$ are less than 2 % when $\tau < 0.4$ and $\tau > 2$. $\tau = 1$ corresponds to the time when the particle diffusion length $\sqrt{4Dt}$ equals the diameter of the cylinder or sphere $2a$. Therefore, for $\tau \ll 1$, the surface appears flat over the scale of the diffusion length, and consequently all surfaces behave as the planar case, where the particle adsorption process gradually depletes the particles from the suspension closest to the surface faster than they can be replaced from regions farther out, which reduces the deposition rate over time, so that $\langle \nu(\tau) \rangle \sim \sqrt{\tau}$ (Adamczyk, et al. 2004; Grabar, et al. 1996; Park, et al. 1987). When $\tau \gg 1$, the finite spherical surface is too small to appreciably deplete the particles from the bulk of the suspension, and the deposition rate is therefore constant, and hence $\langle \nu_{\text{sph}}(\tau) \rangle \sim \tau$. The cylindrical surface represents an intermediate case where the cylinder does deplete the suspensions of particles so that the deposition rate continually decreases, but only logarithmically in time, so that for very long times $\langle \nu_{\text{cyl}}(\tau) \rangle \sim \frac{\tau}{\ln \tau}$. As a result of this, particle deposition occurs significantly faster on curved surfaces than on flat ones, as long as the particle diffusion length is larger than the surface radius of curvature. Since this crossover occurs earlier for smaller radii, the rate of deposition is in fact faster for more highly curved surfaces.

It is also worth mentioning that although the curvature of the surface does affect the interaction between it and the suspended particles, this effect is only appreciable if the curvature becomes comparable to the particle radius (Bhattacharjee, et al. 1998). Moreover, as particle

transport is diffusion limited, this interaction only affects the probability of particle adsorption during a collision with the surface, which under the conditions used here is already nearly 100 %.

4.3 Experimental Section

To test our theory, we deposited Au NSs on three types of silica surfaces: the flat surface of microscope slides, the near-cylindrical surface of tapered optical fibers, and microspheres. The tapers were made with a procedure similar to those in the literature (Ward, et al. 2006; Xue, et al. 2007). Briefly, we placed a silica fiber between two fiber clamps and used a propane-oxygen flame to heat the fiber. As the glass softens under high temperature, the clamps are pulled apart, and the time dependence of the pulling force enables us to control the spatial profile of the taper diameter. In this study, the waist of the fiber taper ranged from 5 to 10 μm in diameter. The silica microspheres were fabricated by focusing a CO_2 laser beam onto an optical fiber, causing it to melt and form a sphere (Yang and Vahala 2003). By adjusting the position and the power of the laser, we can control the microsphere diameter in the range of 200 to 300 μm. To make the surfaces adhesive, we coated them with a single nm-thick layer of PAH to generate a uniform positive surface charge (Decher, et al. 1992). We then placed the samples in an aqueous solution containing negatively charged citrate-terminated, surfactant-free Au nanospheres (30 nm diameter, from Ted Pella) to initiate the deposition. We adjusted the NP concentration (n_0) as well as the deposition time (t) to achieve different surface particle densities, which were then determined by SEM imaging. The NP size d and stock suspension concentration n_s were verified with TEM and inductively coupled plasma atomic emission spectroscopy (ICP-AES), and found to be 28.7 nm and 1.95×10^{11} particles/cm^{-3} respectively, quite close to the values provided by the manufacturer (30 nm and 2.00×10^{11} particles/cm^{-3}). From d, the temperature of the suspension (22ºC) and the viscosity of water at that temperature (0.96 cP), we calculated the diffusion constant for the NPs $D = 1.57 \times 10^{-7}$ cm^2/s with the Einstein-Stokes equation,

$$D = \frac{k_b T}{6\pi \eta r} \tag{4.4}$$

where k_b is Boltzmann's constant, T is temperature, η is viscosity of the medium, and r is the radius of the particle.

To reduce the number of NPs adsorbed onto the surfaces during long depositions to the point where particle surface blocking (Adamczyk 2000; Adamczyk and Szyk 2000) was not a factor, the stock NP suspension was diluted with DI water so that n_0 ranged between 3.0 % and 30 % of n_s. The surface density of adsorbed particles was found by imaging several randomly selected regions of each surface with scanning electron microscopy, and then using image processing routines built into Mathematica to automatically count the particles in each image. The accuracy of this method was verified by manual counting of the particles in a subset of the images.

4.4 Results and Discussion

As suggested by Eq. (4.3), the NP deposition rate can vary by several orders of magnitude, depending on deposition time as well as the spatial dimension of the microstructure. For example, **Fig. 4.1** shows SEM micrographs of NPs adsorbed onto a microsphere, a tapered optical fiber and a flat glass substrate. In all cases, the surface was exposed to the suspension for 30 mins using suspensions with different particle concentration. The highest concentration of NPs was used in the flat surface deposition, yet this case shows the lowest density of adsorbed NPs.

The particle adsorption data was rescaled to enable comparison with Eq. (4.3). For the flat substrate, a was chosen to be 125 μm. We note that the precise value of a has no impact on the fitting for $\langle N_{\text{flat}}(t)\rangle$, as can be easily verified from Eq. (4.3) and the definition for $\nu(t)$. The result is plotted in **Fig. 4.3**, where we can see that the data, obtained with deposition times between 3 minutes and 6 hours, and values of a between 5 μm and 130 μm, follows the scaling of Eq. (4.3) quite well. The only free parameter in the rescaling was the NP concentration in the NS stock solution, n_s, which was chosen to obtain the best least squares fit to theory. The resulting values are displayed in **Tab. 4.1**. For all three geometries, the inferred value of n_s is quite close to the correct value of 2.0×10^{11} cm^{-3}, confirming the validity of our model.

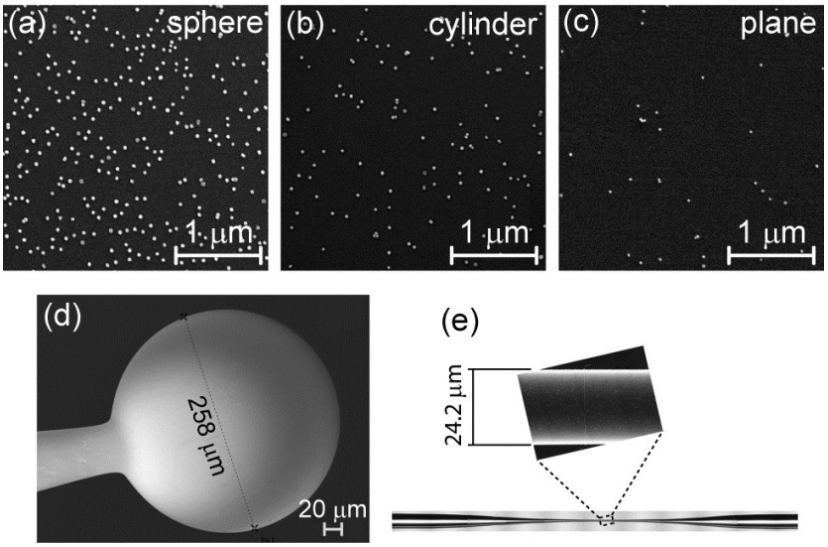

Fig. 4.1: SEM images of Au NSs deposited for 30 minutes from a diluted suspension onto (a) a spherical surface (129 μm radius, 10 % dilution from n_s), (b) a cylindrical surface (5.2 μm radius, 3% dilution), and (c) a planar surface (30 % dilution). The curved surfaces consist of (d) a 258 μm diameter microsphere and (e) a tapered optical fiber, 24.2 μm in diameter at the point where the image was taken.

The theory assumes quiescent conditions, and we would expect any fluid flow to increase the particle deposition rate onto the surfaces above the predicted values. In the case of the planar and spherical samples, it proved unnecessary to ensure a completely stagnant fluid. The depositions were carried out in standard glassware and simply left undisturbed for the desired amount of time, and despite the residual fluid motion inevitable in a large open container subject to the influence of air flow and ambient mechanical vibrations, agreement with theory is good. By contrast, if we place the cylindrical taper within an open container, we find the particle deposition rate is about 2.5 times larger than predicted by Eq. (4.2). To reduce the effect of fluid motion, the fiber tapers were enclosed in custom-made cylindrical fixtures with a 3 mm inside diameter as shown in **Fig. 4.2**. The fitting results with or without the stop flow fixture are displaced in **Tab. 4.1**. Using the fixture, n_s was inferred to be 1.88×10^{11} cm^{-3}, in good agreement with theory, whereas we found $n_s = 5.47 \times 10^{11}$ cm^{-3} if deposition was performed in an open container.

Insensitivity to slow flow is expected for deposition on a plane, since laminar flow in that case takes place parallel to the surface and does not mix fluid strata with different values of n. The reason for the insensitivity in the spherical case is less clear, but the small thickness of the fluid layer depleted of particles around an adsorbing sphere compared to a cylinder is likely an important factor. A more complete investigation of this problem would require numerical simulations (Petsi, et al. 2010), and will be left as a topic for future work.

Fig. 4.2: Schemetic of the cross-section of a stop flow fixture.

Tab. 4.1: Concentration of Au NSs in stock solution as determined by TEM and ICP-AES as well as absorption on different surface geometries and fitted to our model.

Method	TEM + ICP-AES	Flat Surface	Microsphere	Cylindrical Taper (Reduced Flow)	Cylindrical Taper
n_s **(10^{11}/cm^3)**	1.95	1.72	2.06	1.88	5.47

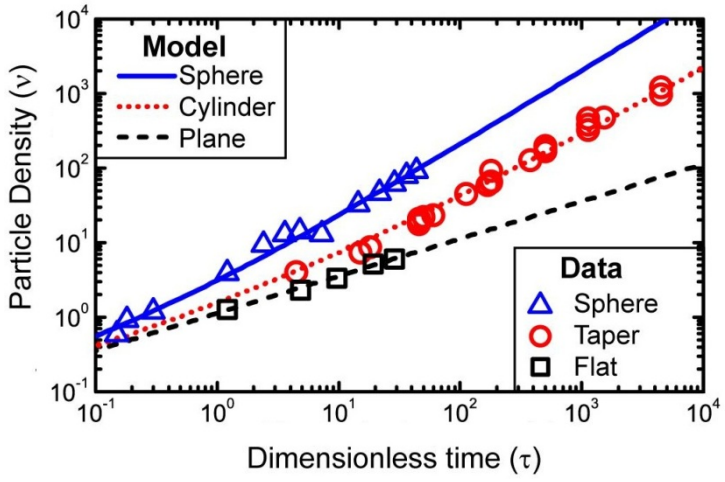

Fig. 4.3: Plot comparing the theoretical scaling in Eq. (4.3) with data obtained from planar, cylindrical and spherical surfaces. The only fitting parameter was n_s.

As is evident from **Fig. 4.1(e)**, the radius of each taper varies continuously from a few microns to the radius of the commercial optical fiber. A single deposition will therefore test Eq. (4.3) over a range of parameters. As can be seen in **Fig. 4.4**, the density of adsorbed NPs scales with a just as predicted by the model. For deposition times on the order of 30 mins, the density of NPs at the center of the taper can be more than an order of magnitude higher than at the edges. The strong dependence of particle density on curvature is particularly clear here.

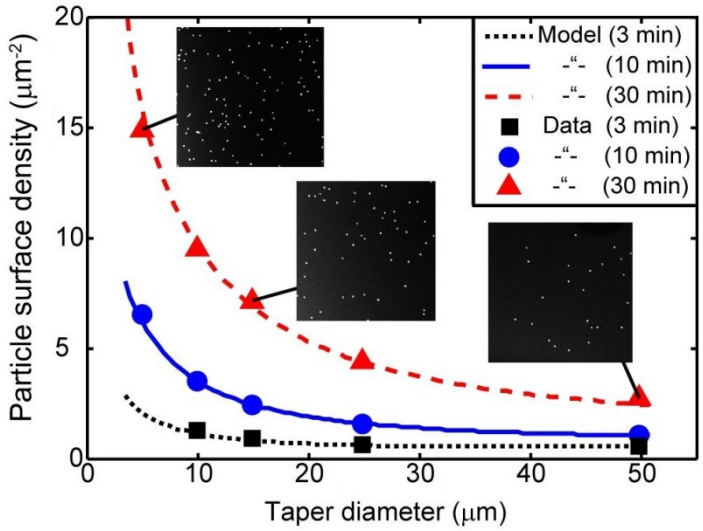

Fig. 4.4: Plots of the nanoparticle coverage on three different fiber tapers as a function of the local curvature, and for different deposition times. As in **Fig. 4.3**, the only fitting parameter was n_s. The inset SEM images are of 3 μm × 3 μm areas and are taken from the micrographs used to generate the indicated data points.

4.5 Conclusion

We have derived simple expressions describing adsorption of spherical particles onto adhesive spherical and cylindrical surfaces in the absence of flow, and shown that realistic deposition conditions are well described by the theory. Our main finding is that highly curved surfaces accumulate particles significantly faster than their flat counterparts at long deposition times, even though their behavior is identical at short deposition times. For the cases we have studied here, with deposition times on the order of minutes to hours, and radii of curvatures

down to approximately 10 μm, the difference in surface particle density can be as large as two order of magnitude. This needs to be taken into account whenever particles or other nanostructures are deposited from suspension onto surfaces that are not flat. The effect can be advantageous both in device fabrication and in sensing applications, where a sensor placed on a highly curved surface will have a faster response than one placed on a flat surface (Wagner, et al. 2006).

4.6 Theoretical Derivation

Solving the diffusion equation

The time evolution of a particle concentration $n(\mathbf{r},t)$ in a dilute liquid suspension generally follows from

$$\frac{\partial n}{\partial t} = \nabla \cdot \left(D \left(\nabla n - \mathbf{F} \frac{n}{k_B T} \right) - \mathbf{v} n \right) \tag{S1}$$

In the absence of external forces ($\mathbf{F} = 0$) and liquid flow ($\mathbf{v} = 0$), this reduces to the standard diffusion equation. For the problem at hand, we also assume that the diffusion constant is invariant over space, which gives us

$$\begin{cases} \partial_t n = D \nabla^2 n \\ n(\mathbf{r}, 0) = n_0 \\ n(\mathbf{r}_s, t) = 0, n(\infty, 0) = n_0 \end{cases} \tag{S2}$$

where the second and third line indicate the initial conditions and boundary conditions, respectively. The first (or inner) boundary condition results from the perfect sink assumption, *i.e.* that all particles that come sufficiently close to the adsorbing surface located at $\{\mathbf{r}_s\}$ will irreversibly stick to it. This equation can be solved with separation of variables, that is by taking $n(\mathbf{r},t) = R(\mathbf{r})T(t)$. With this ansatz, we obtain

$$\frac{1}{D}\frac{T'}{T} = \frac{\nabla^2 R}{R} = -\beta^2 \tag{S3}$$

where β is a real positive number which we will use to index the different solutions. The solution for $T_\beta(t)$ is

$$T_\beta(t) = e^{-Dt\beta^2} \tag{S4}$$

in all cases, while the form of $R_\beta(\mathbf{r})$ depends on the shape of the collecting surface. We will select these solutions with constraint that the $R_\beta(\mathbf{r}_s) = 0$, so that the total solution

$$n(\mathbf{r}, t) = \int C_\beta \, R_\beta(\mathbf{r}) T_\beta(t) d\beta \tag{S5}$$

automatically satisfies the inner boundary condition. In the next step, C_β is chosen so that the initial condition is satisfied:

$$n(\mathbf{r}, 0) = \int_0^\infty C_\beta \, R_\beta(\mathbf{r}) d\beta = n_0 \tag{S6}$$

Doing this, we automatically satisfy the boundary condition at infinity, so this completely solves Eq. S2. By Fick's first law, which is valid here, the flow of particles onto the collecting surface is given by

$$\Phi(\mathrm{t}) = D\nabla_\perp n(\mathbf{r}_s, t) \tag{S7}$$

where $\nabla_\perp$ is the spatial derivative normal to the surface. The average accumulated density of particles on the collecting surface is then simply

$$\langle N(t) \rangle = \int_0^t \Phi(t') dt' \tag{S8}$$

Planer case

For a flat surface located at $x = 0$, the spatial part of Eq. S3 is

$$\partial_{xx} R_\beta(x) = -\beta^2 R_\beta(x) \tag{S9}$$

This gives us

$$R_\beta(x) = n_0 \sin \beta x \tag{S10}$$

as the solution that satisfies the inner boundary condition. Since $\int_0^\infty \frac{\sin \beta x}{\beta} d\beta = \frac{\pi}{2}$ for $x > 0$, we have $C_\beta = \frac{2}{\pi\beta}$, so that the full solution is

$$n_{\text{flat}}(x,t) = \frac{2n_0}{\pi} \int_0^\infty e^{-Dt\beta^2} \frac{\sin \beta x}{\beta} d\beta = n_0 \operatorname{erf}\left(\frac{x}{\sqrt{4Dt}}\right) \tag{S11}$$

We therefore have

$$\begin{aligned} \Phi_{\text{flat}}(t) &= n_0 \sqrt{\frac{D}{\pi t}} \\ \langle N_{\text{flat}}(t) \rangle &= 2n_0 \sqrt{\frac{Dt}{\pi}} \end{aligned} \tag{S12}$$

Spherical case

The spatial part of Eq. S3 is one-dimensional in spherical coordinates:

$$\frac{R_\beta''}{R_\beta} + \frac{2}{r}\frac{R_\beta'}{R_\beta} = -\beta^2 \tag{S13}$$

This has the general solution

$$R_\beta(r) = A_\beta \frac{\sin \beta r}{\beta r} + B_\beta \frac{\cos \beta r}{\beta r} \tag{S14}$$

If the sphere has radius a, the left boundary condition $R(a) = 0$ can be satisfied by taking $A_\beta = \cos \beta a$ and $B_\beta = -\sin \beta a$. The initial condition then becomes

$$\int_0^\infty \frac{C_\beta}{\beta r} \sin \beta (r - a)\, d\beta = n_0 \quad (r > a) \tag{S15}$$

To solve this, we reformulate the initial condition as $n(r > a, 0) = \lim_{Q\to\infty} n_0 \Pi(2Q)$, where $\Pi(x)$ is the rectangle function. Multiplying by r and making the substitution $p = r - a$, we obtain, after a sine transform in p,

$$C_\beta = \frac{2n_0 a}{\pi}\left(1 - \left(\frac{Q}{a} + 1\right)\cos \beta Q + \frac{\sin \beta Q}{\beta a}\right) \tag{S16}$$

Noticing that

$$\int_0^\infty \frac{\sin(r - a)\beta \ \cos Q\beta}{\beta} d\beta = \begin{cases} \frac{\pi}{2} & (r - a > Q) \\ \frac{\pi}{4} & (r - a = Q) \\ 0 & (r - a < Q) \end{cases} \tag{S17}$$

We see that the contribution of the middle term of Eq. S16 to $n_{\text{sph}}(r, t)$ goes to 0 as $Q \to \infty$. We then obtain

$$n_{\text{sph}}(r, t) = \frac{2n_0 a}{\pi} \lim_{Q\to\infty} \int_0^\infty e^{-Dt\beta^2} \left(1 + \frac{\sin \beta Q}{\beta a}\right) \frac{\sin \beta (r - a)}{\beta r} d\beta \tag{S18}$$

which gives us

$$\Phi_{\mathrm{sph}}(t) = D\frac{\partial n(a,t)}{\partial r}$$
$$= \frac{2n_0 D}{\pi}\lim_{Q\to\infty}\int_0^\infty e^{-Dt\beta^2}\left(1+\frac{\sin\beta Q}{\beta a}\right)d\beta = n_0\left(\sqrt{\frac{D}{\pi t}}+\frac{D}{a}\right) \quad \text{(S19)}$$

and therefore

$$\langle N_{sph}\rangle = n_0\left(2\sqrt{\frac{Dt}{\pi}}+\frac{Dt}{a}\right) \quad \text{(S20)}$$

Cylindrical case

The spatial part of Eq. S3 becomes one-dimensional if we pass into cylindrical coordinates, in which case we get

$$\frac{R_\beta''}{R_\beta} + \frac{1}{r}\frac{R_\beta'}{R_\beta} = -\beta^2 \quad \text{(S21)}$$

which has solutions in terms of Bessel functions

$$R_\beta(r) = A_\beta J_0(\beta r) + B_\beta Y_0(\beta r) \quad \text{(S22)}$$

The inner boundary condition ($R_\beta(a) = 0$, if the cylinder has radius a) can be satisfied by taking $A_\beta = Y_0(\beta a)$ and $B_\beta = -J_0(\beta a)$. Noting that

$$\int_0^\infty \frac{J_\nu(ax)Y_\nu(bx) - J_\nu(bx)Y_\nu(ax)}{x\{[J_\nu(bx)]^2 + [Y_\nu(bx)]^2\}}dx = -\frac{\pi}{2}\left(\frac{b}{a}\right)^\nu \qquad (0<b<a) \quad \text{(S23)}$$

we can set C_β so that the initial condition is satisfied, and we obtain

$$n_{\mathrm{cyl}}(r,t) = \frac{2n_0}{\pi}\int_0^\infty e^{-Dt\beta^2}\frac{J_0(\beta a)Y_0(\beta r) - J_0(\beta r)Y_0(\beta a)}{\beta\{[J_0(\beta a)]^2 + [Y_0(\beta a)]^2\}}\,d\beta \tag{S24}$$

From this it is easy to show that

$$\Phi_{\mathrm{cyl}}(t) = \frac{2n_0 D}{\pi}\int_0^\infty e^{-Dt\beta^2}\Im\left\{\frac{H_1^{(2)}(\beta)}{H_0^{(2)}(\beta)}\right\}d\beta \tag{S25}$$

which can be integrated numerically to give $N_{\mathrm{cyl}}(t)$.

Approximation to the cylindrical solution

The integration in Eq. S25 cannot be carried out explicitly, but it can be approximated in the limits of long and short times. Using the definitions in the paper, we write the surface adsorption rate in dimensionless form:

$$\varphi_{\mathrm{cyl}}(\tau) = \frac{2}{\pi}\int_0^\infty e^{-\tau\beta^2}\Im\left\{\frac{H_1^{(2)}(\beta)}{H_0^{(2)}(\beta)}\right\}d\beta \tag{S26}$$

The function $g_{\mathrm{cyl}}(\beta) = \Im\left\{\frac{H_1^{(2)}(\beta)}{H_0^{(2)}(\beta)}\right\}$ diverges at $\beta = 0$, but, as can be shown from the asymptotic form of the Hankel functions, rapidly approaches 1 for $\beta > 0$. For sufficiently small τ, we can therefore approximate

$$\varphi_{\mathrm{cyl}}(\tau) \approx \frac{2}{\pi}\int_0^\infty e^{-\tau\beta^2}\,d\beta + \frac{2}{\pi}\int_0^\infty\left(\Im\left\{\frac{H_1^{(2)}(\beta)}{H_0^{(2)}(\beta)}\right\} - 1\right)d\beta = \frac{1}{\sqrt{\pi\tau}} + \frac{1}{2} \tag{S27}$$

and therefore

$$\langle\nu_{\mathrm{cyl}}(\tau)\rangle \approx 2\sqrt{\frac{\tau}{\pi}} + \frac{\tau}{2} \tag{S28}$$

For large values of τ, only the region near $\beta = 0$ will contribute to the integral in Eq. S26. Under those circumstances, we have that

$$g_{\text{cyl}}(\beta) = \frac{\pi}{2\beta\left\{\left(\frac{\pi}{2}\right)^2 + \left(\ln\frac{\beta}{2} + \gamma\right)^2\right\}} + O(\beta^2) \tag{S29}$$

Here, γ is Euler's constant. Even with this simplification, Eq. S26 cannot be solved analytically. If we replace the Gaussian weight with its Taylor expansion and cut off the integration at some upper bound $C/\sqrt{\tau}$, we obtain

$$\varphi_{\text{cyl}}(\beta) \approx \sum_{n=0}^{\infty} \int_0^{C/\sqrt{\tau}} \frac{(-\tau\beta^2)^n}{n!\,\beta\left\{\left(\frac{\pi}{2}\right)^2 + \left(\ln\frac{\beta}{2} + \gamma\right)^2\right\}} d\beta \tag{S30}$$

The cut-off is necessary if we are to be able to reverse the order of integration and summation, but does not reduce the validity of the approximation. Solving the integral we obtain

$$\varphi_{\text{cyl}}(\beta) \approx \frac{2}{\pi}\left[\operatorname{arccot}\frac{\ln K\tau}{\pi} + \sum_{n=1}^{\infty} \frac{(4e^{-2\gamma}\tau)^n}{n!}\left(\pi - \Im\left\{\operatorname{Ei}\left(n\ln\frac{-1}{K\tau}\right)\right\}\right)\right] \tag{S31}$$

where $K = \frac{4}{C^2}e^{-2\gamma}$, and $\operatorname{Ei} x$ is the exponential integral function. This approximation is only valid for large values of τ, so we cannot simply apply Eq. S8 to find an expression which approximates the accumulated particle density. We therefore add an adjustable parameter A to integral, which gives us

$$\langle \nu_{\mathrm{cyl}}(\tau) \rangle \approx \frac{2}{\pi}\Bigg(A + \tau \operatorname{arccot}\frac{\ln K\tau}{\pi} + \\ + \sum_{n=1}^{\infty} \frac{(4e^{-2\gamma})^n \tau^{n+1}}{(n+1)!}\left(\pi - \Im\left\{\mathrm{Ei}\left(n \ln\frac{-1}{K\tau}\right)\right\}\right) \\ - \frac{(-C^2)^{n-1}}{n!\,K}(\pi - \Im\{\mathrm{li}(-K\tau)\})\Bigg) \tag{S32}$$

where $\mathrm{li}(x) = PV\int_0^x \frac{dt}{\ln t}$ is the logarithmic integral function. We achieve an adequate approximation by terminating this expression at the arccot term. Choosing $C = 1.478$ and $A = 1$ results in a good compromise between accuracy at large and intermediate values for τ, with an error less that 1.25 % for $\tau > 6$, and only 5.5 % for $\tau = 2$. Our chosen value for C yields $K = 0.5772$, tantalizingly similar to Euler's constant $\gamma = 0.577215$ ... Our final approximation for $\langle \nu_{\mathrm{cyl}}(\tau) \rangle$ is then

$$\langle \nu_{\mathrm{cyl}}(\tau) \rangle \approx \begin{cases} 2\sqrt{\frac{\tau}{\pi}} + \frac{\tau}{2} & (\tau \le 2) \\ \frac{2}{\pi}\left(\tau \operatorname{arccot}\frac{\ln(0.5772\,\tau)}{\pi} + 1\right) & (\tau > 2) \end{cases} \tag{S33}$$

Chapter 5 Dynamically pH-Tunable Plasmon Resonance Using a Responsive Polyelectrolyte Multilayer Film

We have studied the tunable plasmon resonance of a hybrid structure consisting of a Au nanosphere (NS) and a Au-coated substrate separated by a polyelectrolyte multilayer (PEM) film. The PEM film swells and shrinks when the pH changes because of charging and discharging of the polyelectrolytes. Therefore, this PEM film provides an efficient means to tune the distance between the Au NS and the Au-coated substrate and hence the coupling strength between spheres and surface. For 100 nm diameter Au NSs, the localized surface plasmon resonances (LSPRs) could be shifted as much as 100 nm in wavelength by changing the pH of the water bath between 3 and 10. Our preliminary estimates indicate that the gap between sphere and surface can be as small as a few nm even though the film itself is tens of nm thick.

5.1 Introduction

The simple structure of a Au NS separated from a Au film by a dielectric spacer has been the subject of significant interest in the plasmonics community. On resonance, the coupling between sphere and surface creates a region with high electric field intensity inside the gap between the sphere and the surface. By changing the gap size, even down to a few nanometer range, this plasmonic gap mode can be tuned across a large wavelength range. A dielectric spacer layer is usually used to control the gap size. A polyelectrolyte multilayer (PEM) film or an ionic self-assembled monolayer (ISAM) film is a good candidate for such a spacer since their thickness can be easily tailored with nanometer accuracy.

We use PEM films consisting of a weak polyelectrolyte, poly(allylamine hydrochloride) (PAH), and a strong polyelectrolyte, poly(sodium 4-styrenesulfonate) (PSS), as the spacer layer.

The details of the PAH, PSS can be found in Secs. 3.2 and 3.3. When a PEM film is fabricated at higher pH condition, more PAH is attracted by a negatively charged surface, such as a PSS layer or a thiolated surface. This is because the amine side groups in PAH lose charge at a higher pH, therefore more PAH needs to be adsorbed onto the negatively charged surface before charge reversal occurs and deposition stops. When the completed film is later immersed in a low-pH water bath, the uncoordinated amines of the PAH regain their charges, and the film swells due to the Coulomb repulsion. The higher the pH used during film assembly, the more PAH the films will contain, and the thicker the film as a consequence will become. The measured swelling of a PEM film assembled at pH 9.5 can be as high as 500 % from its shrunken state when immersed in a pH 2.0 water bath (Itano, et al. 2005). The swelling can be reversed by exposing the film to a high pH, which causes the amines to become uncharged and cluster into hydrophobic region, expelling water from the film, causing it to shrink. The swell/shrink process is highly repeatable. There is not much swelling for a PEM film fabricated below pH 8.5. The swelling/shrinking process of the PEM film changes the coupling strength between the Au NS and Au-coated substrate.

5.2 Theory

Wind and co-workers (Wind, et al. 1987) used a quasi-static calculation to solve a scattering problem for a sphere above a substrate. In this calculation, the retardation effect has been neglected. This means the incident beam has been taken to be infinite in this method. The schematic configuration of the calculation is shown in **Fig. 5.1**.

According to Wind's method (Okamoto and Yamaguchi 2003; Wind, et al. 1987), when the incident electric field is perpendicular to the substrate, the linear equations are given by

$$\frac{1}{4\pi\varepsilon_2 a^3}\sum_{j=1}^{\infty}\left(\delta_{lj}+\left\{\frac{l(\epsilon_1-\epsilon_2)(\epsilon_2-\epsilon_3)}{[l\epsilon_1+(l+1)\epsilon_2](\epsilon_2+\epsilon_3)}\right\}\left[\frac{(l+j)!}{l!\,j!\,(2d/a)^{l+j+1}}\right]\right)\alpha_{\perp j} = \frac{\epsilon_1-\epsilon_2}{\epsilon_1+2\epsilon_2}\delta_{l1} \qquad (l=1,2,\ldots) \tag{5.1}$$

and when it is parallel to the substrate, it is given by

$$\frac{1}{4\pi\varepsilon_2 a^3}\sum_{j=1}^{\infty}\left(\delta_{lj}+\left\{\frac{l(\epsilon_1-\epsilon_2)(\epsilon_2-\epsilon_3)}{[l\epsilon_1+(l+1)\epsilon_2](\epsilon_2+\epsilon_3)}\right\}\left[\frac{(l+j)!}{(l+1)!\,(j-1)!\,(2d/a)^{l+j+1}}\right]\right)\alpha_{\parallel j} = \frac{\epsilon_1-\epsilon_2}{\epsilon_1+2\epsilon_2}\delta_{l1} \qquad (l=1,2,\dots) \tag{5.2}$$

where $\alpha_{\perp \mathrm{j}}$ or $\alpha_{\parallel \mathrm{j}}$ is the j^{th} multipolar polarizability of the perpendicular or the parallel case. The absorption, scattering and extinction efficiencies of a sphere for a *p*-polarized incident beam with angle of incidence θ are given by

$$Q_{\mathrm{abs}} = \frac{k}{\pi a^2}\sqrt{\mathrm{Im}^2\left[\left|1+r_p\right|\sin\theta\,\alpha_{\perp}\right]+\mathrm{Im}^2\left[\left|1-r_p\right|\cos\theta\,\alpha_{\parallel 1}\right]} \tag{5.3}$$

$$Q_{\mathrm{sca}} = \frac{k^4}{6\pi^2 a^2}\left(\left|\left|1+r_p\right|\sin\theta\,\alpha_{\perp}\right|^2+\left|\left|1-r_p\right|\cos\theta\,\alpha_{\parallel 1}\right|^2\right) \tag{5.4}$$

$$Q_{\mathrm{ext}} = Q_{\mathrm{abs}} + Q_{\mathrm{sca}} \tag{5.5}$$

where k is wavenumber in the medium, and r_p is the Fresnel reflection coefficient for *p*-polarized beams, which is

$$r_p = \left|\frac{n_1\cos\theta_{\mathrm{t}} - n_2\cos\theta_{\mathrm{i}}}{n_1\cos\theta_{\mathrm{t}} + n_2\cos\theta_{\mathrm{i}}}\right|^2 \tag{5.6}$$

For all our measurements, the angle of incidence of the *p*-polarized beam is 75º, the sphere and the substrate are both Au and the medium is water. By tabulating the bulk dielectric functions of Au from (Johnson and Christy 1972), we can obtain the extinction spectra for spheres of different sizes with different gap distances to the thick Au film. Some results for 60 nm spheres with varying gap distances from the Au substrate are shown **Fig. 5.2**. We will use this as an example theoretical calculation for our experimental measurements. We define the *redshift* as the difference between the peak wavelengths of the sphere plasmon resonances with and without the Au substrate. The redshift of the spectrum has already been very small for a 4

nm gap; therefore, when the gap is as large as 100 nm, the sphere does not seem to be affected by the substrate. We see from this graph that for a 60 nm sphere, when the gap distance is 0.5 nm, the redshift is 793 – 522 = 271 (nm). By using the redshift rather than the absolute wavelengths, we can compare the calculation to our data, even though the sphere resonances are different in the two cases. (For example, the measured peak wavelength for 60 nm sphere suspension from **Fig. 1.3** is 536 nm, instead of 522 nm.)

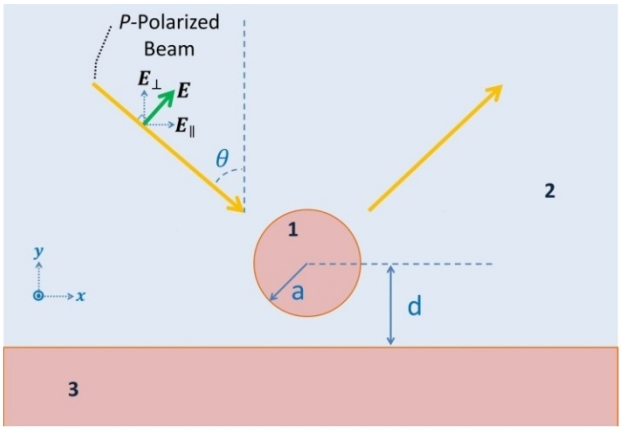

Fig. 5.1: Schematic configuration of the system for theoretical calculation. Here, d is the gap distance plus the sphere radius a.

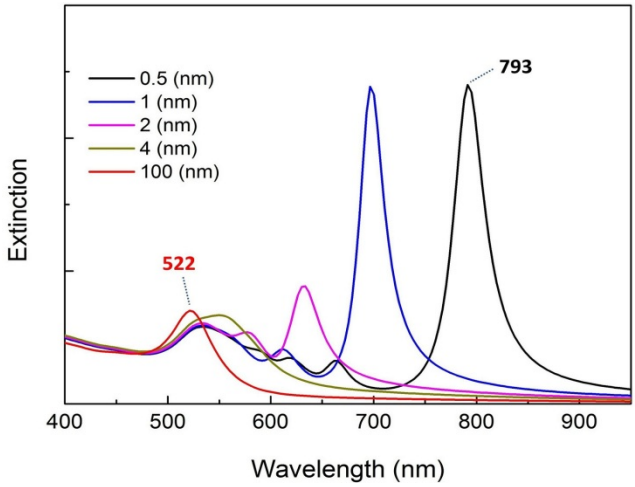

Fig. 5.2: Calculated extinction spectra for 60 nm Au NSs with varying gap distances from the Au substrate.

Fig. 5.3A shows the calculated redshifts for spheres of different radii and gap distances. Smaller gaps are associated with larger redshifts. The redshift is larger for spheres of larger diameter under the same gap distance. **B** is the logarithmic plot. As the lines in this plot are nearly straight, this means the relation between the gap distances and the redshifts follows the power law with exponent = –1.52 for redshifts smaller than ~250 nm.

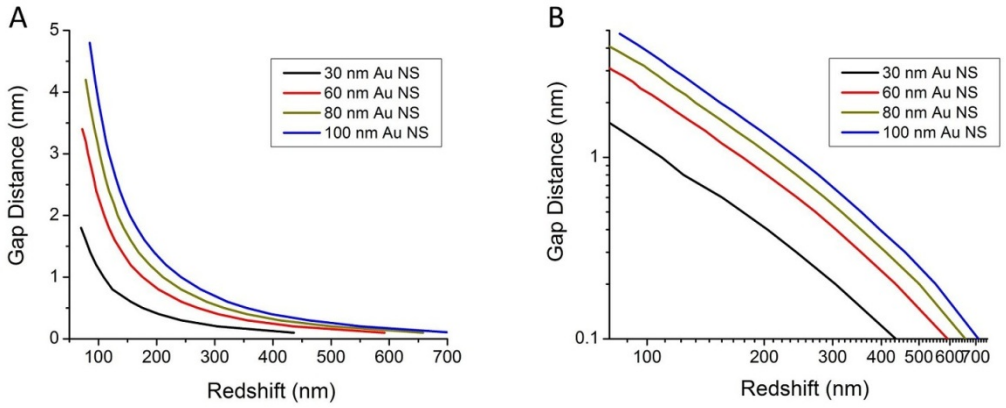

Fig. 5.3: Calculated redshifts of the extinction spectra for Au spheres of different diameters and gap distances from the Au substrate. A) Linear graph; B) Logarithmic graph.

5.3 Experimental Section

Preparation of PEM film samples

In a typical experiment, microscope slides were cleaned in aqua regia solution for 10 mins, then rinsed with DI water, and dried with a stream of nitrogen gas. After cleaning, the slides were mounted on the sample holder of an e-beam evaporator (Thermonics VE-100), followed by the evaporation of 10 nm Ti (99.99 % purity, Kurt J. Lesker) as an adhesion layer at a rate of 0.1 Å/s and 140 nm Au (99.99 % purity, International Advanced Material) at a rate of 0.5 Å/s. The samples here in most cases immediately soaked into an ethanol solution of 1 mM 11-mercaptoundecanoic acid (11-MUA) for 16 h in order to form a charged self-assembled

monolayer on the substrate. The thiol layer is discussed in more detail in the ***thiol layer*** subsection below.

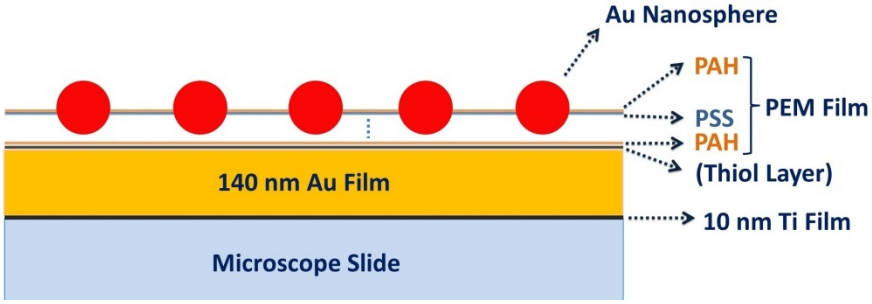

Fig. 5.4: Schematic of Au NSs and Au substrate hybrid structure.

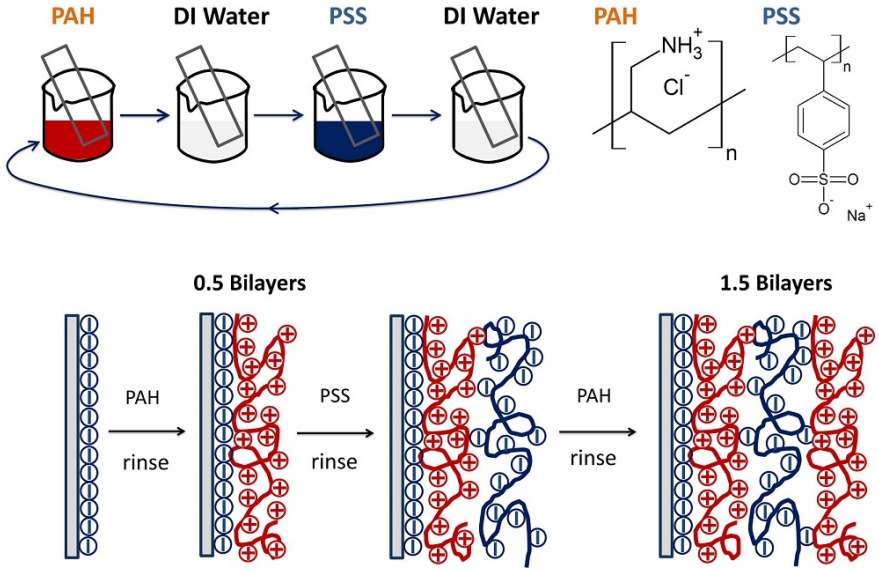

Fig. 5.5: Illustration of polyelectrolyte multilayer (PEM) film preparation

The PEM film in **Fig. 5.4** was fabricated with the layer-by-layer (LBL) adsorption (Decher 1997) as illustrated in **Fig. 5.5**. Three beakers, containing DI water, 10 mM cationic poly(allylamine hydrochloride) (PAH, M_w ~15,000, cationic) and 10 mM anionic poly(sodium 4-styrenesulfonate) (PSS, M_w ~70,000) on a monomer basis were adjusted to a pH between 8.5 and 9.5 by adding sodium hydroxide. The negatively charged thiol-coated substrates were then submerged in a PAH solution for 5 mins and rinsed with DI water. We will refer the samples at

this stage as 0.5-bilayer PEM films. The substrates were then submerged in PSS solution for 5 mins and again rinsed with DI water resulting in a 1-bilayer film. This process was repeated to make films consisting of between 0.5 bilayers and 4.5 bilayers, always ending with a positively charged PAH layer so that the negatively charged Au NSs can be adsorbed onto the PEM films. After the final rinse step, the slides were dried with nitrogen gas.

After film deposition, the substrates were partially immersed in a Au NS suspension which was diluted to half of its initial, as-received concentration. The final pH values of the solutions after dilution were close to neutral. The partial immersion resulted in particle adsorption onto the lower 2 cm of the substrates, while the rest was kept free of nanoparticles. The incubation time varied with the diameter of the spheres—longer times were used for the larger spheres. This was due to the difference between the initial concentrations of the NS suspensions. The nominal particle concentration of the 30 nm diameter NS suspension obtained from Ted Pella was 2.0×10^{11} particles/mL; while it was 2.6×10^{10} particles/mL for the 60 nm spheres; 1.1×10^{10} particles/mL for the 80 nm spheres and 5.6×10^{9} particles/mL for the 100 nm spheres. In most cases, the incubation time was about 4 h for 30 nm spheres, 6 h for 60 nm spheres, 7 h for 80 nm spheres, and 10 h for 100 nm spheres. In order to avoid inhomogeneous adsorption, there was no stirring during incubation. The larger spheres had settled to the bottom after a few hours. After the particle deposition, samples were rinsed with DI water and dried with nitrogen. This completes the sample preparation.

Fig. 5.6 shows SEM images of different size of Au NSs on a 0.5-bilayer PEM film (PAH). The NS density did not show much dependence on the number of bilayers in the PEM nor on whether a thiol layer was present under the PEM films. The distances between the spheres are large enough that there is no coupling between their plasmons. Therefore, the density of the spheres only affects the intensity of the resonance peak but not its spectral position. The larger spheres, with 80 or 100 nm diameter, have higher extinction efficiencies than the 30 nm spheres (Jain, et al. 2006), so we were able to obtain a good signal/noise ratio with a lower particle density.

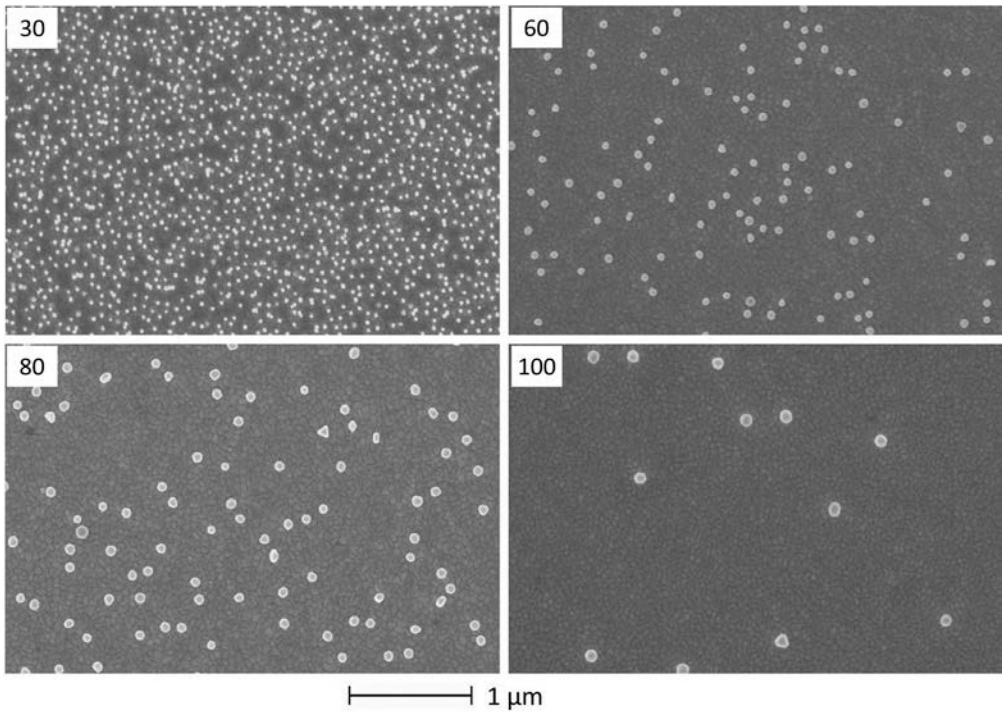

Fig. 5.6: SEM images of 30, 60, 80, and 100 nm Au NSs on a PEM film.

Thiol layer

In our experiments, we mainly use 11-MUA as the thiol layer. In some cases, 3-mercaptopropionic (3-MPA) acid or 16-mercaptohexadecanoic acid (16-MHDA) was used instead.

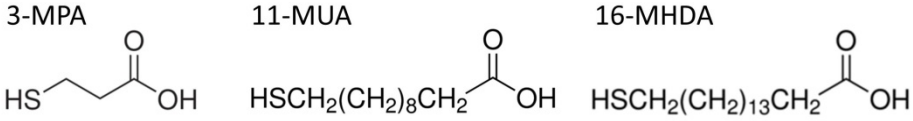

Fig. 5.7: Molecular structures of 3-mercaptopropionic acid, 11-mercaptoundecanoic acid and 16-mercaptohexadecanoic acid.

The shorter or longer carbon chains give the thiol layers different thicknesses which affects the substrate-particle separation. The thiols were dissolved in ethanol and with several drops of concentrated hydrochloric acid added to prevent the formation of hydrogen bonds between thiols

ensuring a single monolayer on the Au surface. In addition, we also have prepared some samples without a thiol layer by directly soaking the substrate in a PAH solution after the Au evaporation. The role of thiol layers is to provide a better coating of PAH since they give the surface strong negative charges.

Extinction spectrum measurement

The PEM film samples were placed inside a home-made glass cuvette fixed on a movable rail carriage (Thorlabs, XT66P2/M), which was mounted on a construction rail (Thorlabs, XT66) as shown in **Fig. 5.8**. The incident beam from a halogen light source (Ocean Optics DH-2000) passed through a collimator and a Glan-Taylor calcite polarizer (Thorlabs p/n GT10-A) before reaching the sample. The specularly reflected and forward scattered light was collected by a bi-convex lens and focused on the input fiber of a high-resolution miniature fiber optic spectrometer (Ocean Optics, HR2000). The incident angle on the cuvette was 70 degrees, corresponding to 75° incidence on the sample inside the cuvette.

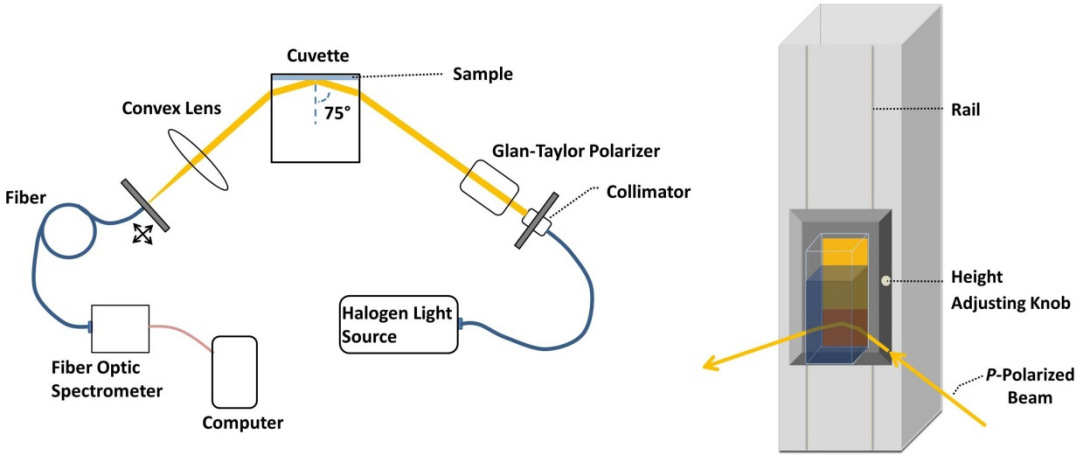

Fig. 5.8: Diagrams of the extinction spectrum measurement. The *p*-polarized light is incident from the right-hand side. The specularly reflected and forward scattered light was collected by the spectrometer on the left-hand side.

For each sample, spectra were taken at both pH 10 and pH 3 conditions. Firstly, the cuvette was filled with pH 10 water. The sample was then immersed in the bath for 3 mins in order to allow the PEM film to stabilize before a reference spectrum (I_0) was taken from the upper region,

where no Au spheres were present on the sample surface. The rail carriage was then moved upward to expose the lower region, which contained spheres, to the incident light and a sample spectrum (I) was taken. The extinction spectrum was calculated as $E = -\log(I/I_0)$. After that, the cuvette was filled with pH 3 water. Another sample spectrum was taken after 3 mins of immersion. This process can be repeated as desired.

5.4 Results and Discussion

Fig. 5.9 shows the analysis of the sample data that will be applied for all the data in this chapter. In this case, 60 nm NSs were sitting on top of a 3.5-bilayer PEM film ($(PAH/PSS)_2/PAH$) which was assembled at pH 9.5 on a 11-MUA thiol layer on the Au substrate. The *suspension spectrum* was extracted from **Fig. 1.3**. The peak wavelength of the spectrum when the sample was soaked in a pH 10 water bath was 637 nm; and when in pH 3 water, it was 586 nm. The difference between the peak wavelength at pH 10 and the Au NS suspension will be referred as **p polarization shift;** the difference between the peak wavelengths at pH 10 and pH 3 will be referred as **swell blueshift** as indicated in the figure.

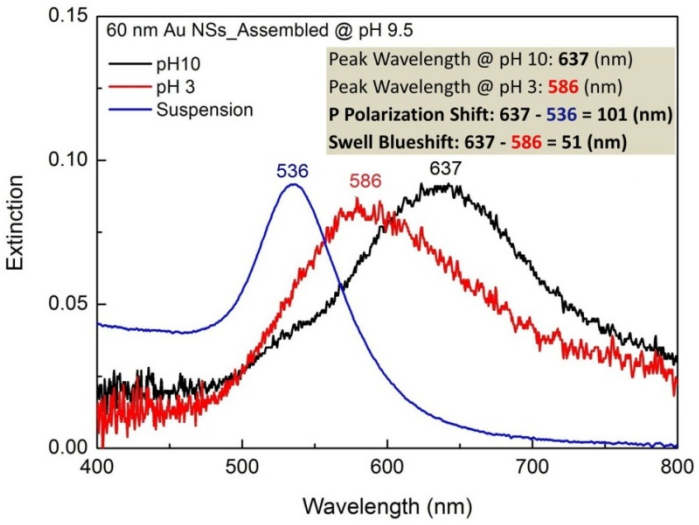

Fig. 5.9: Extinction spectra of 60 nm diameter Au spheres sitting on top of a PEM film and a thiol layer above a Au substrate in a water bath at pH 10 and 3, and spheres that are freely suspended in water.

The thicknesses of the PSS layers do not change since PSS is fully charged under all pH values. The PEM film shrinks at pH 10 due to the discharging of the amines of the PAH on the PEM film bringing the NSs closer to the Au film. Therefore, the coupling between the Au spheres and the Au substrate is stronger causing the peak wavelength to redshift. The PEM film swells at pH 3 due to the charging of the amines repelling each other. This moves the spheres away from the surface, so that the coupling becomes weaker. In addition to the strongly red-shifted peak, the extinction spectrum also contains a smaller peak around 536 nm. This peak is the result of the component of the incident electric field that is parallel to the surface exciting a plasmon mode in the Au sphere, which is only weakly coupled to the surface and therefore barely shifts from its free suspension value.

Fig. 5.10 plots the wavelength of the plasmon peak in samples with their PEM films assembled at pH 9.0. We can see that for spheres of various diameters, the number of bilayers in the PEM film can tune the plasmon resonances as much as 250 nm. The swell blueshifts are also larger when the sphere diameters are larger. This demonstrates that we are able to dynamically tune the gaps between NSs and surface in the range of a few nm.

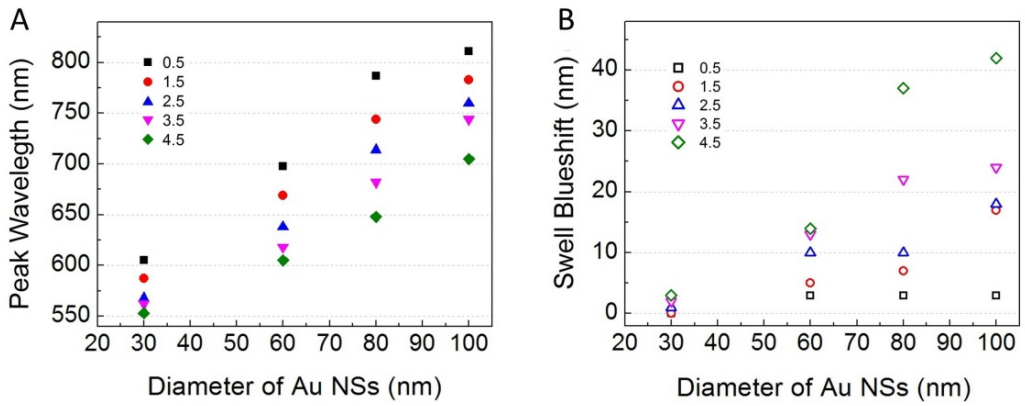

Fig. 5.10: Summary of the peak wavelengths and swell blueshifts of samples with PEM films assembled at pH 9. A) In a pH 10 water bath and B) the blueshifts when samples were switched to a pH 3 bath.

Fig. 5.11 summarizes the peak shifts obtained from films fabricated at different pH containing different numbers of bilayers, and with different size NSs adsorbed onto them. The

solid lines indicate the p polarization shifts, and the dotted lines the swell blueshifts. The blue lines correspond to samples without a thiol layer beneath the PEM film, and the red lines to samples with a layer of thiol (11-MUA) between the Au substrate and the PEM film. Rubner and coworkers (Itano, et al. 2005) measured the thickness per PAH/PSS films assembled at different pH using an ellipsometer and found 2.5, 4.0, 4.6 and 4.9 nm/bilayer for films assembled at pH 8.5, 9.0, 9.3 and 9.5, respectively. Focusing on the data from 80 nm Au NSs, we can see that films assembled at different pH values give very similar p polarization shifts. From the calculated results in **Fig. 5.3A**, these shifts correspond to gap distances less than 1 nm to for the 0.5-bilayer films, and less than 1.5 nm for the 2.5-bilayer films. These values are much smaller than Rubner's measurements for the unstrained films, which likely means that the Au NSs were embedded in the PEM film, instead of sitting on top of it. This is reasonable, since an embedded configuration minimizes the electrostatic energy of the interaction between the negatively charged NSs and the positively charged film. The p polarization shift does however depend strongly on the number of bilayers in the film. It appears that each bilayer has a minimum thickness, below which the electrostatic force between film and sphere cannot compress it.

For films assembled at a higher pH (≥ 9.3), there is substantial variation between spectra obtained from different swell/shrink cycles. This may be because the films assembled at high pH are rougher, so that the sphere-surface gaps vary more in these samples. For films assembled at lower pH (≤ 9.0), the results are more repeatable. This can be seen in the panel in **Fig. 5.11** that corresponds to samples prepared at pH 9.0 and with 80 nm Au NSs, where data sets from two measurement cycles are displayed, and agree quite well with each other.

The swell blueshift depends on number of bilayers in the films, the assembling pH and the size of the spheres. Films assembled at higher pH and with larger Au NSs give larger swell blueshifts. This is consistent with the notion that films assembled at a higher pH contain more uncoordinated amines and therefore swell more, resulting in larger swell blueshifts.

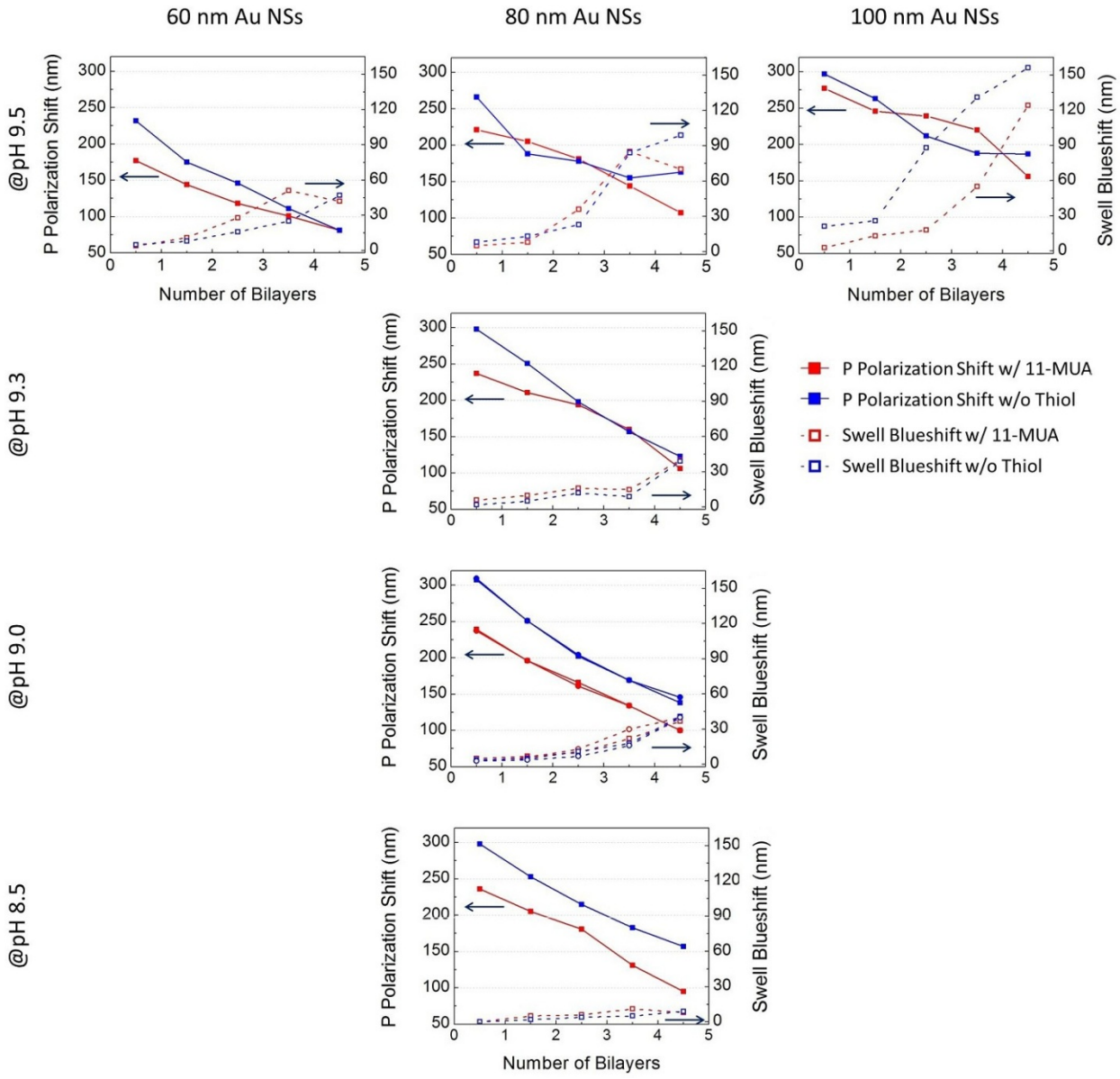

Fig. 5.11: Summary of the peak shifts obtained from films fabricated at different pH containing different numbers of bilayers, and with different size NSs. The blue lines correspond to samples without a thiol layer beneath the PEM film, and the red lines to samples with a layer of thiol (11-MUA) between the Au substrate and the PEM film. (The definitions of p polarization shift and swell blueshift were given in **Fig. 5.9**.)

In order to understand the thickness effect of the thiol layer, we prepared samples with different thiols - 3-MPA, 11-MUA and 16-MHDA as described in the experimental section. The PEM films were assembled at pH 9.0. In this test, only 0.5-bilayer and 2.5-bilayer film samples

were prepared. The spectra shown in **Fig. 5.12A** and **B** were obtained while the samples were in a pH 10 water bath. **Fig. 5.12C** plots the peak wavelengths obtained from the spectra on **A** & **B**. From this graph, we can tell that the peak wavelength changed significantly when using different thiols for the 0.5-bilayer samples. For the 2.5-bilayer samples, the variations were smaller. We believe that this difference may be due to thiol film being compressed more strongly by the Au spheres in films where more amines were present and electrostatic forces were correspondingly larger.

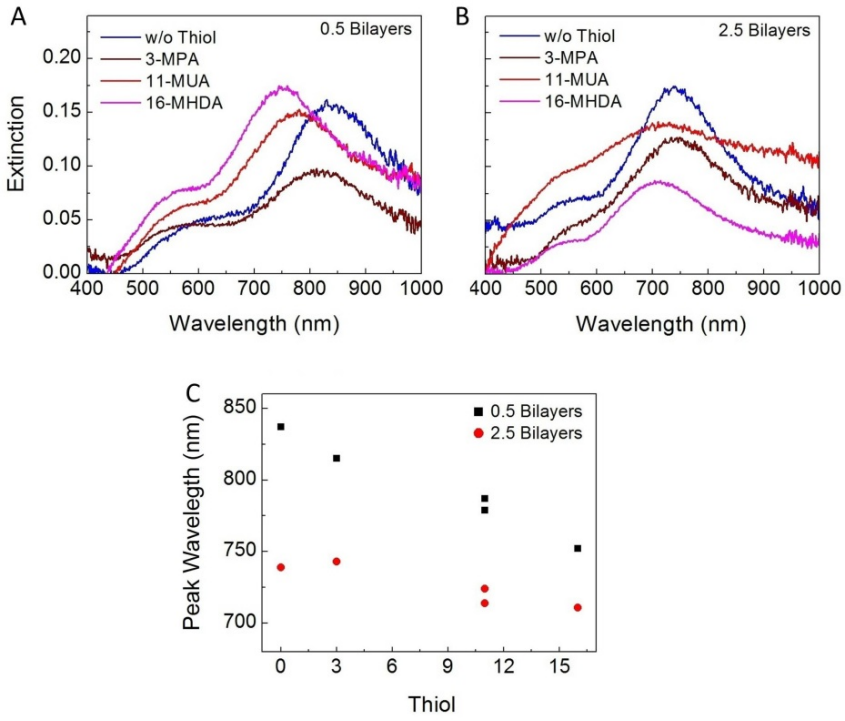

Fig. 5.12: Extinction spectra of the hybrid structure with different thiol layer under the PEM films. A) 0.5 bilayers; B) 2.5 bilayers. C) The peak wavelengths from the spectra on A) and B).

Our theoretical model makes it possible to extract the actual sphere-surface gap distances from the redshifts in **Fig. 5.12**. Subtracting the gap distances of samples without a thiol layer, we can get the monolayer thicknesses of each thiol we used as shown in **Tab. 5.1**. Bain and coworker's (Bain, et al. 1989) used an ellipsometer to measure the thicknesses of monolayers of *n*-alkanethiols, $CH3(CH2)_nSH$, on Au. The thiols we used (3 MPA, 11-MUA and 16-MHDA)

are associated with their data of n = 2, 10 and 15. The literature values listed in the table are the average values of their measurements. We obtain thicknesses of the thiol layers that are much smaller than those in the literature, although it is clear that thiols with longer carbon chains give rise to thicker films.

For each type of thiol, the monolayer thickness in 2.5-bilayer PEM film is smaller than that in the 0.5-bilayer film, which is consistent with the larger compressive forces in these films. As the number of bilayer increases, more amines are present in the film resulting in larger attractive force to the Au spheres. The pressure from the Au sphere can push aside the thiol molecules leading to a thinner thiol monolayer.

The idea that electrostatic forces on the spheres can compress and displace thiol layers on the Au surface is also supported by the data in **Fig. 5.11**. For films prepared at pH 8.5 or 9.0, there is a clear difference between the redshifts seen in samples with and without thiol layers. For films prepared at higher pH, this difference disappears, at least for the thicker films. Thicker films prepared at high pH should generate larger electrostatic forces, so this is precisely where we would expect to see a collapse and displacement of the thiol layer due to force between the sphere and the surface.

Tab. 5.1: Extracted monolayer thicknesses of different thiols and the values in the literature.

0.5-Bilayer PEM Film	No Thiol	3-MPA	11-MUA (1)	11-MUA (2)	16-MHDA
Peak Wavelength (nm)	837	815	779	787	752
Redshift from 548 nm	289	267	231	239	204
Calculated Gap Distance (nm)	0.59	0.68	0.87	0.81	1.06
Monolayer Thickness (nm)		0.09	0.28	0.22	0.47
2.5-Bilayer PEM Film					
Peak Wavelength (nm)	739	743	724	714	711
Redshift from 548 nm	191	195	176	166	163
Calculated Gap Distance (nm)	1.17	1.13	1.33	1.43	1.48
Monolayer Thickness (nm)		-0.04	0.16	0.26	0.31
Thickness from Bain *et al.*		0.27	1.22	1.22	1.90

5.5 Conclusion

We have shown large shift in LSPRs on Au NSs assembled above a Au surface using a pH responsive PEM film as a spacer layer. The shifts are sensitive to the pH of the environment, demonstrating that we are able to dynamically tune the distance between the spheres and the surface using the film. The actual distances between Au spheres and substrate are smaller than the unstrained film, due to a combination of a high degree of compliance of the film and strong electrostatic forces between the spheres and the film, which causes the spheres to become embedded in the films with a sphere-surface gap of no more than a new nm. The pressure from the spheres on the surface is sufficient that an underlying thiol layer can be displaced when a large amount of amines are present in the films.

Chapter 6 Two-Photon Excitation Fluorescence from Silver Nanotriangles

Noble metals can be fluorescent, due to the transitions between low lying energy bands in the metal. The fluorescence spectra from metal NPs are affected by the plasmon modes of the NPs. In this chapter, we study 2-photon excitation fluorescence (TPEF) from Ag nanotriangles fabricated by nanosphere lithography. We found that the TPEF signal was strong when the triangles' plasmon was resonant with the laser. In addition, at sufficiently high laser power, some triangles underwent a shape transformation into spheroidal particles which was accompanied by a drastic increase in the TPEF efficiency.

6.1 Introduction

Noble metal NPs have been widely studied in fluorescence microscopy because they exhibit fluorescence signal that is not subjected to photo-bleaching or phototoxicity, which is unlike traditional fluorescent dye molecules or quantum dots (Yorulmaz, et al. 2012). The plasmon resonance associated with NPs gives rise to large absorption and scattering cross-sections, which helps enhance the fluorescence signal by several orders of magnitude. There are a great number of reports of fluorescence from Au NPs, but Ag NP fluorescence is much less investigated. In this chapter, we study the TPEF of Ag triangles in an inverted Zeiss LSM 510 laser scanning confocal microscope.

6.2 Experimental Section

6.2.1 Sample preparation—nanosphere lithography

A suspension of 800 nm diameter carboxyl-terminated polystyrene (PS) spheres was concentrated by centrifugation to 20 % w/v prior to use. As illustrated in **Fig. 6.1**, the sphere suspension was deposited between a coverslip substrate (#1, 0.13–0.17 mm thickness, 40 × 22 mm, Fisher Sci., 12-545C) and a microscope slide, which was mounted on a vertical positioning stage with micron precision (Thorlabs, PT1A) at 22.5º from the surface. To ensure that the bottom edge of the microscope slide was parallel to the coverslip substrate, a goniometer stage (Thorlabs, GNL18) was also incorporated in the setup so that the edge could be leveled. The coverslip was cleaned in aqua regia solution for 10 mins, rinsed with deionized water, and dried with nitrogen gas. The coverslip was then attached to a computer controlled motion stage (Thorlabs, PT1-Z8 and TDC001) right under the angled microscope slide, allowing it to move at a controlled and constant velocity.

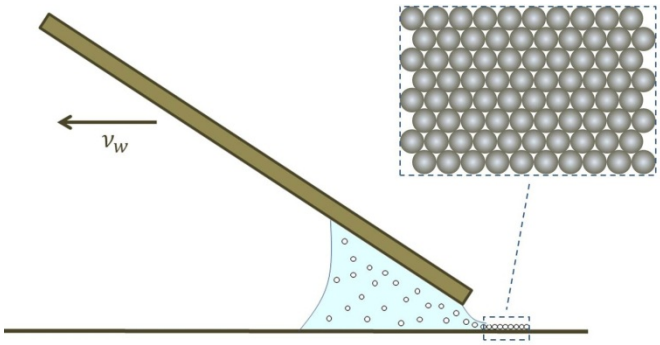

Fig. 6.1: Illustration of convective self-assembly of polystyrene spheres.

As shown by (Chen, et al. 2010), there exists a critical withdrawal speed of the angled slide at which a close-packed monolayer of PS spheres is formed on the substrate. Below this critical speed, bilayer or multilayer will form while beyond this speed, a submonolayer will form. The withdrawal speed was ~65 μm/s @ 22 % ambient humidity. If the humidity is higher, the withdrawal speed should be lower. Depending on the humidity in the room, the withdrawal speed was adjusted accordingly to get a large monolayer area of PS spheres, avoiding sub-monolayer

or multilayer deposition. The distance between the coverslip substrate and the microscope slide was kept at ~10 µm. As shown by Chen *et al.*, changing gap distance between 10 and 200 µm appeared to have no significant influence on the critical withdrawal speed. The self-assembled monolayer can serve as a deposition mask, allowing us to fabricate triangular nanoparticles of good quality.

The coverslip was then mounted on a sample holder of an evaporator (Thermonics VE-100). 140 nm of Ag (99.99 % purity, Kurt J. Lesker) was evaporated onto the coverslip at a rate of 0.5 Å/s. The thickness was monitored by a quartz crystal balance.

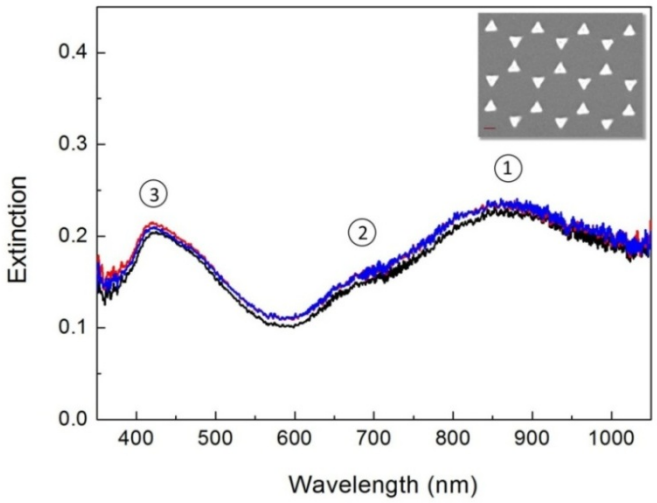

Fig. 6.2: Extinction spectra of the Ag triangles on a coverslip. The three spectra represented three different locations on the coverslip substrate. The inset is a SEM image of Ag triangles. The scale bar is 0.2 µm; the thickness of the Ag triangles is 140 nm.

After the evaporation, a piece of Scotch tape was taped onto the sample and then carefully peeled off, removing the PS spheres and leaving Ag triangles on the substrate as shown in the inset of **Fig. 6.2**. Extinction spectra were taken by a high-resolution miniature fiber optic spectrometer (Ocean Optics, HR2000) with a halogen light source (Ocean Optics, DH-2000). The collimated light was passed through a small aperture with diameter ~2 mm to ensure the measured spot contained, despite some slip dislocations, mostly Ag triangles. The extinction

spectra of the fabricated Ag triangles showed three resonance peaks at 870, 680, and 420 nm as shown in **Fig. 6.2**. Three spectra (black, red and blue) were recorded from three different regions on the sample substrate. The good agreement among the three spectra indicated the overall good quality of the Ag nanotriangles.

The dipole resonance (peak 1) of the Ag triangles can be shifted to longer or shorter wavelengths by changing the PS sphere size or the thickness of the Ag (Chen, et al. 2006). If we define the aspect-ratio of a triangle as the ratio between its edge length and thickness, then larger aspect-ratio leads to longer resonance wavelength.

6.2.2 Two-photon excitation fluorescence microscopy

The TPEF measurement was taken using an inverted Zeiss LSM 510 laser scanning microscope. The objective used was a Plan-Apochromat 63×/1.40 oil DIC M27 with working distance of 0.19 mm. The Ag triangle sample was placed upward so that the immersion oil contacted the back side of the sample leaving the triangles in air, as shown in **Fig. 6.3**. A reflection image of the Ag triangles was first obtained by using an argon laser at 477 nm (Max 30 mW) with 5 % transmission for the comparison with the fluorescence image.

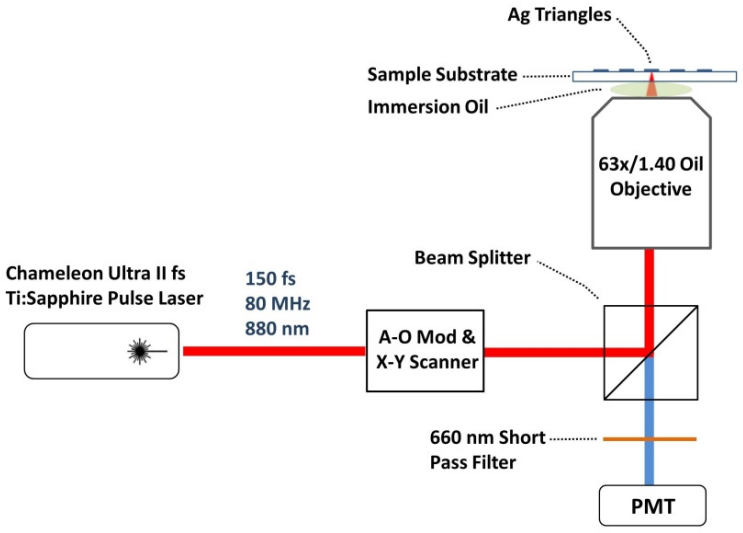

Fig. 6.3: Experimental setup of the TPEF measurement.

To take a TPEF image, 150 fs laser pulses at 880 nm from a Chameleon Ultra II ultrafast Ti:Sapphire laser (19.6 mW) go through an acousto-optical modulator and an x-y scanner (which permits fast scanning of the beam inside the sample) before being focused with an confocal microscope onto the sample. TPEF is collected in reflection mode and filtered out from the laser light with a beamsplitter and shortpass optical filter before being detected by a photo multiplier tube (PMT).

6.3 Results and Discussion

The TPEF image as shown in **Fig. 6.4** shows an array of spots, which are the fluorescence signals from individual Ag triangles. The inset **A** shows the reflection image from the same region obtained with the 477 nm line of an argon laser. In inset **A**, we can see the bright lines and spots associated with slip dislocations or defects of the sample. Because of their relatively large feature sizes, they are used as markers when comparing the fluorescence image to the SEM image of the same area shown in **Fig. 6.5**. While these features are bright in reflection, they appear dark in the TPEF image. This is because their plasmon resonances are not resonant with the laser, which supports the concept that the fluorescence signals from the triangles are plasmon-enhanced. The three orange arrows in the reflection, fluorescence and SEM images represent the same spot on the sample substrate.

The fluorescence image in **Fig. 6.4** was taken immediately after focusing. Besides the arrays of spots from individual triangles, several larger and brighter spots, which are numbered on the image, are also observed. The fluorescence signals at these spots are at least an order of magnitude higher than the signal from their neighbors. These bright spots in the fluorescence image correspond to the numbered spots in the SEM image (**Fig. 6.5**), where the triangles were partially or totally rounded up by the laser beam, even though the excitation light intensity was only 19.6 mW. As shown in **Fig. 6.2**, the resonance of the triangles overlaps well with the excitation laser wavelength at 880 nm. Therefore, the resonances of the triangle are efficiently excited leading to enormous near field intensity, which is high enough to melt the triangles into spherical nanoparticles. It is possible that the plasmon resonance of these spherical particles is in

the range of 440 nm, which corresponds to second harmonic of the excitation laser (880 nm). Therefore, we speculate that the larger and brighter spots in the image are due to plasmon excitation in those spherical particles.

The inset **B** in **Fig. 6.4** clearly shows fluorescence spot from individual triangles. The distances between triangles are below diffraction limit of the laser light, (880/2NA = 314 nm), but they can nonetheless be distinguished in the TPEF measurement.

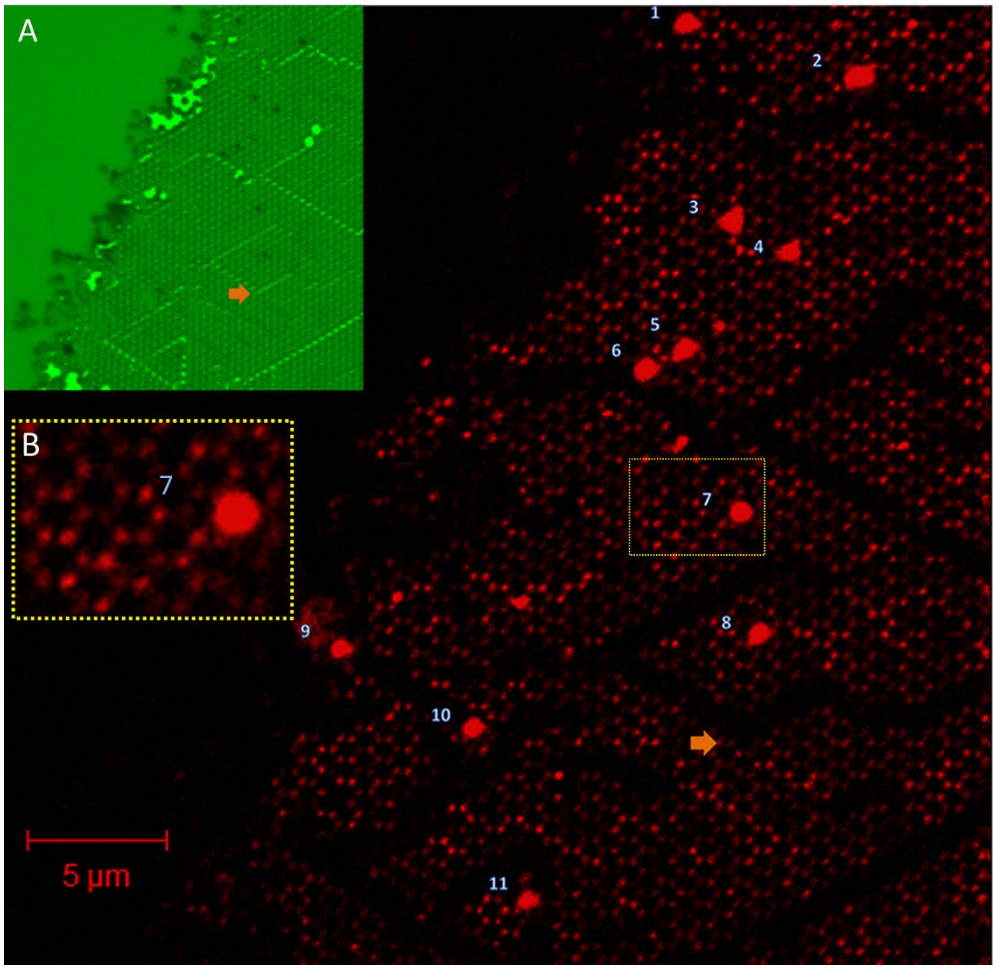

Fig. 6.4: 880 nm two-photon fluorescence image of Ag triangles. The insets are A) 477 nm reflection image and B) A close up of region 7.

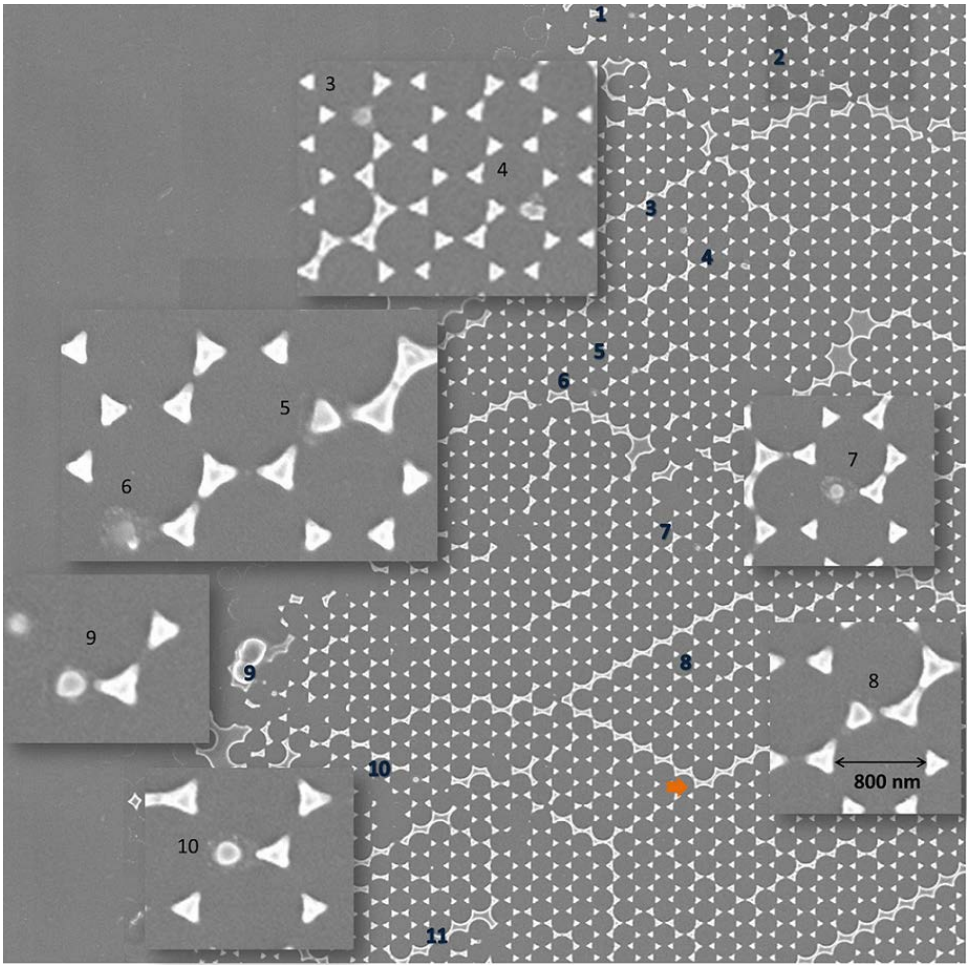

Fig. 6.5: SEM images of the areas appearing as bright spots in **Fig. 6.4**. The orange arrow indicates the same position as those in **Fig. 6.4**.

In addition, when the transmission intensity of the pump laser power was increased to 28 mW, some of the Ag triangles not only melted into spheres, but also jumped away as shown in **Fig. 6.6**. The kinetic energy of the jumping droplets comes from the surface energy difference between triangles and spheres (Boneberg, et al. 2008; Habenicht, et al. 2005; Stalmashonak, et al. 2009).

In a separate experiment, we placed the sample upside down with the immersion oil between the objective and the Ag triangles and kept everything else unchanged. We found that with low power scanning, no large bright spots were observed. Then we did a high power scan at 84 mW followed by a low power scan imaging at 22.4 mW to take a TPEF image. This caused large

bright spots to appear as before. The only difference between this experiment and the previous one is that the Ag nanotriangles are now submerged in immersion oil. This immersion oil serves as a more efficient heat sink than air. Therefore, higher laser powers are needed to reach the same temperature in the NPs and to induce the shape transformation that causes the bright spots to appear.

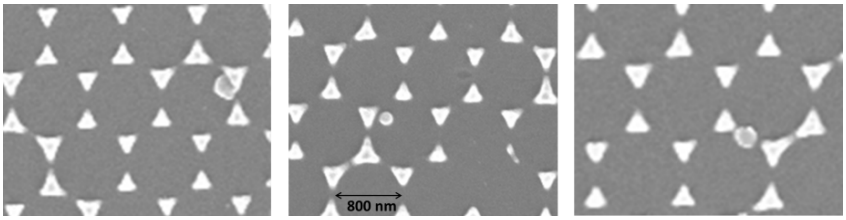

Fig. 6.6: SEM images of Ag NPs. (The newly-formed spheres have received enough energy from the melting process that they have jumped away from their original location)

Fluorescence spectroscopy

We also measured the spectra associated with the bright spots and the shape transformation. The initial spectra as shown in **Fig. 6.7** were taken by Dr. Brenden Magill using the same experimental condition as used in **Fig. 6.4** (28 mW @ 880 nm) with the fluorescence light being collected by an imaging spectrometer (Horiba, iHR320), which was connected to the laser scanning microscope. As expected, a bare glass slide (black) did not show any fluorescence. The fluorescence signal (blue) from the triangles is 2–3 times larger than that from a continuous Ag film (140 nm thickness). The enhancement is much greater than 3 times—scale with the amount of Ag on the surface due to the plasmon resonance of the triangles at 870 nm. In this figure, we also observed a 440 nm peak in the fluorescence spectrum of Ag triangles. This corresponds to second harmonic generation (SHG) of our 880 nm excitation wavelength. This peak is not or barely seen in the spectrum of the solid Ag film, which again demonstrates the plasmonic enhancement from the Ag triangles. It is possible that the two sharp peaks that flank the 440 nm peak are due to plasmon scattering from the SHG, which will be the subject of additional studies.

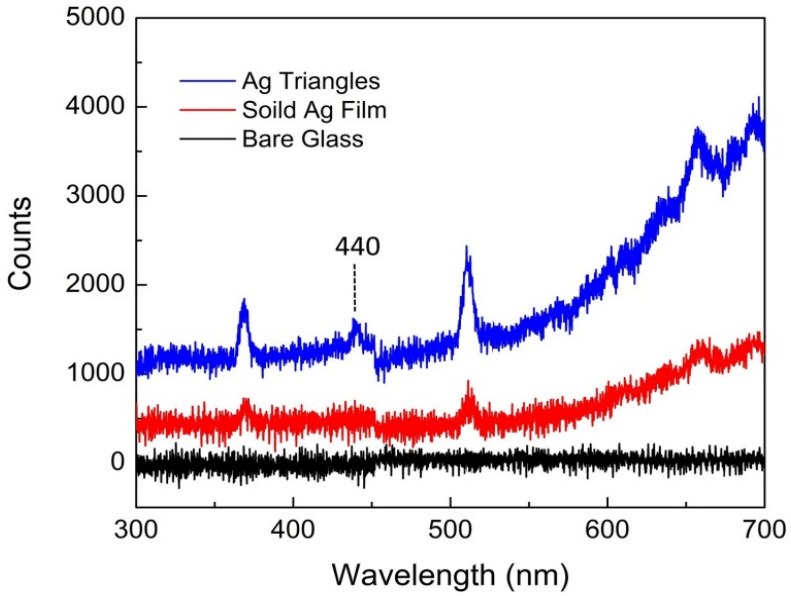

Fig. 6.7: Fluorescence spectra[iii] of a glass coverslip, a continuous Ag film and Ag triangles.

6.4 Conclusion

In this chapter, we studied the TPEF from Ag nanotriangles fabricated by nanosphere lithography. We observed bright spots in the images much brighter than those from individual nanotriangles even at the low excitation power of 19.6 mW. SEM images show that in these regions, some of the triangles underwent a shape transformation from triangles to spheres resulting in a signal at least an order higher than that of other regions. The shape transformation is ascribed to the plasmonic enhancement of the triangles, whose resonances overlap with the excitation laser wavelength. The larger fluorescence signal (brighter spots on the images) is possibly due to plasmon resonances associated with the spherical nanoparticles, which is in the 440 nm range. At higher excitation energy, some of the newly-formed spheres received enough energy from the melting process to jump away from their original locations.

[iii] The spectra were taken by Dr. Brenden Magill using Horiba iHR320 Imaging Spectrometer.

Bibliography

Adamczyk, Z.

2000 Kinetics of diffusion-controlled adsorption of colloid particles and proteins. Journal of Colloid and Interface Science 229(2):477-489.

Adamczyk, Z., et al.

2004 Irreversible adsorption of particles at random-site surfaces. Journal of Chemical Physics 120(23):11155-11162.

Adamczyk, Z., and L. Szyk

2000 Kinetics of irreversible adsorption of latex particles under diffusion-controlled transport. Langmuir 16(13):5730-5737.

Adamczyk, Zbigniew

2006 Particles at Interfaces: Interactions, Deposition, Structure. London: Academic Press.

Aherne, Damian, et al.

2008 Optical Properties and Growth Aspects of Silver Nanoprisms Produced by a Highly Reproducible and Rapid Synthesis at Room Temperature. Advanced Functional Materials 18(14):2005-2016.

Ahmed, Marya, and Ravin Narain

2010 Rapid Synthesis of Gold Nanorods Using a One-Step Photochemical Strategy. Langmuir 26(23):18392-18399.

Aizpurua, J., et al.

2003 Optical Properties of Gold Nanorings. Physical Review Letters 90(Copyright (C) 2009 The American Physical Society):057401.

Aravind, P. K., and Horia Metiu

1983 The effects of the interaction between resonances in the electromagnetic response of a sphere-plane structure; applications to surface enhanced spectroscopy. Surface Science 124(2–3):506-528.

Auguste, Debra T., et al.

2008 Surface Rheology of Hydrophobically Modified PEG Polymers Associating with a Phospholipid Monolayer at the Air−Water Interface. Langmuir 24(8):4056-4064.

Bain, Colin D., et al.

1989 Formation of monolayer films by the spontaneous assembly of organic thiols from solution onto gold. Journal of the American Chemical Society 111(1):321-335.

Beversluis, Michael R., Alexandre Bouhelier, and Lukas Novotny

2003 Continuum generation from single gold nanostructures through near-field mediated intraband transitions. Physical Review B 68(11):115433.

Bhattacharjee, S., M. Elimelech, and M. Borkovec

1998 DLVO interaction between colloidal particles: Beyond Derjaguin's approximation. Croatica Chemica Acta 71(4):883-903.

Bobbert, P. A., and J. Vlieger

1986 Light scattering by a sphere on a substrate. Physica A: Statistical Mechanics and its Applications 137(1–2):209-242.

Bohren, Craig F., and Donald R. Huffman

2007 Rayleigh-Gans Theory. *In* Absorption and Scattering of Light by Small Particles. Pp. 158-165: Wiley-VCH Verlag GmbH.

Boneberg, J., et al.

2008 Jumping nanodroplets: a new route towards metallic nano-particles. Applied Physics A: Materials Science & Processing 93(2):415-419.

Bönnemann, H., et al.

1996 Nanoscale colloidal metals and alloys stabilized by solvents and surfactants Preparation and use as catalyst precursors. Journal of Organometallic Chemistry 520(1-2):143-162.

Bouhelier, A., et al.

2005 Surface Plasmon Characteristics of Tunable Photoluminescence in Single Gold Nanorods. Physical Review Letters 95(26):267405.

Brioude, A., X. C. Jiang, and M. P. Pileni

2005 Optical Properties of Gold Nanorods: DDA Simulations Supported by Experiments. The Journal of Physical Chemistry B 109(27):13138-13142.

Burgin, Julien, Mingzhao Liu, and Philippe Guyot-Sionnest

2008 Dielectric Sensing with Supported Gold Bipyramids, 2008, pp. MThD4. Optical Society of America.

Busbee, B. D., S. O. Obare, and C. J. Murphy

2003 An Improved Synthesis of High-Aspect-Ratio Gold Nanorods. Advanced Materials 15(5):414-416.

Camargo, Pedro H. C., et al.

2010 Measuring the SERS enhancement factors of dimers with different structures constructed from silver nanocubes. Chemical Physics Letters 484(4–6):304-308.

Caruso, F.

2001 Nanoengineering of Particle Surfaces. Advanced Materials 13(1):11-22.

Caruso, Frank

2000 Hollow Capsule Processing through Colloidal Templating and Self-Assembly. Chemistry - A European Journal 6(3):413-419.

Caruso, Frank, Edwin Donath, and Helmuth Mohwald

1998 Influence of Polyelectrolyte Multilayer Coatings on Forster Resonance Energy Transfer between 6-Carboxyfluorescein and Rhodamine B-Labeled Particles in Aqueous Solution. The Journal of Physical Chemistry B 102(11):2011-2016.

Caruso, Frank, et al.

1999a Investigation of Electrostatic Interactions in Polyelectrolyte Multilayer Films: Binding of Anionic Fluorescent Probes to Layers Assembled onto Colloids. Macromolecules 32(7):2317-2328.

Caruso, Frank, Corinna Schuler, and Dirk G. Kurth

1999b Core−Shell Particles and Hollow Shells Containing Metallo-Supramolecular Components. Chemistry of Materials 11(11):3394-3399.

Chen, Huanjun, et al.

2009 Shape-Dependent Refractive Index Sensitivities of Gold Nanocrystals with the Same Plasmon Resonance Wavelength. The Journal of Physical Chemistry C 113(41):17691-17697.

Chen, J., et al.

2005 Gold Nanocages: Engineering Their Structure for Biomedical Applications. Advanced Materials 17(18):2255-2261.

Chen, Kai, et al.

2006 Plasmon-Enhanced Second-Harmonic Generation from Ionic Self-Assembled Multilayer Films. Nano Letters 7(2):254-258.

Chen, Kai, and Hans Robinson

2011 Robust dithiocarbamate-anchored amine functionalization of Au nanoparticles. Journal of Nanoparticle Research 13(2):751-761.

Chen, Kai, et al.

2010 Restricted meniscus convective self-assembly. Journal of Colloid and Interface Science 344(2):315-320.

Cheng, Yu, et al.

2008 Highly Efficient Drug Delivery with Gold Nanoparticle Vectors for in Vivo Photodynamic Therapy of Cancer. Journal of the American Chemical Society 130(32):10643-10647.

Ciracì, C., et al.

2012 Probing the Ultimate Limits of Plasmonic Enhancement. Science 337(6098):1072-1074.

Crooks, Richard M., et al.

2000 Dendrimer-Encapsulated Metal Nanoparticles: Synthesis, Characterization, and Applications to Catalysis. Accounts of Chemical Research 34(3):181-190.

Decher, G., J. D. Hong, and J. Schmitt

1992 Buildup of ultrathin multilayer films by a self-assembly process: III. Consecutively alternating adsorption of anionic and cationic polyelectrolytes on charged surfaces. Thin Solid Films 210-211(Part 2):831-835.

Decher, Gero

1997 Fuzzy Nanoassemblies: Toward Layered Polymeric Multicomposites. Science 277(5330):1232-1237.

Drachev, Vladimir P., et al.

2004 Quantum size effect in two-photon excited luminescence from silver nanoparticles. Physical Review B 69(3):035318.

Driskell, Jeremy D., Robert J. Lipert, and Marc D. Porter

2006 Labeled Gold Nanoparticles Immobilized at Smooth Metallic Substrates: Systematic Investigation of Surface Plasmon Resonance and Surface-Enhanced Raman Scattering. The Journal of Physical Chemistry B 110(35):17444-17451.

Dulkeith, E., et al.

2004 Plasmon emission in photoexcited gold nanoparticles. Physical Review B 70(20):205424.

Durr, Nicholas J., et al.

2007 Two-Photon Luminescence Imaging of Cancer Cells Using Molecularly Targeted Gold Nanorods. Nano Letters 7(4):941-945.

Ebbesen, T. W., et al.

1998 Extraordinary optical transmission through sub-wavelength hole arrays. Nature 391(6668):667-669.

Esumi, Kunio, Keiichi Matsuhisa, and Kanjiro Torigoe

1995 Preparation of Rodlike Gold Particles by UV Irradiation Using Cationic Micelles as a Template. Langmuir 11(9):3285-3287.

Evans, J. W.

1993 RANDOM AND COOPERATIVE SEQUENTIAL ADSORPTION. Reviews of Modern Physics 65(4):1281-1329.

Fang, Ying, et al.

2012 Plasmon Emission Quantum Yield of Single Gold Nanorods as a Function of Aspect Ratio. ACS Nano.

Faraday, Michael

1857 The Bakerian Lecture: Experimental Relations of Gold (and Other Metals) to Light. Philosophical Transactions of the Royal Society of London 147:145-181.

Frens, G.

1973 CONTROLLED NUCLEATION FOR REGULATION OF PARTICLE-SIZE IN MONODISPERSE GOLD SUSPENSIONS. Nature-Physical Science 241(105):20-22.

Fucile, E., et al.

1997 Optical properties of a sphere in the vicinity of a plane surface. J. Opt. Soc. Am. A 14(7):1505-1514.

Gai, Pratibha L., and Mark A. Harmer

2002 Surface Atomic Defect Structures and Growth of Gold Nanorods. Nano Letters 2(7):771-774.

Gao, Bo, Gaurav Arya, and Andrea R. Tao

2012 Self-orienting nanocubes for the assembly of plasmonic nanojunctions. Nat Nano 7(7):433-437.

Gao, Junpeng, et al.

2004 Formation and Photoluminescence of Silver Nanoparticles Stabilized by a Two-Armed Polymer with a Crown Ether Core. Langmuir 20(22):9775-9779.

Gauderon, R., P. B. Lukins, and C. J. R. Sheppard

2001 Optimization of second-harmonic generation microscopy. Micron 32(7):691-700.

Goldys, Ewa M., and Mushtaq A. Sobhan

2012 Fluorescence of Colloidal Gold Nanoparticles is Controlled by the Surface Adsorbate. Advanced Functional Materials 22(9):1906-1913.

Gole, Anand, and Catherine J. Murphy

2005 Polyelectrolyte-Coated Gold Nanorods: Synthesis, Characterization and Immobilization. Chemistry of Materials 17(6):1325-1330.

Grabar, K. C., et al.

1996 Kinetic control of interparticle spacing in Au colloid-based surfaces: Rational nanometer-scale architecture. Journal of the American Chemical Society 118(5):1148-1153.

Gu, Y. G., and D. Q. Li

2002 Deposition of spherical particles onto cylindrical solid surfaces II. Experimental studies. Journal of Colloid and Interface Science 248(2):329-339.

Guerrini, Luca, et al.

2009 Self-assembly of a dithiocarbamate calix[4]arene on Ag nanoparticles and its application in the fabrication of surface-enhanced Raman scattering based nanosensors. Physical Chemistry Chemical Physics 11(11):1787-1793.

Habenicht, A., et al.

2005 Jumping Nanodroplets. Science 309(5743):2043-2045.

Hao, Encai, et al.

2004 Synthesis and Optical Properties of “Branched” Gold Nanocrystals. Nano Letters 4(2):327-330.

Harding, S. E.

1995 ON THE HYDRODYNAMIC ANALYSIS OF MACROMOLECULAR CONFORMATION. Biophysical Chemistry 55(1-2):69-93.

Haruta, Masatake

1997 Size- and support-dependency in the catalysis of gold. Catalysis Today 36(1):153-166.

Harutyunyan, Hayk, et al.

2010 Nonlinear Dark-Field Microscopy. Nano Letters 10(12):5076-5079.

He, Guang S., et al.

2010 Scattering and Absorption Cross-Section Spectral Measurements of Gold Nanorods in Water. The Journal of Physical Chemistry C 114(7):2853-2860.

Hiller, Jeri'Ann, and Michael F. Rubner

2003 Reversible Molecular Memory and pH-Switchable Swelling Transitions in Polyelectrolyte Multilayers. Macromolecules 36(11):4078-4083.

Huang, Xiaohua, Svetlana Neretina, and Mostafa A. El-Sayed

2009 Gold Nanorods: From Synthesis and Properties to Biological and Biomedical Applications. Advanced Materials 21(48):4880-4910.

Huff, Terry B., et al.

2007 Controlling the Cellular Uptake of Gold Nanorods. Langmuir 23(4):1596-1599.

Hvolbæk, Britt, et al.

2007 Catalytic activity of Au nanoparticles. Nano Today 2(4):14-18.

Im, S. H., et al.

2005 Large-Scale Synthesis of Silver Nanocubes: The Role of HCl in Promoting Cube Perfection and Monodispersity. Angewandte Chemie International Edition 44(14):2154-2157.

Imae, Toyoko, Ritsu Kamiya, and Shoichi Ikeda

1985 Formation of spherical and rod-like micelles of cetyltrimethylammonium bromide in aqueous NaBr solutions. Journal of Colloid and Interface Science 108(1):215-225.

Imura, Kohei, Tetsuhiko Nagahara, and Hiromi Okamoto

2004 Plasmon Mode Imaging of Single Gold Nanorods. Journal of the American Chemical Society 126(40):12730-12731.

—

2005 Near-Field Two-Photon-Induced Photoluminescence from Single Gold Nanorods and Imaging of Plasmon Modes. The Journal of Physical Chemistry B 109(27):13214-13220.

Imura, Kohei, and Hiromi Okamoto

2009 Properties of Photoluminescence from Single Gold Nanorods Induced by Near-Field Two-Photon Excitation†. The Journal of Physical Chemistry C 113(27):11756-11759.

Itano, Koji, Jeeyoung Choi, and Michael F. Rubner

2005 Mechanism of the pH-Induced Discontinuous Swelling/Deswelling Transitions of Poly(allylamine hydrochloride)-Containing Polyelectrolyte Multilayer Films. Macromolecules 38(8):3450-3460.

Jain, Prashant K., Ivan H. El-Sayed, and Mostafa A. El-Sayed

2007 Au nanoparticles target cancer. Nano Today 2(1):18-29.

Jain, Prashant K., et al.

2008 Noble Metals on the Nanoscale: Optical and Photothermal Properties and Some Applications in Imaging, Sensing, Biology, and Medicine. Accounts of Chemical Research 41(12):1578-1586.

Jain, Prashant K., et al.

2006 Calculated Absorption and Scattering Properties of Gold Nanoparticles of Different Size, Shape, and Composition: Applications in Biological Imaging and Biomedicine. The Journal of Physical Chemistry B 110(14):7238-7248.

Jana, Nikhil R., Latha Gearheart, and Catherine J. Murphy

2001a Seeding Growth for Size Control of 5−40 nm Diameter Gold Nanoparticles. Langmuir 17(22):6782-6786.

—

2001b Wet Chemical Synthesis of High Aspect Ratio Cylindrical Gold Nanorods. The Journal of Physical Chemistry B 105(19):4065-4067.

Jin, Rongchao, et al.

2001 Photoinduced Conversion of Silver Nanospheres to Nanoprisms. Science 294(5548):1901-1903.

Jin, Rongchao, et al.

2003 Controlling anisotropic nanoparticle growth through plasmon excitation. Nature 425(6957):487-490.

Johnson, B. R.

1996 Calculation of light scattering from a spherical particle on a surface by the multipole expansion method. J. Opt. Soc. Am. A 13(2):326-337.

Johnson, P. B., and R. W. Christy

1972 Optical Constants of the Noble Metals. Physical Review B 6(12):4370-4379.

Kelly, K. Lance, et al.

2002 The Optical Properties of Metal Nanoparticles: The Influence of Size, Shape, and Dielectric Environment. The Journal of Physical Chemistry B 107(3):668-677.

Kou, Xiaoshan, et al.

2007 Growth of Gold Bipyramids with Improved Yield and Their Curvature-Directed Oxidation. Small 3(12):2103-2113.

LaGrow, Alec P., et al.

2011 Synthesis, Alignment, and Magnetic Properties of Monodisperse Nickel Nanocubes. Journal of the American Chemical Society 134(2):855-858.

Le, F., et al.

2005 Plasmons in the Metallic Nanoparticle−Film System as a Tunable Impurity Problem. Nano Letters 5(10):2009-2013.

Lee, Seunghyun, Kathryn M. Mayer, and Jason H. Hafner

2009 Improved Localized Surface Plasmon Resonance Immunoassay with Gold Bipyramid Substrates. Analytical Chemistry 81(11):4450-4455.

Lévêque, Gaëtan, and Olivier J. F. Martin

2006a Tunable composite nanoparticle for plasmonics. Opt. Lett. 31(18):2750-2752.

Lévêque, Gäetan, and Olivier J. F. Martin

2006b Optical interactions in a plasmonic particle coupled to a metallic film. Opt. Express 14(21):9971-9981.

Li, Cuncheng, et al.

2007 High-Yield Synthesis of Single-Crystalline Gold Nano-octahedra. Angewandte Chemie International Edition 46(18):3264-3268.

Link, Stephan, and Mostafa A. El-Sayed

1999 Spectral Properties and Relaxation Dynamics of Surface Plasmon Electronic Oscillations in Gold and Silver Nanodots and Nanorods. The Journal of Physical Chemistry B 103(40):8410-8426.

Liu, and Philippe Guyot-Sionnest

2005 Mechanism of Silver(I)-Assisted Growth of Gold Nanorods and Bipyramids. The Journal of Physical Chemistry B 109(47):22192-22200.

Liu, J., et al.

2005 Fabrication of Hollow Metal ldquoNanocapsrdquo and Their Red-Shifted Optical Absorption Spectra. Advanced Materials 17(10):1276-1281.

Liz-Marzán, Luis M.

2004 Nanometals: Formation and color. Materials Today 7(2):26-31.

Lu, Xianmao, et al.

2009 Chemical Synthesis of Novel Plasmonic Nanoparticles. Annual Review of Physical Chemistry 60(1):167-192.

Maillard, Mathieu, Pinray Huang, and Louis Brus

2003 Silver Nanodisk Growth by Surface Plasmon Enhanced Photoreduction of Adsorbed [Ag+]. Nano Letters 3(11):1611-1615.

Masatake, Haruta

1997 Size- and support-dependency in the catalysis of gold. Catalysis Today 36(1):153-166.

Métraux, G. S., and C. A. Mirkin

2005 Rapid Thermal Synthesis of Silver Nanoprisms with Chemically Tailorable Thickness. Advanced Materials 17(4):412-415.

Mie, Gustav

1908 Beiträge zur Optik trüber Medien, speziell kolloidaler Metallösungen. Annalen der Physik 330(3):377-445.

Millstone, Jill E., et al.

2009 Colloidal Gold and Silver Triangular Nanoprisms. Small 5(6):646-664.

Ming, Tian, et al.

2011 Plasmon-Controlled Fluorescence: Beyond the Intensity Enhancement. The Journal of Physical Chemistry Letters 3(2):191-202.

Mock, Jack J., et al.

2008 Distance-Dependent Plasmon Resonant Coupling between a Gold Nanoparticle and Gold Film. Nano Letters 8(8):2245-2252.

Mock, Jack J., et al.

2012 Probing Dynamically Tunable Localized Surface Plasmon Resonances of Film-Coupled Nanoparticles by Evanescent Wave Excitation. Nano Letters.

Mock, Jack J., David R. Smith, and Sheldon Schultz

2003 Local Refractive Index Dependence of Plasmon Resonance Spectra from Individual Nanoparticles. Nano Letters 3(4):485-491.

Mohamed, Mona B., et al.

2000 The `lightning' gold nanorods: fluorescence enhancement of over a million compared to the gold metal. Chemical Physics Letters 317(6):517-523.

Morf, Peter, et al.

2005 Dithiocarbamates: Functional and Versatile Linkers for the Formation of Self-Assembled Monolayers. Langmuir 22(2):658-663.

Mubeen, Syed, et al.

2012 Plasmonic Properties of Gold Nanoparticles Separated from a Gold Mirror by an Ultrathin Oxide. Nano Letters.

Murphy, Catherine J., et al.

2005 Anisotropic Metal Nanoparticles: Synthesis, Assembly, and Optical Applications. The Journal of Physical Chemistry B 109(29):13857-13870.

Nagai, Yusuke, Tatsuya Yamaguchi, and Kotaro Kajikawa

2012 Angular-Resolved Polarized Surface Enhanced Raman Spectroscopy. The Journal of Physical Chemistry C 116(17):9716-9723.

Nathan, C. Lindquist, et al.

2012 Engineering metallic nanostructures for plasmonics and nanophotonics. Reports on Progress in Physics 75(3):036501.

Ni, Weihai, et al.

2008 Tailoring Longitudinal Surface Plasmon Wavelengths, Scattering and Absorption Cross Sections of Gold Nanorods. ACS Nano 2(4):677-686.

Nikoobakht, Babak, and Mostafa A. El-Sayed

2003 Preparation and Growth Mechanism of Gold Nanorods (NRs) Using Seed-Mediated Growth Method. Chemistry of Materials 15(10):1957-1962.

Nordlander, P., and E. Prodan

2004 Plasmon Hybridization in Nanoparticles near Metallic Surfaces. Nano Letters 4(11):2209-2213.

Nusz, G. J., et al.

2009 Rational Selection of Gold Nanorod Geometry for Label-Free Plasmonic Biosensors. ACS Nano 3(4):795-806.

Okamoto, Takayuki, and Ichirou Yamaguchi

2003 Optical Absorption Study of the Surface Plasmon Resonance in Gold Nanoparticles Immobilized onto a Gold Substrate by Self-Assembly Technique. The Journal of Physical Chemistry B 107(38):10321-10324.

Oldenburg, S. J., et al.

1998 Nanoengineering of optical resonances. Chemical Physics Letters 288(2-4):243-247.

Paciotti, Giulio F., et al.

2004 Colloidal Gold: A Novel Nanoparticle Vector for Tumor Directed Drug Delivery. Drug Delivery 11(3):169-183.

Paolo, Biagioni, Huang Jer-Shing, and Hecht Bert

2012 Nanoantennas for visible and infrared radiation. Reports on Progress in Physics 75(2):024402.

Park, Jaesook, et al.

2010 Intra-organ biodistribution of gold nanoparticles using intrinsic two-photon-induced photoluminescence. Lasers in Surgery and Medicine 42(7):630-639.

Park, K., S. R. Simmons, and R. M. Albrecht

1987 SURFACE CHARACTERIZATION OF BIOMATERIALS BY IMMUNOGOLD STAINING - QUANTITATIVE-ANALYSIS. Scanning Microscopy 1(1):339-350.

Perrault, Steven D., and Warren C. W. Chan

2009 Synthesis and Surface Modification of Highly Monodispersed, Spherical Gold Nanoparticles of 50−200 nm. Journal of the American Chemical Society 131(47):17042-17043.

Petsi, A. J., A. N. Kalarakis, and V. N. Burganos

2010 Deposition of Brownian particles during evaporation of two-dimensional sessile droplets. Chemical Engineering Science 65(10):2978-2989.

Sau, Tapan K., and Catherine J. Murphy

2004 Seeded High Yield Synthesis of Short Au Nanorods in Aqueous Solution. Langmuir 20(15):6414-6420.

Schertz, Florian, et al.

2012 Near Field of Strongly Coupled Plasmons: Uncovering Dark Modes. Nano Letters.

Shao, Yunliang, et al.

2010 Optical Fiber LSPR Biosensor Prepared by Gold Nanoparticle Assembly on Polyelectrolyte Multilayer. Sensors 10(4):3585-3596.

Shoup, D., and A. Szabo

1982 ROLE OF DIFFUSION IN LIGAND-BINDING TO MACROMOLECULES AND CELL-BOUND RECEPTORS. Biophysical Journal 40(1):33-39.

Skrabalak, Sara E., et al.

2008 On the Polyol Synthesis of Silver Nanostructures: Glycolaldehyde as a Reducing Agent. Nano Letters 8(7):2077-2081.

So, P. T. C., et al.

2000 Two-photon excitation fluorescence microscopy. Annual Review of Biomedical Engineering 2:399-429.

Stalmashonak, Andrei, et al.

2009 Effects of Temperature on Laser-Induced Shape Modification of Silver Nanoparticles Embedded in Glass. The Journal of Physical Chemistry C 113(28):12028-12032.

Sun, Y. G., and Y. N. Xia

2002 Shape-controlled synthesis of gold and silver nanoparticles. Science 298(5601):2176-2179.

Sun, Yugang, et al.

2002 Crystalline Silver Nanowires by Soft Solution Processing. Nano Letters 2(2):165-168.

Sun, Yugang, Brian Mayers, and Younan Xia

2003 Transformation of Silver Nanospheres into Nanobelts and Triangular Nanoplates through a Thermal Process. Nano Letters 3(5):675-679.

Taguchi, Atsushi, et al.

2008 Oxygen-assisted shape control in polyol synthesis of silver nanocrystals. Chemical Physics Letters 462(1–3):92-95.

Talbot, J., et al.

2000 From car parking to protein adsorption: an overview of sequential adsorption processes. Colloids and Surfaces a-Physicochemical and Engineering Aspects 165(1-3):287-324.

Tanchak, Oleh M., and Christopher J. Barrett

2004 Swelling Dynamics of Multilayer Films of Weak Polyelectrolytes. Chemistry of Materials 16(14):2734-2739.

Tao, Andrea, et al.

2003 Langmuir−Blodgett Silver Nanowire Monolayers for Molecular Sensing Using Surface-Enhanced Raman Spectroscopy. Nano Letters 3(9):1229-1233.

Tao, Andrea R., Susan Habas, and Peidong Yang

2008 Shape Control of Colloidal Metal Nanocrystals. Small 4(3):310-325.

Tao, Andrea, Prasert Sinsermsuksakul, and Peidong Yang

2006 Polyhedral Silver Nanocrystals with Distinct Scattering Signatures. Angewandte Chemie International Edition 45(28):4597-4601.

Tcherniak, A., et al.

2010 Probing a Century Old Prediction One Plasmonic Particle at a Time. Nano Letters 10(4):1398-1404.

Tong, L., et al.

2007 Gold Nanorods Mediate Tumor Cell Death by Compromising Membrane Integrity. Advanced Materials 19(20):3136-3141.

Tong, M. C., et al.

2006 Dithiocarbamate-capped silver nanoparticles. Journal of Physical Chemistry B 110(39):19238-19242.

Toshima, N., and T. Yonezawa

1998 Bimetallic nanoparticles - novel materials for chemical and physical applications. New Journal of Chemistry 22(11):1179-1201.

Turkevich, John, Peter Cooper Stevenson, and James Hillier

1951 A study of the nucleation and growth processes in the synthesis of colloidal gold. Discussions of the Faraday Society 11:55-75.

Turner, Mark, et al.

2008 Selective oxidation with dioxygen by gold nanoparticle catalysts derived from 55-atom clusters. Nature 454(7207):981-983.

van der Zande, Bianca M. I., et al.

1999 Colloidal Dispersions of Gold Rods: Synthesis and Optical Properties. Langmuir 16(2):451-458.

Wagner, J. K., et al.

2006 A nutrient uptake role for bacterial cell envelope extensions. Proceedings of the National Academy of Sciences of the United States of America 103(31):11772-11777.

Wang, Hui, et al.

2006 Nanorice: A Hybrid Plasmonic Nanostructure. Nano Letters 6(4):827-832.

Wang, Z. L., et al.

1999 Crystallographic facets and shapes of gold nanorods of different aspect ratios. Surface Science 440(1–2):L809-L814.

Ward, Jonathan M., et al.

2006 Heat-and-pull rig for fiber taper fabrication. Review of Scientific Instruments 77(8):083105-5.

Weare, Walter W., et al.

2000 Improved Synthesis of Small (dCORE $\approx$ 1.5 nm) Phosphine-Stabilized Gold Nanoparticles. Journal of the American Chemical Society 122(51):12890-12891.

Wiley, Benjamin J., et al.

2006 Maneuvering the Surface Plasmon Resonance of Silver Nanostructures through Shape-Controlled Synthesis. The Journal of Physical Chemistry B 110(32):15666-15675.

Wiley, Benjamin, Yugang Sun, and Younan Xia

2007 Synthesis of Silver Nanostructures with Controlled Shapes and Properties. Accounts of Chemical Research 40(10):1067-1076.

Wind, M. M., J. Vlieger, and D. Bedeaux

1987 The polarizability of a truncated sphere on a substrate I. Physica A: Statistical and Theoretical Physics 141(1):33-57.

Xiong, Yujie, et al.

2006 Poly(vinyl pyrrolidone): A Dual Functional Reductant and Stabilizer for the Facile Synthesis of Noble Metal Nanoplates in Aqueous Solutions. Langmuir 22(20):8563-8570.

Xue, Can, et al.

2008 Mechanistic Study of Photomediated Triangular Silver Nanoprism Growth. Journal of the American Chemical Society 130(26):8337-8344.

Xue, Can, and Chad A Mirkin

2007 pH-Switchable Silver Nanoprism Growth Pathways. Angewandte Chemie International Edition 46(12):2036-2038.

Xue, Shicheng, et al.

2007 Theoretical, Numerical, and Experimental Analysis of Optical Fiber Tapering. J. Lightwave Technol. 25(5):1169-1176.

Yang, L., and K. J. Vahala

2003 Gain functionalization of silica microresonators. Optics Letters 28(8):592-594.

Yang, Wen-Hui, George C. Schatz, and Richard P. Van Duyne

1995 Discrete dipole approximation for calculating extinction and Raman intensities for small particles with arbitrary shapes. The Journal of chemical physics 103(3):869-875.

Yeshchenko, Oleg A., et al.

2009 Size-dependent surface-plasmon-enhanced photoluminescence from silver nanoparticles embedded in silica. Physical Review B 79(23):235438.

Yorulmaz, Mustafa, et al.

2012 Luminescence Quantum Yield of Single Gold Nanorods. Nano Letters 12(8):4385-4391.

Yu, et al.

1997 Gold Nanorods: Electrochemical Synthesis and Optical Properties. The Journal of Physical Chemistry B 101(34):6661-6664.

Yuan, Chao, et al.

2011 Single clusters of self-assembled silver nanoparticles for surface-enhanced Raman scattering sensing of a dithiocarbamate fungicide. Journal of Materials Chemistry 21(40):16264-16270.

Zeng, Jie, et al.

2010 Controlling the Shapes of Silver Nanocrystals with Different Capping Agents. Journal of the American Chemical Society 132(25):8552-8553.

Zeng, S. W., et al.

2011 A Review on Functionalized Gold Nanoparticles for Biosensing Applications. Plasmonics 6(3):491-506.

Zhang, Jian, Mark R. Langille, and Chad A. Mirkin

2010a Photomediated Synthesis of Silver Triangular Bipyramids and Prisms: The Effect of pH and BSPP. Journal of the American Chemical Society 132(35):12502-12510.

Zhang, Jian, et al.

2009a Plasmon-Mediated Synthesis of Silver Triangular Bipyramids. Angewandte Chemie International Edition 48(42):7787-7791.

Zhang, Jing, and Nicholas A. Peppas

1999 Synthesis and Characterization of pH- and Temperature-Sensitive Poly(methacrylic acid)/Poly(N-isopropylacrylamide) Interpenetrating Polymeric Networks. Macromolecules 33(1):102-107.

Zhang, Qiang, et al.

2010b Seed-Mediated Synthesis of Ag Nanocubes with Controllable Edge Lengths in the Range of 30−200 nm and Comparison of Their Optical Properties. Journal of the American Chemical Society 132(32):11372-11378.

Zhang, Qiao, et al.

2009b Reconstruction of Silver Nanoplates by UV Irradiation: Tailored Optical Properties and Enhanced Stability13. Angewandte Chemie 121(19):3568-3571.

Zhao, Jing, et al.

2008 Methods for Describing the Electromagnetic Properties of Silver and Gold Nanoparticles. Accounts of Chemical Research 41(12):1710-1720.

Zhao, Jing, et al.

2006 Localized surface plasmon resonance biosensors. Nanomedicine 1(2):219-228.

Zhao, Yan, et al.

2009 Dithiocarbamate-Coated SERS Substrates: Sensitivity Gain by Partial Surface Passivation†. Langmuir.

Zhao, Yan, et al.

2005 Dithiocarbamate Assembly on Gold. Journal of the American Chemical Society 127(20):7328-7329.

Zhou, Fei, et al.

2008 Quantitative Analysis of Dipole and Quadrupole Excitation in the Surface Plasmon Resonance of Metal Nanoparticles. The Journal of Physical Chemistry C 112(51):20233-20240.

Zhou, H. S., et al.

1994 Controlled synthesis and quantum-size effect in gold-coated nanoparticles. Physical Review B 50(Copyright (C) 2009 The American Physical Society):12052.

Zhu, Heng, et al.

2008 Assembly of Dithiocarbamate-Anchored Monolayers on Gold Surfaces in Aqueous Solutions. Langmuir 24(16):8660-8666.

Zijlstra, P., and M. Orrit

2011 Single metal nanoparticles: optical detection, spectroscopy and applications. Reports on Progress in Physics 74(10):106401.

Zweifel, Daniel A., and Alexander Wei

2005 Sulfide-Arrested Growth of Gold Nanorods. Chemistry of Materials 17(16):4256-4261.